

Christian-Albrechts-Universität zu Kiel
Institut für Experimentelle und Angewandte Physik

DISSERTATION
ZUR ERLANGUNG DES AKADEMISCHEN GRADES
DOCTOR RERUM NATURALIUM
DER MATHEMATISCH-NATURWISSENSCHAFTLICHEN FAKULTÄT
DER CHRISTIAN-ALBRECHTS-UNIVERSITÄT ZU KIEL

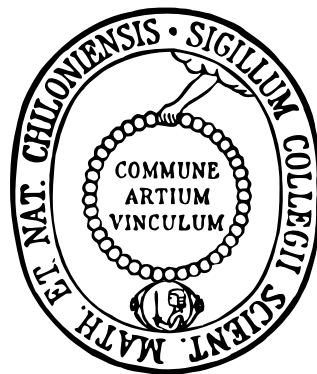
SCANNING TUNNELING SPECTROSCOPY
OF
PB THIN FILMS

VORGELEGT VON
MICHAEL BECKER

GEBOREN AM 30.10.1975

AUS KIEL

KIEL, OKTOBER 2010



This work was typeset in L^AT_EX.

Referent: Prof. Dr. Richard Berndt

Korreferent/in: Prof. Dr. Michael Bauer

Tag der mündlichen Prüfung: 13. Dezember 2010

Zum Druck genehmigt: Kiel, 13. Dezember 2010

gez. Dekan Prof. Dr. Lutz Kipp

For my beloved parents.

Abstract

The present thesis deals with the electronic structure, work function and single-atom contact conductance of Pb thin films, investigated with a low-temperature scanning tunneling microscope.

The electronic structure of Pb(111) thin films on Ag(111) surfaces is investigated using scanning tunneling spectroscopy (STS). Quantum size effects, in particular, quantum well states (QWSs), play a crucial role in the electronic and physical properties of these films [1, 2]. Quantitative analysis of the spectra yields the QWS energies as a function of film thickness, the Pb bulk-band dispersion in Γ -L direction, scattering phase shifts at the Pb/Ag interface and vacuum barrier as well as the lifetime broadening at $\bar{\Gamma}$.

The work function ϕ is an important property of surfaces, which influences catalytic reactivity and charge injection at interfaces. It controls the availability of charge carriers in front of a surface. Modifying ϕ has been achieved by deposition of metals and molecules [3, 4]. For investigating ϕ at the atomic scale, scanning tunneling microscopy (STM) has become a widely used technique. STM measures an apparent barrier height ϕ_a [5], which is commonly related to the sample work function ϕ_s by [6]: $\phi_a = (\phi_s + \phi_t - |eV|)/2$, with ϕ_t the work function of the tunneling tip, V the applied tunneling bias voltage, and $-e$ the electron charge. Hence, the effect of the finite voltage in STM on ϕ_a is assumed to be linear and the comparison of ϕ_a measured at different surface sites is assumed to yield quantitative information about work function differences. Here, the dependence of ϕ_a on the Pb film thickness and applied bias voltage V is investigated. ϕ_a is found to vary significantly with V . This bias dependence leads to drastic changes and even inversion of contrast in spatial maps of ϕ_a , which are related to the QWSs in the Pb films. It is shown how accurate quantitative information about work function differences can be obtained and how these differences depend on the QWSs in the Pb thin films.

The electron transport properties and mechanical characteristics of atom-sized metallic contacts are of fundamental interest in view of future nanoscale device technologies. Proximity probes like STM, metal break junctions, and related techniques, together with computational methods for simulating tip-sample interactions, have made it possible to address this question [7]. While the importance of atomic structure and bonding for transport through single-atom junctions has repeatedly been emphasized, investigations of the influence of subsurface bonding properties have been rare [8, 9]. Here, the contact formation of a STM tip approaching Pb(111) thin films supported on Ag(111) substrates is investigated. Contacts on monolayer films are found to differ from contacts made on thicker Pb films. This behavior is explained in terms of different vertical bonding-strengths due to a charge-transfer induced surface dipole. Furthermore, the single-atom contact conductance on Pb(111) films beyond the first monolayer is determined.

It is shown that analyses based on hitherto widely used conventional conductance histograms [10] may overestimate the single-atom contact conductance by as much as 20%.

Zusammenfassung

Die vorliegende Dissertation befasst sich mit der elektronischen Struktur, der Austrittsarbeit und der Einatomkontaktleitfähigkeit dünner Pb Filme, welche mit einem Tieftemperatur-Rastertunnelmikroskop untersucht wurden.

Die elektronische Struktur von dünnen Pb(111) Filmen auf Ag(111) Oberflächen ist mittels Rastertunnelspektroskopie (RTS) untersucht worden. Quanteneffekte, insbesondere Quantentrogzustände (QTZ), haben einen entscheidenden Einfluss auf die elektronischen und physikalischen Eigenschaften von diesen Filmen [1, 2]. Die quantitative Analyse der Spektren ergibt die Quantentrogzustandsenergien in Abhängigkeit der Filmdicke, die Dispersion der Pb Volumenzustände in Γ -L Richtung, die Streuphasen am Pb/Ag Übergang und der Vakuumbarriere als auch die Lebensdauer verbreiterung der QTZ am $\bar{\Gamma}$ -Punkt.

Die Austrittsarbeit ϕ ist eine wichtige Kenngröße von Oberflächen, welche Einfluss auf das katalytische Reaktionsvermögen und den Ladungsübergang an Grenzflächen hat. Sie beeinflusst maßgeblich die Verfügbarkeit von Ladungsträgern dicht vor der Oberfläche. Eine Veränderung von ϕ kann durch das Aufbringen von Metallen und Molekülen erreicht werden [3, 4]. Für das Vermessen von ϕ auf atomarer Skala ist mittlerweile die Rastertunnelmikroskopie (RTM) eine weit verbreitete Technik. RTM misst eine scheinbare Barrierenhöhe ϕ_a [5], welche weithin zur Austrittsarbeit der Probe ϕ_s wie folgt in Beziehung gesetzt wird [6]: $\phi_a = (\phi_s + \phi_t - |eV|)/2$, wobei ϕ_t die Austrittsarbeit der Tunnelspitze, V die angelegte Tunnelspannung, und e die Elementarladung darstellt. Folglich wird der Einfluss der Tunnelspannung in der RTM auf ϕ_a als linear angenommen. Weiterhin wird angenommen das ϕ_a Messungen, welche auf unterschiedlichen Oberflächenbereichen vorgenommen wurden, quantitative Aussagen über Austrittsunterschiede zulassen. Die Abhängigkeit von ϕ_a von der Pb Filmdicke und der angelegten Tunnelspannung V soll hier untersucht werden. Es wird gezeigt, das ϕ_a als Funktion von V in signifikanter Weise nicht-linear variiert. Diese Spannungsabhängigkeit führt zu drastischen Veränderungen bis hin zu Kontrastinversionen von räumlichen Karten der scheinbaren Barrierenhöhe ϕ_a , welche mit den QTZn in den Pb Filmen in Verbindung stehen. Es wird gezeigt, wie eine korrekte quantitative Bestimmung der Austrittsunterschiede vorgenommen werden kann und wie diese Differenzen von den QTZn in den dünnen Pb Filmen abhängen.

Die Transporteigenschaften von Elektronen und die mechanischen Charakteristiken von atomaren metallischen Kontakten sind hinsichtlich zukünftiger nanoskaliger Bauteiltechnologien von fundamentalem Interesse. Näherungs sonden wie die RTM, mechanisch-kontrollierte metallische Bruchkontakte und artverwandte Techniken, zusammen mit computergestützten Methoden zur Simulation von Spitze-Probe Wechselwirkungen haben es ermöglicht, sich dieser Fragestellung anzunehmen [7]. Während der Einfluss der atomaren Struktur und der

Bindungseigenschaften auf den Elektronentransport durch Einatomkontakte wiederholt betont wurde, gibt es bis dato wenige Untersuchungen über den Einfluss der Bindungscharakteristiken dicht unterhalb der Oberfläche der Kontaktstelle [8, 9]. In dieser Arbeit wird die Kontaktbildung zwischen einer RTM Spitze und den auf Ag(111) aufgetragenen Pb(111) Filmen untersucht. Kontakte auf Pb Monolagen (ML) unterscheiden sich von Kontakten auf dickeren Pb Filmen. Dieses Verhalten lässt sich mittels der Unterschiede in den vertikalen Bindungskräften verstehen, welche auf ladungstransferinduzierte Oberflächendipole beruhen. Des Weiteren wird die Einatomkontaktleitfähigkeit auf den dickeren Pb(111) Filmen ($ML > 1$) bestimmt. Es wird gezeigt, dass Untersuchungen, welche auf den bisher weitestgehend genutzten konventionellen Leitfähigkeitshistogrammen [10] basieren, die Einatomkontaktleitfähigkeit zu 20% überschätzen können.

Contents

| | | |
|-----|--|----|
| 1 | Introduction | 1 |
| 2 | Scanning Tunneling Microscopy | 5 |
| 2.1 | Experimental Setup | 5 |
| 2.2 | Working Principle | 8 |
| 2.3 | Operating Modes | 12 |
| 3 | Growth and Morphology of Pb/Ag(111) | 15 |
| 3.1 | Sub-Monolayer Regime | 16 |
| 3.2 | The Wetting Layer | 20 |
| 3.3 | Pb Islands | 23 |
| 4 | Electronic Structure of Pb/Ag(111) | 27 |
| 4.1 | Phase Accumulation Model | 28 |
| 4.2 | Quantum Well State Energies | 31 |
| 4.3 | Band Structure and Scattering Phase Shifts | 33 |
| 4.4 | Linewidths and Lifetime Broadening | 35 |
| 4.5 | Summary | 40 |
| 5 | Apparent Barrier Height on Noble Metal Surfaces | 41 |
| 5.1 | Introduction | 41 |
| 5.2 | Experiment | 43 |
| 5.3 | Modeling | 43 |
| 5.4 | Results and Discussion | 45 |
| 5.5 | Conclusion | 51 |
| 5.6 | Annex: Influence of the Geometric Asymmetry of the Junction . . | 52 |
| 6 | Contrast Inversion of the Apparent Barrier Height of Pb Thin Films | 55 |
| 6.1 | Introduction | 55 |
| 6.2 | Experiment | 56 |
| 6.3 | Modeling | 57 |
| 6.4 | Results and Discussion | 57 |

| | | |
|-------|---|-----|
| 6.5 | Conclusion | 62 |
| 7 | Conductance of Atom-Sized Pb Contacts | 63 |
| 7.1 | Introduction | 63 |
| 7.2 | Experiment | 65 |
| 7.3 | Results and Discussion | 65 |
| 7.3.1 | Thickness Dependence of Pb Contacts | 67 |
| 7.3.2 | Imaging at Contact | 69 |
| 7.3.3 | Analysis of Pb Conductance Histograms | 71 |
| 7.3.4 | Role of the Tip | 74 |
| 7.4 | Conclusion | 75 |
| | Summary | 77 |
| A | Pb/Ag(111) Quantum Well State Energies | 79 |
| B | Scanning Tunneling Microscopy on High-Temperature Superconductors | 83 |
| B.1 | Introduction | 83 |
| B.2 | Experiment | 85 |
| B.3 | Results and Discussion | 86 |
| B.3.1 | Spectroscopy at Low Tunneling Resistances | 88 |
| B.3.2 | Temperature Resolved Measurements | 91 |
| B.4 | Summary | 92 |
| | Bibliography | 93 |
| | List of the Author's Publications | 103 |
| | Wissenschaftlicher Lebenslauf | 107 |
| | Danksagung | 109 |

CHAPTER 1

Introduction

As anyone who has suffered from a rusting car knows, surface processes play a significant part in our lives: corrosion on the car body, friction in the wear and tear on the engine, catalysis in the petrol refining, all occur at surfaces [11].

Control of such processes by tailoring functionalized surfaces at the nanometer scale is one of the goals of the so-called nanotechnology. In particular, control of the charge density on a metal surface makes it possible to tune its catalytic reactivity [12] and research in this field may lead to improvements of the effectivity of, e.g., anti-corrosive protections, and of the production of industrially important chemicals. However, before elaborate surface morphologies with the desired functionalities can be tailored, a thorough understanding of the functionalities of clean, perfect surfaces must be accomplished.

Among all the metal species, ultra-thin Pb(111) films have attracted vast attentions. Prominently, it has been found that the electron Fermi wavelength λ_F of Pb is nearly four times the lattice spacing along the [111] direction, hence most physical properties of Pb(111) films such as, e.g., the electrical resistivity, superconducting transition temperature, Hall coefficient, surface energy, work function, electron-phonon coupling, and chemical reactivity, all oscillate with the thickness in a quasi bilayer period [1, 13–19]. The thickness selectivity of chemical surface processes on the Pb(111) films has been evidenced by adsorption experiments of O₂ and cobalt-phthalocyanine (CoPc) molecules as probes of the chemical reactivity [19, 20]. However, it is desirable to gain information on the chemical reactivity of a certain surface morphology without the need of adsorption experiments. The work function ϕ of a metal surface, which controls the

availability of charge carriers in front of a surface, contains the necessary information to improve our understanding of such chemical surface processes. Scanning tunneling microscopy (STM) measures an apparent barrier height ϕ_a [5], which is commonly related to the sample work function ϕ_s by [6]: $\phi_a = (\phi_s + \phi_t - |eV|)/2$, with ϕ_t the work function of the tunneling tip, V the applied tunneling bias voltage, and $-e$ the electron charge. Hence, the effect of the finite voltage in STM on ϕ_a is assumed to be linear and the comparison of ϕ_a measured at different surface sites is assumed to yield quantitative information about work function differences. However, while the scanning tunneling microscope has become a widely used tool for the investigation of ϕ_s at the nanoscale, controversial experimental results concerning the voltage dependence of STM derived work functions have been reported [21, 22] and the reliability and limitations of the STM derived ϕ_s still remain unclear.

Another important aspect of nanotechnology is the development of future nanoscale electronic devices. For example, in 2010 the 32-nm-process has been employed by several semiconductor companies. Meaning that the typical half-distance between identical features in an array of a memory cell is around 32 nm. According to the international technology roadmap for semiconductors (ITRS) it is expected that the 32-nm-process will be followed by the 22-nm-process in 2011/2012, and the 16-nm-process is expected to be reached in 2013/14. Hence, the fast approach of technological devices to sizes comparable with their atomic constituents makes a fundamental understanding of how such nanoscale structures behave in this realm of utmost importance. Therefore it is highly interesting to investigate the electron transport through single atoms, as they represent the smallest possible building blocks of such nanoscale circuitry. At the atomic scale all common macroscopic knowledge about a materials properties becomes invalid. The familiar Ohm's law, from which we learn that the resistance of a conductor scales proportional to its length, breaks down [7]. The reason is that the distance an electron travels between two scattering events is typically much larger than the atomic size. The electrons traverse an atom-sized conductor ballistically, and the resistance becomes independent of its length. In fact, the character of the resistance changes conceptually and it is necessary to invoke the wave nature of the electrons in the conductor for a proper description. The chemical nature of the metallic element starts to play an essential role. As a

consequence, while in the macroscopic world Au is a better conductor than Pb by an order of magnitude, for conduction through a single atom, Pb beats Au by a factor of ≈ 1.5 [7]. In addition to the chemical nature, the dependence of the electron transport properties of such atom-sized conductors on the detailed geometric structure and bonding properties of the constituent atoms has been emphasized [7]. However, investigations of the influence of bonding on the electron transport for well characterized conductor geometries have been rare [8, 9] and more work appears to be required for a thorough understanding of electron transport at the single-atom scale.

This thesis is organized as follows. Chapter 2 gives an introduction to the basic principles of STM and the experimental setup. In Chapter 3 an overview of the growth and surface morphology of Pb thin films on Ag(111) is given. An investigation into the electronic structure of the Pb thin films is presented in Chapter 4. Quantum size effects, in particular, quantum well states (QWSs), play a crucial role for the electronic properties of these films [1, 2]. A quantitative analysis of scanning tunneling spectroscopy (STS) measurements yields the QWS energies as a function of film thickness, the Pb bulk-band dispersion in Γ -L direction, scattering phase shifts at the Pb/Ag interface and vacuum barrier as well as the lifetime broadening at $\bar{\Gamma}$.

In Chapters 5 and 6 the voltage dependence of the relation between the apparent barrier height ϕ_a and the work function of the sample ϕ_s is investigated. The influence of the band structure of the sample, as well as the geometry of the tip-sample junction are investigated in Chapter 5 using the noble metal (111) surfaces as a reference system. Results for Pb/Ag(111) are presented in Chapter 6. The dependence of ϕ_a on the Pb film thickness and applied bias voltage V is investigated. ϕ_a is found to vary significantly with V . This bias dependence leads to drastic changes and even inversion of contrast in spatial maps of ϕ_a , which are related to the QWSs in the Pb films. It is shown how accurate quantitative information about work function differences can be obtained and how these differences depend on the QWSs in the Pb thin films.

A detailed investigation of the impact of bonding on conductance measurements of single-atom Pb contacts are presented in Chapter 7. The contact formation of a STM tip approaching Pb(111) thin films supported on Ag(111)

substrates is analyzed. Contacts on monolayer films are found to differ from contacts made on thicker Pb films. This behavior is explained in terms of different vertical bonding-strengths due to a charge-transfer induced surface dipole. Furthermore, the single-atom contact conductance on Pb(111) films beyond the first monolayer is determined. It is shown that analyses based on hitherto widely used conventional conductance histograms [10] may overestimate the single-atom contact conductance by as much as 20%.

Parts of this thesis have been published or are accepted for publication in peer reviewed journals as indicated below:

- Chapter 4 has been published in large part as *Scattering and lifetime broadening of quantum well states in Pb films on Ag(111)*, M. Becker, R. Berndt, Phys. Rev. B **81**, 205438 (2010).
- Chapter 5 has been published as *Influence of band structure on the apparent barrier height in scanning tunneling microscopy*, M. Becker, R. Berndt, Phys. Rev. B **81**, 035426 (2010).
- Chapter 6 has been published as *Contrast inversion of the apparent barrier height of Pb thin films in scanning tunneling microscopy*, M. Becker, R. Berndt, Appl. Phys. Lett. **96**, 033112 (2010).
- Chapter 7 has been published as *Conductance of atom-sized Pb contacts*, M. Becker, R. Berndt, New J. Phys. **12**, 113010 (2010).

CHAPTER 2

Scanning Tunneling Microscopy

The experiments described in this thesis were all conducted under ultra-high vacuum (UHV) conditions which is necessary to obtain well characterized surfaces. Additionally, to improve the spectroscopic resolution and for a reduction of drift, measurements were performed at cryogenic temperatures. In this chapter, a brief introduction to the experimental setup of the UHV system and the scanning tunneling microscope is given.¹ Furthermore, the basic experimental principle of scanning tunneling microscopy (STM) and scanning tunneling spectroscopy (STS) and the various operational modes of the instrument and acquisition methods used during this thesis are introduced. For a more detailed description of STM and other scanning probe techniques, the interested reader is referred to one of the many textbooks on this topic [24–29].

2.1 Experimental Setup

UHV System: Figure 2.1 shows a schematic drawing of the UHV system. The STM chamber (green) on the left contains the cryostats and the scanning tunneling microscope, the chamber on the right (red) is the preparation chamber (PREP chamber) which contains the usual vacuum science instruments for sample characterization and preparation. Additionally there is a loadlock (not visible in Fig. 2.1) connected to the PREP chamber, such that tips, samples and evap-

¹ A thorough specification can be found in the PhD thesis by J.U. Kliewer [23].

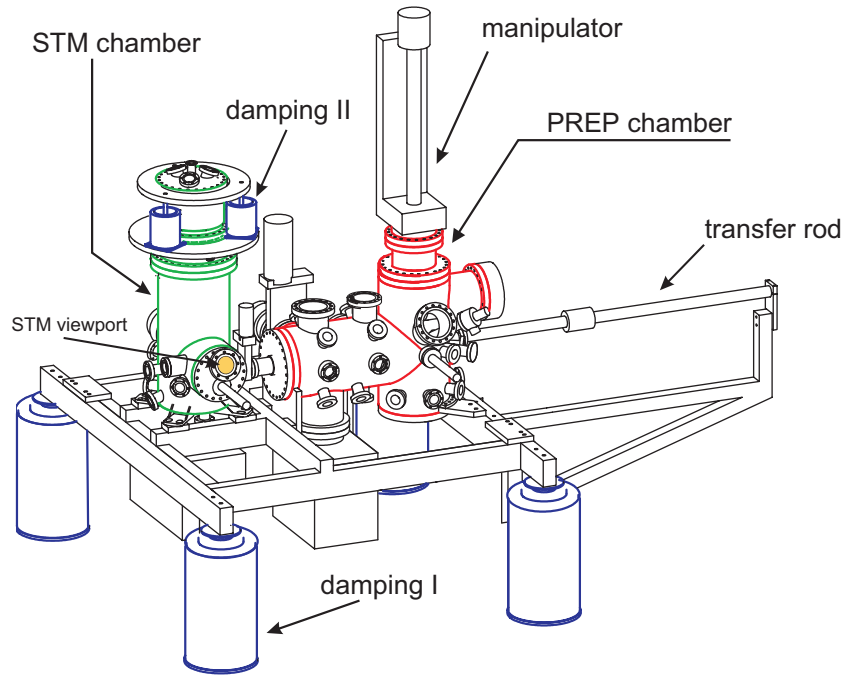


Figure 2.1: Schematic overview of the UHV system (adopted from Ref. [23]).

orators can be introduced into the UHV system without breaking the vacuum. Samples, tips and evaporators can be transferred between the STM and PREP chambers by a magnetically driven linear translator (transfer rod). The entire system is mounted on an aluminum frame which is placed onto pendulum air dampers (Fig. 2.1, damping I).

The STM chamber is equipped with two cryostats, an inner 6 liter liquid Helium cryostat and a 5 liter liquid Nitrogen cryostat surrounding the Helium cryostat, thereby reducing thermal radiation. The STM is placed in a copper stage which itself is tightly screwed to the bottom of the Helium dewar, thereby providing a good thermal contact. This way a measurement temperature of 5 K for a period of ≈ 20 hours can be maintained. The top flange, which is connected to the inner Helium cryostat, is vibrationally isolated from the rest of the vacuum system through a membrane bellow which itself is kept from collapsing by a second vibration isolation stage made of air dampers (Fig. 2.1, damping II).

The PREP chamber is equipped with the following vacuum science instru-

ments: a quadrupole mass spectrometer for residual gas analysis, a quartz micro balance for evaporation monitoring and calibration, a LEED/Auger combination for sample characterization and analysis, a 4 axes manipulator for sample heating and cooling and precise positioning, a sputter gun for sample and tip cleaning.

All three chambers are evacuated with turbo molecular drag pumps which are backed by rotary vane pumps and are equipped with cold cathode gauges for measuring the pressure down to $2 \cdot 10^{-11}$ mbar. The PREP chamber has an additional titanium sublimation pump. During STM measurements all mechanical pumps are shut down and separated from the PREP and STM chambers with gate valves, and the vacuum is maintained by two ion getter pumps. With this system, a base pressure below $5 \cdot 10^{-10}$ mbar is reached in the PREP chamber when pumped by ion getter pump, turbo molecular drag pump and Titanium sublimation pump. A base pressure below ($5 \cdot 10^{-11}$ mbar) is reached in the STM chamber when both dewars are filled with liquid Helium and liquid Nitrogen, respectively, and the chamber is pumped by the ion getter pump.

Scanning Tunneling Microscope: Figure 2.2 shows a photograph of the scanning tunneling microscope as it can be seen through the STM viewport (see Figure 2.1; highlighted in yellow). In this setup, the movement of the scanning probe is carried out by a horizontally mounted piezoelectric tube scanner (a) [23, 30, 31]. Ideally, the tip (b) is mounted, such that the tip-apex is close to the centerline of the tube scanner, resulting in almost isotropic lateral (x,y) deflection constants. At 5 K, the deflection constants are ≈ 30 Å/V in lateral direction and ≈ 5 Å/V in vertical (z) direction. The precise deflection constants depend on the tip geometry and the deflection of the tube scanner.

The sample (c) is mounted on the slider (d), which is used for the coarse positioning of the sample in front of the tip. This coarse positioning is done by a slip-stick drive, which consists of 3 piezoelectric tube drives (one of which is shown in Fig. 2.2, (e)) situated below the slider, and which also enables the adjustment of the scanning angle between tip centerline and sample surface plane.

Electronics: The STM is controlled by commercial *ECS* digital electronics and software. The current I between tip and sample is amplified and converted to a voltage V_I by a transimpedance amplifier (*Femto DLPCA-200*) with a variable

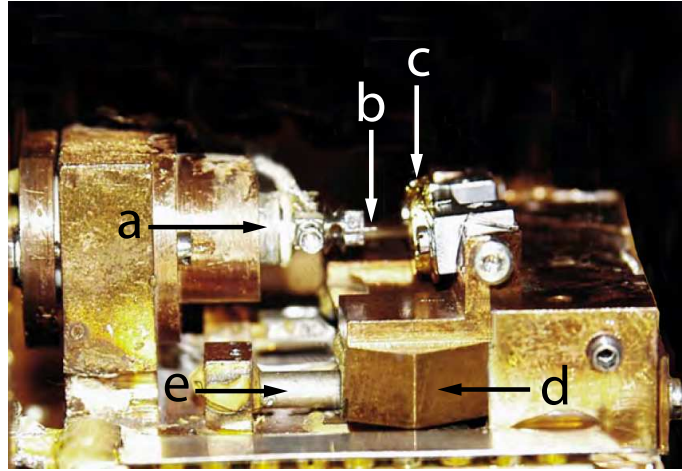


Figure 2.2: Photograph of the scanning tunneling microscope: (a) horizontally mounted piezoelectric tube scanner, (b) tip, (c) sample, (d) slider for the slip-stick coarse approach, (e) coarse approach piezoelectric tube drive.

gain of $10^3 - 10^{11}$ V/A. The commercial equipment is supplemented by homebuilt analog electronics (made by Laurent Libiouille) which are used for the attenuation and offset calibration of the x, y, z -deflection voltages, sample voltage V , and the converted tunneling-current voltage V_I . Using the *ECS* high-voltage amplifier, voltages in the range of ± 150 V can be applied to the piezoelectric tube scanner, which yields a maximum lateral scan range of $\approx 900 \times 900$ nm².

As part of this thesis, complementary analog electronic components were built and added to the electronic setup. The modifications were intended to improve the signal-to-noise ratio of the output sample voltage V . For the noise component δV of the sample voltage V a reduction of δV from ≈ 700 $\mu\text{V}_{\text{peak-peak}}$ to 100 $\mu\text{V}_{\text{peak-peak}}$ has been achieved. Similar electronics have been employed to improve the signal-to-noise ratio of the tunneling-current voltage V_I .

2.2 Working Principle

In order to define the necessary variables for the discussion of the STM measurements presented in this thesis a short introduction on the working principle of STM along with the basic formulas describing the tunneling current is given here. Figure 2.3(a) shows a schematic diagram of the STM tunneling junction.

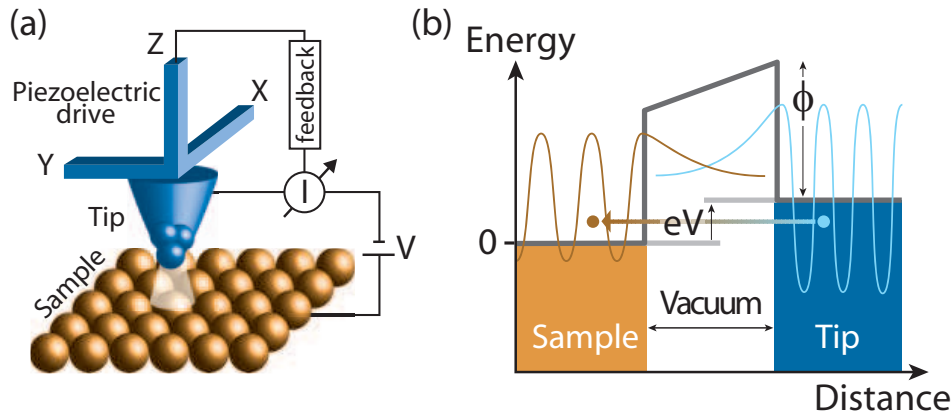


Figure 2.3: (a) Schematic diagram of the STM tunneling junction. Using the piezoelectric drive the tip sample separation is regulated (feedback) in order to keep the current I constant. (b) One-dimensional energy diagram of the tunneling process. The electron wave functions decay exponentially into the vacuum, having a small overlap, thus allowing electrons to tunnel from one electrode to the other. With a positive V applied to the sample the electrons tunnel preferentially from the tip into unoccupied sample states. Figure adopted from Ref. [32].

An atomically sharp tip is brought in close proximity to a sample surface. If a voltage V is applied between tip and sample, a net tunneling current I can be detected. Using the piezoelectric transducers the tip sample separation is regulated (feedback-loop) in order to maintain a constant current I . By scanning the tip across the surface, it is possible to generate a three-dimensional real-space image of the surface. For low voltages these images can be interpreted in terms of contour maps of constant local density of states (LDOS). Throughout this thesis, the voltage V is applied to the sample. Figure 2.3(b) shows an energy diagram illustrating the tunneling process. The tip on the right side is biased by eV . The vacuum potential barrier, which depends on the work function of tip and sample, respectively, and the applied bias V , exhibits a roughly trapezoidal shape. The electron wave functions (while periodic in the bulk) decay exponentially into the vacuum, having a small overlap, thus allowing the electrons to tunnel from one electrode to the other. Hence, the magnitude of the current depends exponen-

tially on the tip-sample separation \tilde{z} .¹ With a positive V applied to the sample, as in Fig. 2.3(b), the electrons tunnel preferentially from the tip into unoccupied sample states. Thus leading to a net current flow from the tip to the sample. At $T = 0$ K, all electronic states below the corresponding Fermi levels E_F of tip and sample, respectively, are occupied. Throughout this thesis E_F of the sample has been used as the reference level and is set to 0 eV. Within the one-dimensional Wentzel-Kramer-Brillouin (WKB) approximation in the limit $T = 0$ K, the current flowing between tip and sample is proportional to the sum of the tunneling electrons in the energy range between 0 and eV [33]:

$$I \propto \int_0^{eV} \rho_s(E) \rho_t(E - eV) T(E, V, \tilde{z}) dE, \quad (2.1)$$

where ρ_s and ρ_t denote the local density of states (LDOS) of the sample and the tip, respectively, at the corresponding surface. The transmission probability $T(E, V, \tilde{z})$ for an electron impinging on the tunneling barrier with energy E is given by [6, 34]

$$T(E, V, \tilde{z}) = \exp \left[-\frac{2}{\hbar} \int_0^{\tilde{z}} \sqrt{2m(U(s) - E)} ds \right], \quad (2.2)$$

where $U(s)$ is the barrier potential felt by the tunneling electron. The sample and tip surfaces are located at $s = 0$ and $s = \tilde{z}$ respectively. The barrier potential is widely approximated by the electrostatic potential of an infinitely blunt tip, i.e. a tip with radius $R \rightarrow \infty$, such that:

$$U(s) = U_\infty(s) = \phi_s + \frac{s}{\tilde{z}} (eV + (\phi_t - \phi_s)). \quad (2.3)$$

Here, ϕ_s is the sample work function and ϕ_t the local work function of the tip apex. Using U_∞ , the expression for the transmission probability Eq. 2.2 can be

¹ It is important to note, that STM measures only relative tip displacements, \tilde{z} differs from the measured tip excursion z by an offset z_i .

further simplified as [6]

$$T(E, V, \tilde{z}) = \exp \left[-\frac{2\tilde{z}}{\hbar} \sqrt{m(\phi_s + \phi_t + eV - 2E)} \right]. \quad (2.4)$$

Supported by the experimental findings, it is common practice to assume, that the LDOS of the tip ρ_t is a slowly varying function of E and that the transmission probability $T(E, V, \tilde{z})$ is smooth in the range of the applied voltages with a maximum at $E = eV$. Under these assumptions, differentiating Equation 2.1 with respect to V yields a differential conductance which can be approximated as

$$\frac{dI}{dV} \propto \rho_s(E) T(eV, V, \tilde{z}). \quad (2.5)$$

Hence, by measuring $I - V$ characteristics with the STM it is possible to probe the local density of states of the surface with atomic scale resolution. More detailed discussions on the approximations used here are given in Refs. [35–38].

Furthermore, the STM offers the possibility to study the current as a function of tip-excursion z . Starting from Eqs. 2.1 and 2.4 it can be shown that for voltages close to $V = 0$ V, the tunneling current can be approximated as

$$I \propto V \rho_s(E_F) \rho_t(E_F) \exp \left[-\frac{2\tilde{z}}{\hbar} \sqrt{2m\phi_a} \right] \quad (2.6)$$

where $\phi_a = (\phi_s + \phi_t)/2$ is an apparent barrier height (ABH)¹ of the vacuum potential. Hence, by measuring the exponential variation of the tunneling current with z , the ABH can be calculated from the slope of $\ln(I(z))$ as [6, 39]

$$\phi_a = \frac{\hbar^2}{8m} \left(\frac{d \ln(I)}{dz} \right)^2, \quad (2.7)$$

giving access to the mean value of the work functions of tip and sample.

¹ Note, that the relation between ϕ_a and ϕ_s is only valid for *small* voltages. The meaning of *small* in this context is investigated in Chapters 5 and 6.

2.3 Operating Modes

Topographic imaging

During this thesis all topographic images were acquired in the constant-current mode. In this standard mode, the tunneling current I is kept constant by continuously feedback-adjusting the tip vertical position during the scan. Since the tunneling current integrates over all states in the energy range from 0 eV to eV , the constant-current mapping corresponds to a profile of constant integrated electron density of states. When the LDOS is homogeneous over the mapped area, this profile corresponds to constant tip-sample separation.

dI/dV spectroscopy

dI/dV spectra can either be obtained by numerical differentiation of $I(V)$ curves or by a lock-in amplifier technique. In the latter case, a small sinusoidal modulation $V_m \sin(\omega t)$ is superimposed to the sample voltage V , and the corresponding modulation of the tunneling current is measured [23, 40, 41]. The amplitude of the current modulation is proportional to dI/dV , given that $V_m \ll V$ and that $I(V)$ is sufficiently smooth. The additional broadening induced by the lock-in technique is on the order of $1.73V_m$ [42]. Hence, when analyzing the width Δ of spectroscopic features in the dI/dV signal (see e.g. Section 4.4), the amplitude of the modulation voltage has to be such that $V_m \ll \Delta$. The advantage offered by the lock-in technique is that the sampling frequency ω can be selected outside the typical frequency domains of mechanical vibrations or electronic noise, thereby enhancing the measurement sensitivity. Amplitudes of V_m between $500 \mu\text{V}$ and 10 mV were used in the present study. The frequency was usually set in the range of $10 - 11 \text{ kHz}$. In general, the frequency should be chosen such that the steptime of the bias sweep is large compared to the cycle duration of the modulation voltage.¹

Two kinds of dI/dV spectroscopy using the lock-in technique have been used

¹ In addition to the instrumental broadening due to the lock-in technique, one has to bear in mind the thermal broadening, which is on the order of $3.5 k_B T$ or $\approx 1.5 \text{ meV}$ at $T = 5 \text{ K}$ as in the present study.

during the present thesis and are outlined below:

Constant-height dI/dV spectroscopy: In this spectroscopy mode, the feedback loop is switched off and the vertical and lateral position of the tip is kept constant. Then a voltage sweep is applied to the junction and the tunneling current $I = I(V)$ and dI/dV are recorded.

Constant-current $z(V)$ & dI/dV spectroscopy: In this mode, the bias voltage is swept while the feedback loop remains active. The lateral position of the tip is kept constant. The vertical tip displacement $z = z(V)$ is recorded concomitantly. Additionally, dI/dV can be measured by means of the lock-in technique. The dI/dV signal measured this way resembles dz/dV . Note, that the modulation frequency ω has to be set higher than the cut-off frequency of the feedback loop. Otherwise the feedback loop compensates the bias modulation by continuously adjusting the tip-sample separation. In addition the velocity of the bias sweep dV/dt has to be low enough, such that the feedback loop can completely adjust the tip height in order to maintain the steady state current constant.

$I(z)$ measurements

Two different kinds of $I(z)$ measurements have been employed. While both methods can be used to determine the ABH, so-called conventional $I(z)$ measurements, as described below, are also suited to perform conductance measurements in the contact regime (see Chapter 7). The constant-current dI/dz method (see below) is well suited to perform voltage-resolved ABH measurements in a fast and convenient way.

Conventional $I(z)$ measurements: The tunneling current $I(z)$ is recorded while the feedback loop is switched off and the tip is approached to (or retracted from) the sample with constant bias voltage. Here, the velocity of the tip motion (dz/dt) has to be set such that the measured current variation dI/dz is not affected by the cut-off frequencies of the STM-electronics nor the transimpedance amplifier.

Constant-current dI/dz measurements: For this spectroscopy mode the feedback loop is kept active and a small sinusoidal voltage $V_m \sin(\omega t)$ is applied to the Z-segment of the piezoelectric tube scanner. The response on the current signal is measured via the lock-in technique. The bias voltage is ramped over the voltage range of interest. The recorded signals are $dI/dz(V)$ and $z(V)$. The velocity of the bias sweep dV/dt has to be low enough such that during each bias step the z -motion can complete several oscillation cycles. The frequency of the modulation voltage has to be set above the cut-off frequency of the feedback loop. Otherwise the feedback loop compensates the oscillating motion by adjusting the tip-sample separation. Additionally, the frequency has to be set well below the resonant frequency of the z -motion of the piezoelectric tube scanner. In the present thesis, the frequency of the modulation voltage was chosen between 300 and 1000 Hz, and the feedback-loop was set such, that doubling the modulation frequency ω did not affect the experimental result. The root-mean-square amplitude of the modulation was usually set to 0.15 Å.

CHAPTER 3

Growth and Morphology of Pb/Ag(111)

In this chapter the different surface structures found during the growth of Pb on Ag(111) are presented. The growth of Pb on noble metal substrates has been investigated in several research reports [43–61]. In particular, growth of Pb/Ag(111) in the sub-monolayer and monolayer regime has been investigated by means of different surface-sensitive techniques such as low-energy electron diffraction (LEED) [43–45], Auger electron spectroscopy (AES) [44, 45], photoelectron spectroscopy (PES) [56, 60, 61], surface X-ray diffraction (SXRD) [57], and STM [48, 49, 56–59]. It is found that the Pb/Ag(111) surface morphology strongly depends on the amount of deposited Pb as well as on the substrate temperature during deposition and post-annealing procedures. Given the preparation procedure as presented below the stages of Pb growth on Ag(111) are as follows. For coverages well below 1/3 monolayer (ML), the Pb atoms appear randomly distributed within the first Ag layer. Even though Pb and Ag are immiscible in the bulk, they alloy in the sub-monolayer regime. For coverages of 1/3 ML the Pb/Ag surface alloy arranges in a long-range ordered ($\sqrt{3} \times \sqrt{3}$) R30° superstructure as evidenced by LEED, SXRD, and STM [43, 58]. Increasing the coverage from 1/3 ML to 1 ML Pb, the Pb atoms segregate from the substrate. This segregation can be seen as the consequence of the immiscibility of Pb/Ag in the bulk and is also called de-alloying [62, 63]. For coverages of 1 ML the de-alloying process results in an overlayer with an average in-plane lattice constant of a free-standing Pb monolayer (3.5 Å) [43–45, 49, 56]. Additionally, a hexagonal moiré-type modulation of this so-called wetting layer (WL) with a ($\sqrt{19} \times \sqrt{19}$) R23.4° supercell is observed. Further deposition of Pb results in

three-dimensional island growth on top of the WL, also referred to as Stranski-Krastanov growth [44, 45]. Film thicknesses are numbered in ML including the WL. The sub-monolayer regime, the wetting layer, and the three-dimensional island growth are discussed in sections 3.1, 3.2, and 3.3, respectively.

Sample preparation: The Ag(111) single crystal surfaces were prepared by repeated Ar⁺ sputter and anneal cycles. Pb has been evaporated from a resistively heated tungsten crucible at deposition rates of ≈ 1 ML/min. The Ag(111) sample was held at room temperature during deposition, and the pressure in the preparation vacuum chamber did not exceed 2×10^{-9} mbar. The samples were annealed at 450 ± 50 K for 2 min subsequent to the deposition (Subsequently it was found that for coverages in excess of 1 ML, the post-annealed surfaces exhibit the same surface morphology and electronic properties as non-post-annealed surfaces. Therefore, the post-annealing has been omitted in the bulk of the studies on Pb islands beyond the WL.).

3.1 Sub-Monolayer Regime

While most STM studies in the sub-monolayer regime are concerned with the $(\sqrt{3} \times \sqrt{3}) R30^\circ$ alloy structure no detailed analysis of the equilibrium Pb distribution at coverages below 1/3 ML as presented here has been reported. Figure 3.1 shows an STM topograph of the so-called disordered surface alloy of Pb on Ag(111). 0.1 ML Pb have been deposited on the Ag substrate. The Pb atoms (red/yellow spots) appear as protrusions with an apparent height between 0.1 and 0.2 Å at $V = 10$ mV. Depending on the bias voltage, the single incorporated atoms appear as protrusions or as depletions. This behavior is well understood in terms of the localization of the Ag(111) surface state at the embedded Pb atom [64]. At lower coverages than presented in Fig. 3.1, Friedel oscillations due to the scattered electrons of the Ag(111) surface state around the Pb atoms and small clusters can be observed. Hence, the surface around the Pb atoms and small clusters is the clean Ag(111) surface, which is also confirmed by STS.

Inspecting the Pb atom distribution of Figure 3.1, at first sight there is a seemingly long-range order of the Pb atoms. It appears as if the Pb atoms arrange in favor of specific atom separations. Hence, the question arises whether

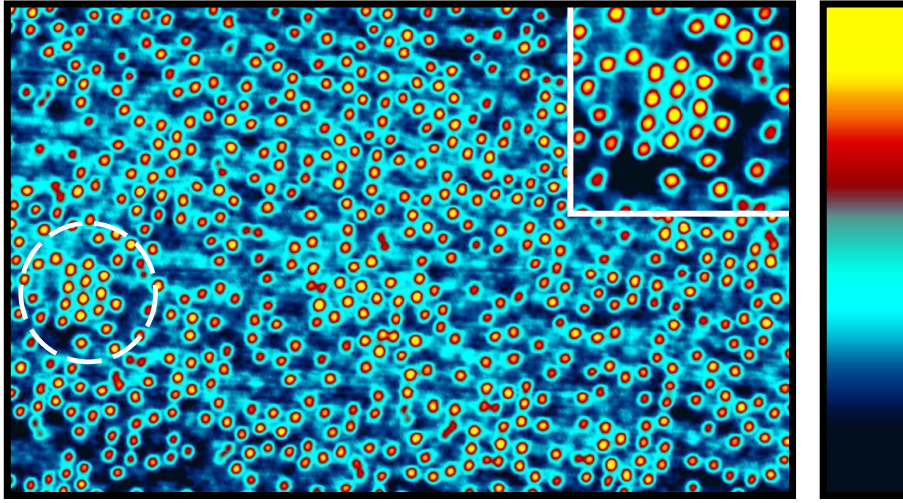


Figure 3.1: Topograph of 0.1 ML Pb of the disordered Pb/Ag surface alloy ($20 \times 12.5 \text{ nm}^2$, $V = 10 \text{ mV}$, $I = 60 \text{ nA}$). The white dashed circle highlights a region where the $(\sqrt{3} \times \sqrt{3}) \text{R}30^\circ$ phase starts to form (see inset for zoom). The full colorscale corresponds to a height difference of 0.26 \AA .

the annealing procedure lead to an equilibrium distribution of the Pb atoms which is governed by, e.g., a substrate mediated long-range interaction as it has been found for Cu atoms on Cu(111) [65]. There a long-range oscillatory interaction between the Cu adatoms mediated by two-dimensional surface state electrons was evidenced. In addition, highlighted by the white dashed circle, small regions of local hexagonal order can be identified (see inset in Fig. 3.1 for close-up view). The nearest neighbor distance within the ordered region is $4.9 \pm 0.2 \text{ \AA}$ in agreement with the 5 \AA in-plane lattice constant of an ordered Ag_2Pb $(\sqrt{3} \times \sqrt{3}) \text{R}30^\circ$ surface alloy (Ag in-plane lattice constant 2.89 \AA). For a schematic sketch of the ordered Ag_2Pb alloy structure see Figure 3.3.

To investigate the existence of a long-range interaction of the Pb atoms an autocorrelation analysis of the Pb distribution was performed. The autocorrelation describes how well an image correlates with itself under conditions where the image is displaced with respect to itself in all possible directions. Figure 3.2(a) shows a STM topograph of the disordered surface alloy with a coverage of 0.1 ML (Note, Fig. 3.1 shows a subrange of Fig. 3.2(a)). The single embedded Pb atoms appear as bright spots. In order to account only for the Pb atoms and to remove artifacts due to standing wave phenomena of the Ag(111) surface state, the au-

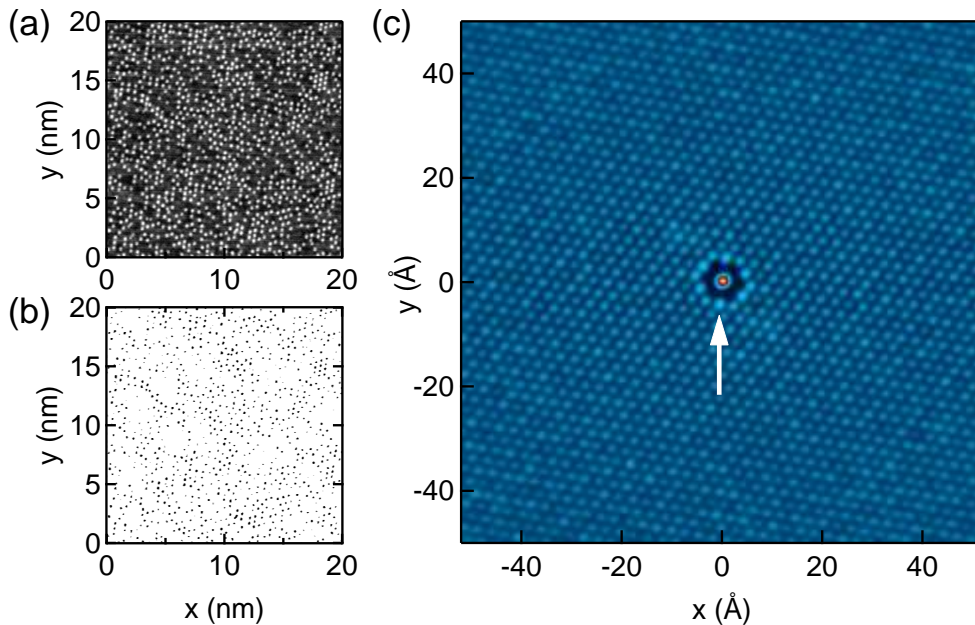


Figure 3.2: (a) STM topograph of 0.1 ML Pb (bright spots) on Ag(111) (increasing brightness corresponds to an increasing height), (b) binary representation of (a) as explained in the text (threshold value: 70% of the maximum height of the embedded Pb atoms), (c) self-correlation of (b). (c) uses the same colorscale as Fig. 3.1.

to correlation analysis of the Pb atom distribution (Fig. 3.2(c)) was performed using a binary representation (Fig. 3.2(b)) of the topograph shown in (a). Figure 3.2(b) has been obtained by assigning surface areas the value 1 (black) when they exhibit a height which is larger than 70% of the maximum height of the embedded Pb atoms. Otherwise, the value 0 (white) was assigned.

The autocorrelation of Figure 3.2(b) is shown in Fig. 3.2(c). A hexagonal lattice with Ag(111) in-plane lattice constant can be identified. The peak at the center of the autocorrelation image (ACI) corresponds to the virtual position of a Pb atom. The height at this position has been normalized to 1. The height of all other hexagonal lattice sites of the ACI may be interpreted as a probability for finding a Pb atom at that very location given that a Pb atom is located at the center of the image. The appearance of the Ag substrate lattice in the ACI evidences that the embedded Pb atoms acquire Ag lattice sites. The dark ring around the center position reflects the fact that neighboring Pb atoms occupy

second-nearest neighbor (SNN) Ag lattice sites. This can be understood in terms of the size mismatch of Pb and Ag atoms. The in-plane bulk lattice constants of Pb(111) and Ag(111) are 3.50 Å and 2.89 Å, respectively. The Pb atoms are too large such that repulsive forces prevent that two Pb atoms occupy neighboring Ag lattice sites. Consequently, the diminished occupation probability of the nearest neighbor lattice sites causes an increased occupation probability of the SNN and third-nearest neighbor (TNN) sites. As can be seen in Figure 3.2(c) the SNN and TNN make up a hexagon consisting of 12 virtual lattice sites centered at the origin of the ACI. Within the hexagon the SNN and TNN position alternate. One of the SNN positions is highlighted by a white arrow. Comparing the height of SNN and TNN, the occupation probability of the SNN position is $\approx 10\%$ larger as compared to the TNN site. This may indicate a slight preference for hexagonal order according to the Ag_2Pb ($\sqrt{3} \times \sqrt{3}$) R30° alloy structure to the disadvantage of a strictly disordered surface alloy already at coverages of 0.1 ML Pb.

However, except for the above mentioned findings the ACI does not reveal any further long-range order of the Pb atom distribution at this coverage. The height fluctuation of all other lattice sites are within the uncertainty margins. According to the current data basis the existence of a substrate mediated long-range order of the Pb atoms cannot be evidenced. Rather, it appears that the seemingly long-range order of the Pb atoms may be understood in terms of the Ag lattice acting as a long-range ordered template for the Pb absorption sites. The Pb atoms are randomly distributed (except for the SNN minimum separation) throughout the Ag lattice template, thereby giving the erroneous impression of long-range order.

For increasing coverage up to 1/3 ML, the disordered alloy phase vanishes. The Pb atoms rearrange such that large scale ($\approx 50 \times 50 \text{ nm}^2$) domains of the ordered ($\sqrt{3} \times \sqrt{3}$) R30° alloy phase develop, which cover the whole surface [43, 58–60]. This behavior is similar to Pb/Cu(111) where a disordered alloy consisting of local ($\sqrt{3} \times \sqrt{3}$) R30° and $p(2 \times 2)$ ordered patches is reported [66]. Figure 3.3 shows a schematic sketch of the ordered alloy structure. The blue and gray dots represent the Ag and Pb atoms, respectively. The green and the red hexagons highlight the hexagonal unit cells of the undistorted Ag and Pb lattices, respectively. Note, that due to the symmetry of the ordered Ag_2Pb alloy,

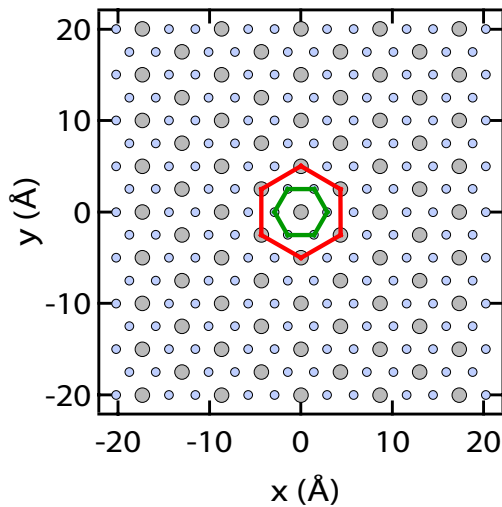


Figure 3.3: Schematic sketch of the ordered $(\sqrt{3} \times \sqrt{3})$ R30° Ag₂Pb alloy structure. The blue and gray dots represent the Ag and Pb atoms, respectively. The green and the red hexagons, highlight the hexagonal unit cells of the undistorted Ag and Pb lattices, respectively.

three commensurate domains with different occupation sites of the Pb atoms can develop.

Further increase of the Pb coverage to 1 ML leads to a segregation of the Pb atoms from the substrate which results in a hexagonal Pb overlayer wetting the Ag(111) surface (see below).

3.2 The Wetting Layer

For coverages of 1 ML the de-alloying process is almost complete and the Pb atoms are rearranged into a hexagonal ordered overlayer, which is wetting the complete surface. The average in-plane lattice constant is 3.5 ± 0.1 Å and matches well with the (111) in-plane bulk lattice constant of 3.5 Å. The WL exhibits a moiré-type hexagonal superstructure with a supercell length of 16 ± 0.5 Å [56]. For a moiré pattern to be formed, the lateral stiffness of the film has to be large compared to the binding energy of the substrate, such that the first adsorbed monolayer displays almost the geometric structure of a freestanding monolayer.

Fig. 3.4(a) shows an atomically resolved image of the WL. The atomic lattice with the moiré superstructure can be clearly identified. Furthermore, additional protrusions consisting of 2 to 5 Pb atoms, exhibiting an increased apparent height of $0.1 - 0.2$ Å are observed (red/yellow colored atoms). Similar protrusions have been also observed for Pb/Cu(111) [66]. Since the heights of the clusters

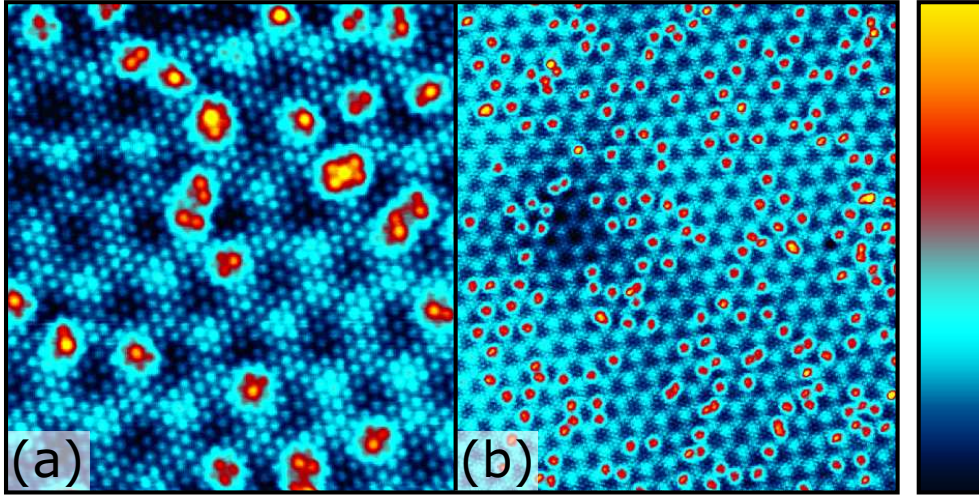


Figure 3.4: Topograph of the wetting layer acquired with $V = 100$ mV, $I = 250$ nA, (a) 10.4×11.3 nm, (b) 27×30 nm². The full colorscale corresponds to a height difference of (a) 0.62 Å and (b) 0.86 Å.

correspond to the apparent heights of embedded Pb atoms ($0.1 - 0.2$ Å) in the sub-monolayer regime, it is likely that the de-alloying process is not complete and that below the WL there are still embedded Pb atoms in the first Ag layer. Fig. 3.4(b) shows a larger scale image of the WL. The fact that the protrusions never occur at the topographic minima of the moiré structure will be discussed below. The dark area on the left may be due to a subsurface Ar-filled nanocavity implanted in the Ag(111) substrate during the sputtering/annealing procedure [67–69].

The lattice mismatch between the Pb(111) WL and the Ag(111) substrate is $\approx 21\%$ (The Pb(111) and Ag(111) in-plane bulk lattice constants are 3.50 Å and 2.89 Å, respectively). For the Pb overlayer it is known that there are two equivalent domains of the moiré structure, rotated by $\pm(4.5 \pm 0.2)^\circ$ [56]. A schematic sketch of one of the rotated domains using the undistorted Pb and Ag lattices is shown in Figure 3.5. The small yellow hexagon in the middle highlights the hexagonal unit cell of the Pb lattice while the larger red hexagon represents the hexagonal unit cell of the moiré reconstruction which is denoted by $(\sqrt{28} \times \sqrt{28})$ R19.1° with respect to the Ag substrate, or $(\sqrt{19} \times \sqrt{19})$ R23.4° with respect to the Pb lattice.

While Fig. 3.5 is based on the undistorted lattices, it has been shown that

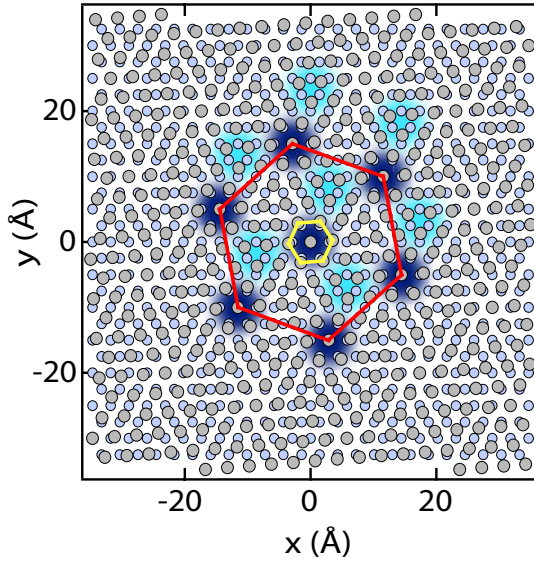


Figure 3.5: Schematic sketch of the moiré structure of the wetting layer of Pb/Ag(111). The blue and gray dots represent the Ag and Pb lattice, respectively. The Pb lattice is rotated by 4.3° with respect to the Ag lattice. The yellow and the red hexagons, highlight the hexagonal unit cells of the undistorted Pb lattice and of the moiré reconstruction, respectively. The dark and light blue background correspond to the topographic minima and maxima of the moiré pattern, respectively [56].

the atomic positions are modulated mainly perpendicular to the surface [56]. This result was obtained using the embedded atom method for structure calculations. According to the calculations presented in Ref. [56] the dark and light blue background in Figure 3.5 highlight the regions of the moiré structure which correspond to the topographic minima and maxima, respectively. Hence, the on-top position of the Pb atom is connected with the topographic minima of the moiré pattern. This result is referred to as inverse corrugation (see Ref. [51] and references therein). Furthermore, the out-of-plane modulation of the atom positions in the Pb layer was found to be 0.09 \AA , whereas the modulation of the Ag atoms in the top layer amounts to 0.32 \AA . A qualitatively similar result has been obtained for a Pb overlayer on Cu(111). For the Pb/Cu(111) system, the Pb overlayer induced modulation of the substrate surface has been proposed to be related to the surface-active (surfactant) role of Pb [55].

According to the structural model of the moiré pattern, the protrusions (see Fig. 3.4 (a) (b)), which are probably due to the incomplete de-alloying, never occur at the lattice sites which correspond to the on-top position of the Pb atoms. This result may be understood in terms of the reduced coordination number of an Pb overlayer atom in on-top position as compared with a Pb overlayer atom in a bridge position. The lower coordination of a Pb atom in on-top position

over an embedded Pb atom possibly results in enhanced repulsive forces [51], which make the de-alloying process energetically favored at the on-top positions. Hence, it appears that the specific surface morphology at these locations prevents the occurrence of embedded Pb atoms in close proximity to the on-top sites.

3.3 Pb Islands

After completion of the WL, further Pb deposition results in three-dimensional island growth. The Pb islands preferentially emerge from Ag terraces which are bounded towards the upper lying terraces by Ag double-steps. Figure 3.6(a) shows a topograph of a 3 ML thick Pb film (orange colored region on the right) emerging from such an Ag double-step. The blue colored region on the left shows the Pb WL. The moiré structure from the WL can also be recognized on the Pb island. However, the protrusions observed on the WL, which we assign to the incomplete de-alloying, are not found on the Pb film. Hence, Pb islands and the WL can easily be distinguished by inspecting STM topographs. Additionally, dI/dV spectra clearly reveal the different electronic structure and hence the

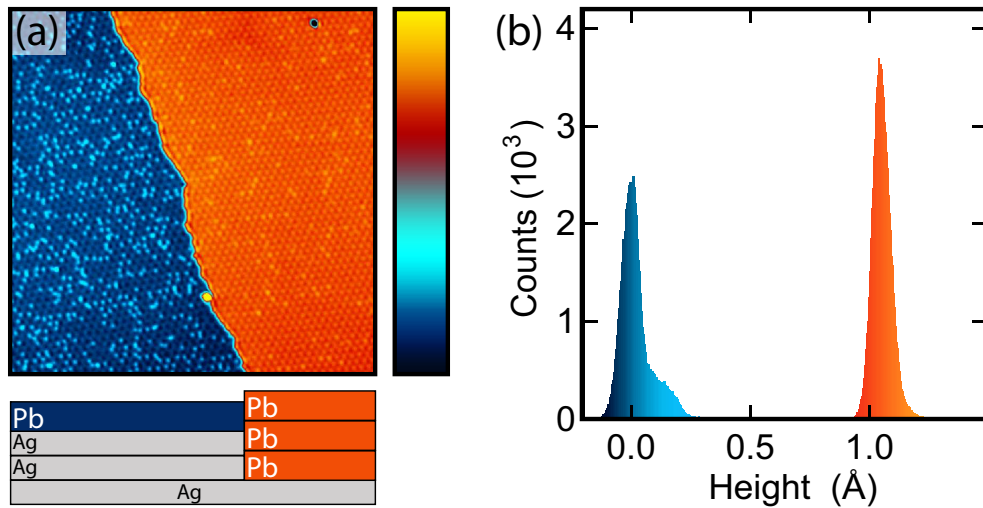


Figure 3.6: (a) shows a topograph of a 3 ML thick Pb film (orange colored region on the right). The blue colored region on the left shows the Pb WL ($74 \times 74 \text{ nm}^2$, $V = 200 \text{ mV}$, $I = 0.2 \text{ nA}$). Below the topograph is a schematic sketch of the cross-sectional profile of the Pb thin film structure. (b) shows a height distribution of the topograph shown on the left.

different thickness of the Pb films (see Chapter 4). Below the topograph is a schematic sketch of the cross-sectional profile of the Pb thin film. The height of an Ag(111) (gray colored) and Pb(111) layer are 2.36 \AA and 2.86 \AA , respectively (Pb blue and orange colored; different color code for Pb only for consistency with shown image). Hence the geometric height of the step in Fig. 3.6(a) should correspond to 1 \AA . Figure 3.6(b) shows a height histogram of the topograph shown on the left. The average height of the undistorted WL has been set to 0 \AA . While the protrusions on the WL result in a shoulder-like feature located at 0.13 \AA , the histogram peak of the Pb island does not exhibit such a shoulder and points to the flat-top growth of Pb islands. The average height difference of the WL and the island of 1.04 \AA is in very good agreement with the theoretical geometric height. However, due to the existence of quantum well resonances within the Pb films (see chapter 4) step heights as measured by STM exhibit voltage dependent variations. To minimize this effect, topographs should be acquired with voltages close to 0 V .

Figure 3.7(a) shows an image of Pb islands (gray) protruding from the WL (blue) of Pb/Ag(111). On Pb islands, which extend over several adjacent Ag terraces, the difference in interlayer spacing between Pb (2.86 \AA) and Ag (2.36 \AA) causes a dislocation running from the Pb/Ag interface to the surface. This produces a step of 0.5 \AA height at the island surface. These dislocation lines are clearly visible in the shown image Fig. 3.7(a) and are used to discriminate different island thicknesses (one of the dislocation lines is highlighted by a white arrow). The image has been processed by adding contributions of the Laplacian filtered image to enhance the contrast of steps and dislocation lines.

It is found that the moiré structure is still present at coverages up to 37 ML. As shown by Altfeder *et al.* for Pb/Si(111) this is caused by an adiabatic shift of quantum well resonances due to lateral variations of the electronic reflection phase at the buried interface and is not a sign of unrelaxed strain within the Pb islands [70]. Figure 3.7(b) shows a zoom in to a Pb island. The image has been processed by adding contributions of the Laplacian filtered image to enhance the contrast of the moiré pattern. Four different terraces are shown. The thickness of the Pb film increases from 24 ML at the lower left to 27 ML at the upper right. It is found that the contrast of the moiré pattern on the different terraces reverses when the film thickness is increased by 1 ML [70]. This is due to the

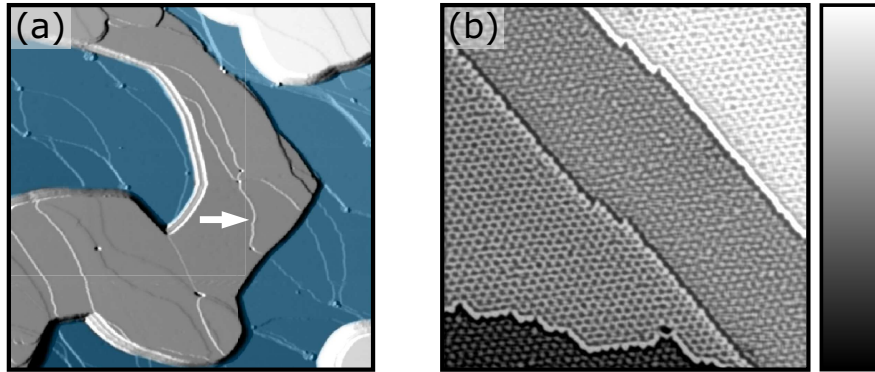


Figure 3.7: (a) Processed image of Pb islands on Ag(111) ($600 \times 600 \text{ nm}^2$, $V = 0.2 \text{ V}$, $I = 5 \text{ nA}$). Ag steps are clearly 'shining through' the Pb island. (b) Processed image of a Pb film with 24-27 ML Pb from lower left to upper right ($60 \times 60 \text{ nm}^2$, $V = 0.1 \text{ V}$, $I = 2.6 \text{ nA}$).

specific ratio of interlayer spacing a and Fermi wavelength λ_F ($\lambda_F/a \approx 4$) along the [111] crystallographic direction of Pb, which causes a modulation of the electron density of states near the Fermi level E_F with bilayer periodicity (Due to the slight mismatch of λ_F and $4a$, a beating pattern with a 9-layer periodicity is superimposed to the bilayer modulation [16]). Furthermore, similar to Pb adsorbed on Cu(111) and Si(111) some island heights —2, 4, 5, 7, and 9 ML in the present case of Pb/Ag(111)— are hardly observed [22, 71, 72].

CHAPTER 4

Electronic Structure of Pb/Ag(111)

The quantum confinement of electronic states in thin Pb(111) films has attracted considerable interest for almost 40 years [73, 74]. When the thickness of a Pb film is reduced to the nanoscale, confinement of electrons results in discrete energy levels associated with so-called quantum well states (QWSs). The specific ratio of interlayer spacing a and Fermi wavelength λ_F ($\lambda_F/a \approx 4$) along the [111] crystallographic direction of Pb causes a modulation of the electron density of states near the Fermi level E_F with bilayer periodicity. Hence, increasing the film thickness by one atomic layer has a significant impact on the physical and chemical properties of the films [2] as shown for, e.g., the electrical resistivity [1], superconducting transition temperature [13], Hall coefficient [14], surface energy [15], work function [16, 17], roughening temperature [75], step height [76], electron-phonon coupling [18], and chemical reactivity [19]. By means of scanning tunneling microscopy (STM) and spectroscopy (STS) of these quantum well structures it is possible to gain information on the band structure, scattering phase shifts, interface reflectivity, and quasiparticle lifetimes of occupied as well as unoccupied states. The quasiparticle lifetime sets the duration of excitations and, in combination with the group velocity, determines their mean free path. Excited electrons play an essential role in many physical and chemical surface processes, such as energy transfer, electronically induced adsorbate reactions, catalytic processes and epitaxy [12, 77]. For understanding these surface processes on thin metal films, it is therefore of fundamental importance to study the decay of electronic excitations within these films. Theoretical lifetime studies of Pb films have already been performed for freestanding Pb and for Pb films

on Cu(111) [78, 79]. Experimentally, it has been found that for Pb films on Si(111) the lifetime broadening exhibits a quadratic energy dependence as also found theoretically for freestanding Pb [78]. Contrary to this finding, the theoretical results for Pb/Cu(111) suggest a rather linear dependence of the lifetime broadening on E for energies above $E_F + 1$ eV [79]. However, for Pb on closed-packed noble metal surfaces, experimental results for the quasiparticle lifetimes are lacking.

Here, we report on a detailed STS study of QWSs in thin Pb(111) films grown on Ag(111) in the thickness range from 1 to 37 monolayers (ML). From the QWS energies as a function of film thickness, the bulk-band dispersion along Γ -L is derived in the energy region from -0.5 eV to $+3.5$ eV around E_F . Simple models of scattering at the two boundaries of the Pb film, *i. e.*, the vacuum barrier and the inverted *sp*-band gap of the Ag(111) interface yield a rather accurate description of the energy dependence of the scattering phase shift Φ [80]. Moreover, the widths of the spectroscopic features of the QWS are analyzed, giving insight into hot-electron and hot-hole dynamics in Pb films on Ag(111).

Experiment: Electrochemically etched W tips were prepared by annealing cycles and indenting into Pb islands, thereby covering the tip apex with Pb. Spectra of the differential conductance (dI/dV) were acquired by using standard lock-in detection (modulation amplitude 2.5 mV_{rms}, frequency 10 kHz).

4.1 Phase Accumulation Model

For our study we utilize the phase accumulation model (PAM) [82, 83] which has been very successful in the interpretation of image and surface states on clean metals and of QWSs in layered noble metal systems [84].

The physics of this multiple reflection approach is illustrated schematically in Fig. 4.1. In the energy range of a bulk band gap, an incident electron will be reflected by the crystal. If the electron energy is also below the vacuum level E_V , the electron will be reflected back again by the surface barrier. It is therefore trapped between the crystal barrier, located at z_C , and the image potential surface barrier. For constructive interference, the round-trip phase accumulation

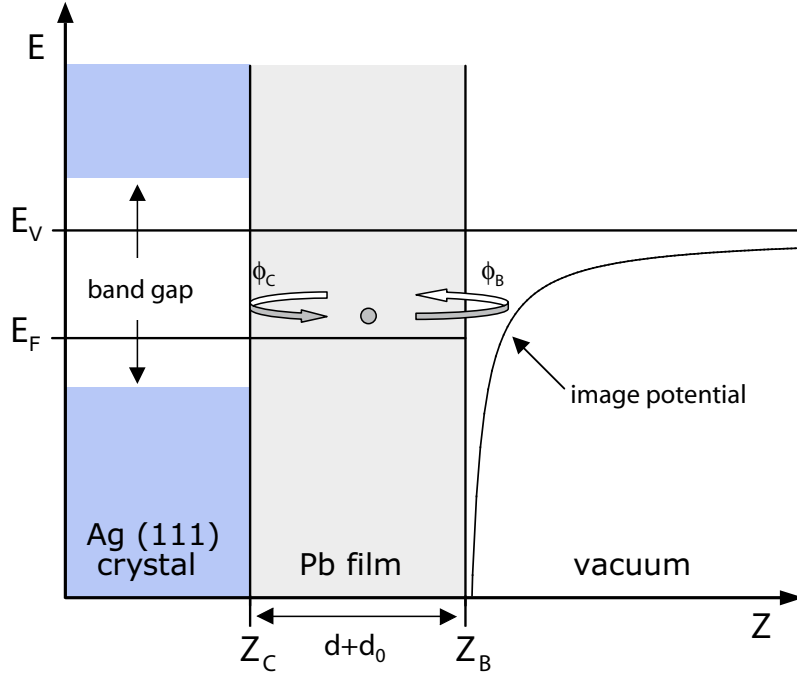


Figure 4.1: Schematic diagram showing the multiple reflection (phase accumulation) model used to describe the electron bound states in a thin Pb film on an Ag(111) surface. The electron confinement is caused by the image potential on the vacuum side and the Ag(111) band gap at the Pb/Ag interface (adopted from Ref. [81]).

associated with the propagation between the barriers and the phase shifts associated with the reflections at the boundaries must be an integer multiple of 2π , then a standing wave solution corresponding to a bound state occurs.

Hence, the quantization condition for the existence of such states, which is based on the Bohr-Sommerfeld quantization rule, can be written as

$$2k(E)(d + d_0) + \Phi = 2\pi n, \quad (4.1)$$

where $\Phi = \Phi_C + \Phi_B$ is the sum of the phase shifts on reflection at the crystal Φ_C and at the vacuum barrier Φ_B , $k(E)$ is the energy dependent wave vector of an electron propagating along the Γ -L direction of Pb in a slab of thickness $z_B - z_C = d + d_0$. $d = aN$ is the nominal thickness, with N the number of atomic layers, and $a = 2.86 \text{ \AA}$. d_0 is a constant offset which accounts for the displacement of the position of the Pb/Ag interface and of the image plane with respect to

the jellium edges of the film due to the spill-out of electrons on both sides of the slab [2]. We assume d_0 to be independent of N and use it as a fit parameter. The integer quantum number n corresponds to the number of half-wavelengths of the wave function inside the slab. For Φ_B we have used the WKB expression [85]:

$$\Phi_B = \pi [3.4 \text{ (eV)} / (E_V - E)]^{1/2} - \pi, \quad (4.2)$$

with E_V the vacuum level. The fact that the image potential barrier extends beyond the terminating plane z_B is accounted for in the expression for Φ_B . E_V has been shown to vary with bilayer periodicity [16, 17]. Here we fix a single value for all layer thicknesses and use E_V as a fit parameter. The interface phase shift Φ_C can be calculated from a simple two-band model of the substrate. Φ_C should vary from 0 to π across the inverted sp -band gap of Ag(111), varying rapidly with E at the band edges [81, 83]. We have used the empirical expression [80, 86]:

$$\Phi_C = 2 \arcsin [(E - E_L) / (E_U - E_L)]^{1/2}, \quad (4.3)$$

where E_U and E_L are the energies of the upper and lower edges of the projected band gap in Ag(111), respectively. Here $E_L = -0.4$ eV and $E_U = 3.9$ eV [87] (Energies are measured with respect to the Fermi level of the sample.). Figure 4.2 shows the scattering phase shifts Φ_C (blue) and Φ_B (red) as a function of energy E for $E_V = 4.5$ eV, and E_L and E_U as given above.

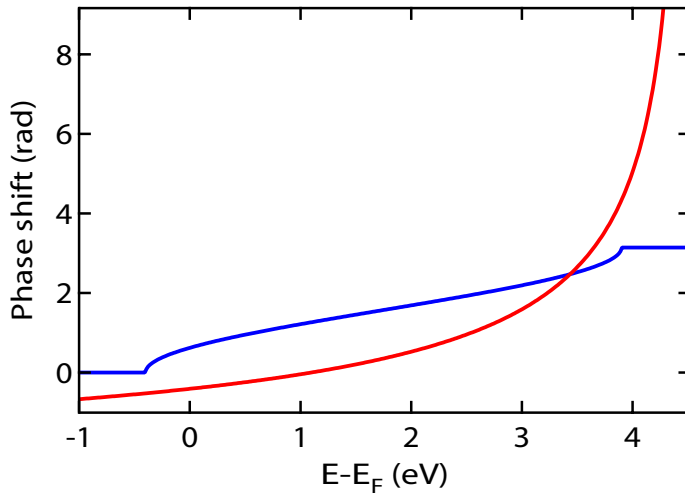


Figure 4.2: Scattering phase shifts Φ_C (blue) and Φ_B (red) as a function of energy E . $E_V = 4.5$ eV, $E_L = -0.4$ eV, and $E_U = 3.9$ eV.

Note, that the term inverted sp -band gap is used to specify a band gap, where the state at the bottom of the gap is p -like, with charge accumulating between the atoms as expected for a bonding state, whereas at the top of the gap the state is s -like, with charge concentrated on the atoms and thus having anti-bonding character. The inversion is relative to free atoms in which s -states generally have lower energies than p -states.

4.2 Quantum Well State Energies

A collection of representative constant-current dI/dV spectra acquired atop of various island heights is displayed in Fig. 4.3. The spectra show a number of unoccupied states. Similar spectra have been found in Pb islands on Cu(111) [88]. The peak positions correspond to the extracted QWS energies of each island and are highlighted by solid triangles (Fig. 4.3(b)). For sample voltages $V < 1$ V, the peak structure displays a shoulder towards higher voltages. For $V > 1$ V the peaks become more symmetric. This is due to the specific band structure of thin Pb films [89]. In constant-height dI/dV spectra the states at $V < 1$ V

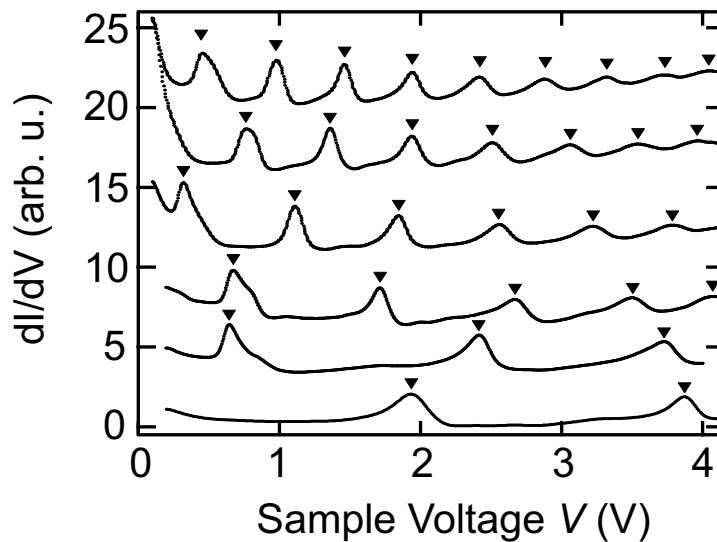


Figure 4.3: Representative constant-current dI/dV spectra acquired on Pb islands with film thicknesses of 3, 6, 12, 17, 22, and 27 ML from bottom to top, respectively ($I = 5$ nA). Triangles indicate the extracted QWS energy. Spectra are vertically shifted for clarity.

exhibit boxshaped lineshapes with an arctan-like onset as will be discussed in more detail in Sec. 4.4 (see also Fig. 4.8).

Figure 4.4 shows the layer resolved QWS energies versus island height for Pb/Ag(111) numbered in monatomic layers. Dots and triangles are obtained from constant-current (cf. Fig. 4.3(b)) and constant-height dI/dV respectively. Open squares show QWS energies calculated as described in the following. As mentioned before, similar to Pb adsorbed on Cu(111) and Si(111) some island heights —2, 4, 5, 7, and 9 ML in the present case— are hardly observed [22, 71, 72]. For $V < 1$ V, the QWS energies are determined from the constant-height data as the midpoint of the onset of the arctan-like spectral feature [90]. For $V > 1$ V the peak position of the Lorentzian-like lineshapes is used.

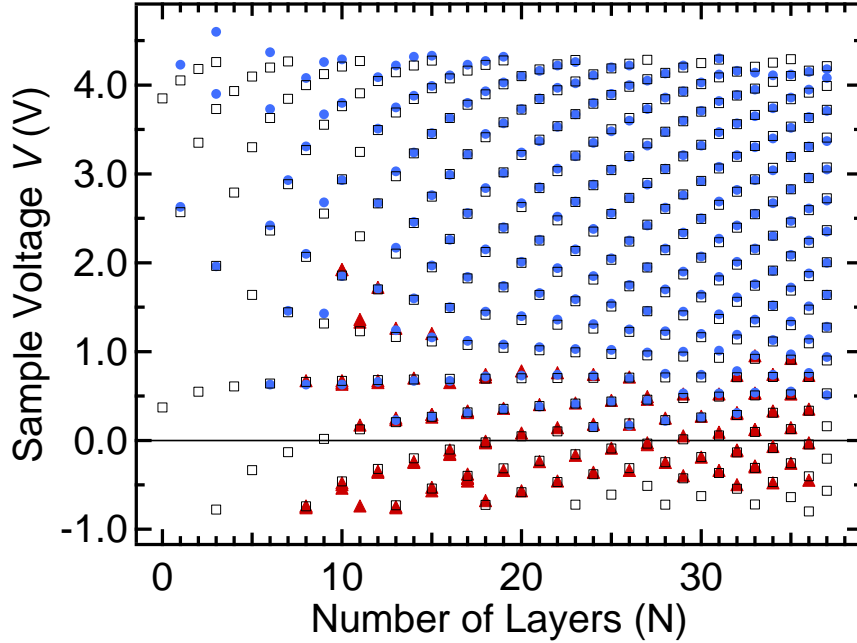


Figure 4.4: QWS energies versus island height for Pb on Ag(111) numbered in monatomic layers. Dots and triangles are obtained from constant-current and constant-height dI/dV respectively. Open squares show calculated QWS energies as described in the text ($v_g = 13.19 \text{ eV}\text{\AA}$, $k_F = 1.592 \text{ \AA}^{-1}$, $d_0 = -0.18 \text{ \AA}$, and $E_V = 4.5 \text{ eV}$).

The sections below are organized as follows. In Sec. 4.3, the bulk dispersion along Γ -L is derived and the scattering phase shifts are analyzed. In Sec. 4.4, we

analyze the onset-widths of the spectroscopic signals of the QWSs, giving insight into hot-electron and hot-hole dynamics in the Pb films.

4.3 Band Structure and Scattering Phase Shifts

From the energies of the QWSs as a function of film thickness, the bulk band dispersion along the Γ -L direction can be derived. Fig. 4.4 displays the layer resolved QWS energies. For the determination of the quantum number n of each QWS, we utilize the fact that the energy of the particular QWS located at ≈ 0.65 eV on islands consisting of an even number of Pb layers is rather independent of the slab thickness. It has been shown that the wave vector k of this state is $3\pi/2a$ [91]. Hence, the corresponding quantum number n for all QWSs shown in Fig. 4.4 (dots and triangles) can be derived [88].

The sum of the thickness-independent phase shifts $\Phi_{t-i} = \Phi_C + \Phi_B + 2k(E)d_0$ depends only on the electron energy. Hence, the wave vector $k(E)$ at a given energy can be derived from the QWSs at that energy. Consider N_1 and N_2 , corresponding to film thicknesses of two QWSs at the same energy $E = E_1 = E_2$ with quantum number n_1 and n_2 , respectively. Eq. (4.1) leads to

$$k(E) = \pi(n_2 - n_1) / [(N_2 - N_1)a]. \quad (4.4)$$

In view of the uncertainty margins in determining QWS energies from dI/dV spectra, we applied Eq. (4.4) to pairs of QWSs whose energies differ by less than 30 meV, *i. e.*, $|E_2 - E_1| \leq 30$ meV. Fig. 4.5 summarizes the results for the dispersion along Γ -L in an extended Brillouin zone scheme. The band exhibits an approximately linear relation between E and k over the entire energy range.¹ The slope of the dispersion relation converts to a constant group velocity $v_g = 13.19$ eVÅ and a Fermi wave vector $k_F = 1.592$ Å⁻¹. The result for k_F is very close to the value from angle-resolved photoemission spectroscopy, $k_F = 1.598$ Å⁻¹, and de Haas-van Alphen measurements, $k_F = 1.596$ Å⁻¹ [18, 92, 93]. It is

¹ The piling up of data points around $k = 3\pi/2a = 1.648$ Å⁻¹ and $k = 5\pi/3a = 1.831$ Å⁻¹ is due to the finite energy window of 30 meV used to determine $k(E)$. The piling can be removed by reducing the energy window. However, the resulting slope of the dispersion is not affected when changing the energy window to 3 meV.

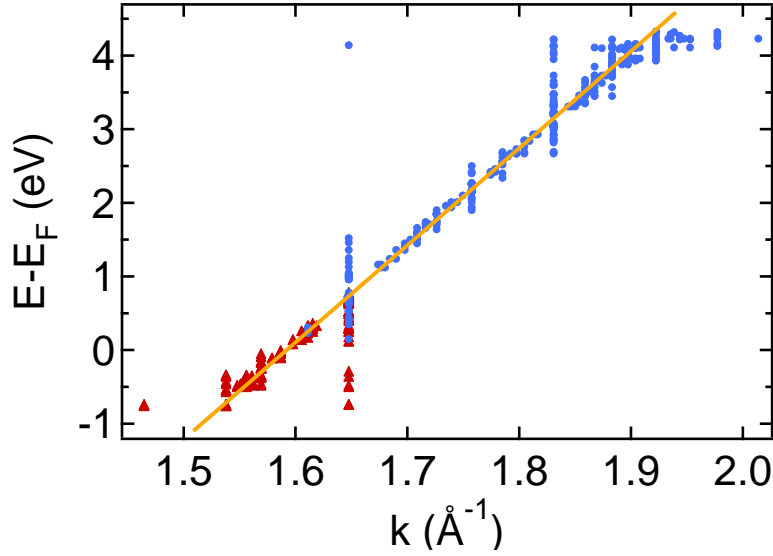


Figure 4.5: Bulk band dispersion along the Γ -L direction shown in the extended Brillouin zone scheme. Data from constant-current and constant-height data are indicated by dots and triangles, respectively. A linear fit (solid line) yields $v_g = 13.19 \text{ eV}\text{\AA}$ and $k_F = 1.592 \text{ \AA}^{-1}$.

important to note that the dispersion relation of Fig. 4.5 has been obtained without using the scattering phase shift at the vacuum barrier. Thus, our result would not be affected by a STM-induced Stark-shift [94].

Using the above derived linear dispersion relation along Γ -L, we can now calculate the scattering phase shifts from the experimental data. Fig. 4.6 shows the resulting Φ_{t-i} (dots and triangles). A solid line shows Φ_{t-i} as calculated from Eqs. (4.1),(4.2), and (4.3). Given the expressions for Φ_B and Φ_C we find that the experimental data is best described with $d_0 = -0.18 \text{ \AA}$ and $E_V = 4.5 \text{ eV}$. Figure 4.6 shows that simple models for the scattering phase shift yield a rather accurate description for the experimentally observed Φ_{t-i} over the entire energy range investigated here. The divergence of Φ_B for $E \rightarrow E_V$ is clearly observable and points to the massive impact of the vacuum barrier phase shift on the energetic positions of the higher lying QWSs. $E_V = 4.5 \text{ eV}$ as found here compares well with $E_V = 4.6 \text{ eV}$ as inferred from STS data of Pb QWSs on Cu(111) [88]. Furthermore, the very good agreement of calculated QWS energies, using the PAM together with the derived values for $v_g = 13.19 \text{ eV}\text{\AA}$, $k_F = 1.592 \text{ \AA}^{-1}$,

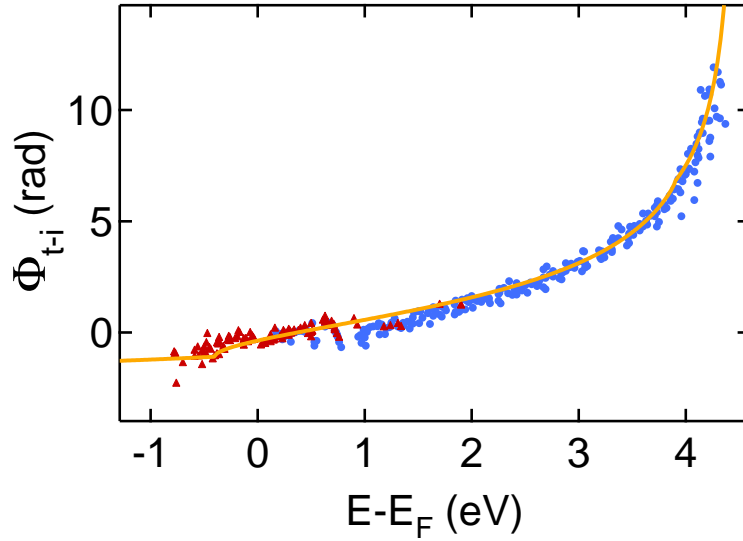


Figure 4.6: Φ_{t-i} , sum of the thickness-independent phase shifts. Data from constant-current and constant-height data are indicated by dots and triangles, respectively. Φ_{t-i} as calculated from Eqs. (4.1),(4.2), and (4.3) with $v_g = 13.19 \text{ eV}\text{\AA}$, $k_F = 1.592 \text{ \AA}^{-1}$, $d_0 = -0.18 \text{ \AA}$, and $E_V = 4.5 \text{ eV}$ is shown as a solid line.

$d_0 = -0.18 \text{ \AA}$, and $E_V = 4.5 \text{ eV}$, and the experimental data as shown in Fig. 4.4 is remarkable.

4.4 Linewidths and Lifetime Broadening

In the following, we discuss the spectral linewidths of the Pb/Ag(111) QWSs. Figure 4.7 shows the projected band structure of the QWSs of an 8 ML Pb film along the high-symmetry directions (adopted from Ref. [95]). The dispersion of the QWSs shows a quasifree-electron-like dispersion near the zone center $\bar{\Gamma}$, but at larger in-plane momenta the dispersion flattens and even turns toward higher binding energies [89, 95–97]. For QWSs at higher energies, the effective mass near $\bar{\Gamma}$ increases. For the unoccupied QWSs in the vicinity of $\bar{\Gamma}$, this can result in almost non-dispersive bands, yielding a Lorentzian lineshape in STS [98–100].

Figure 4.8 shows an exemplary constant-height dI/dV spectrum of an 36 ML Pb film. The shapes of the QWS features change with varying voltage. For

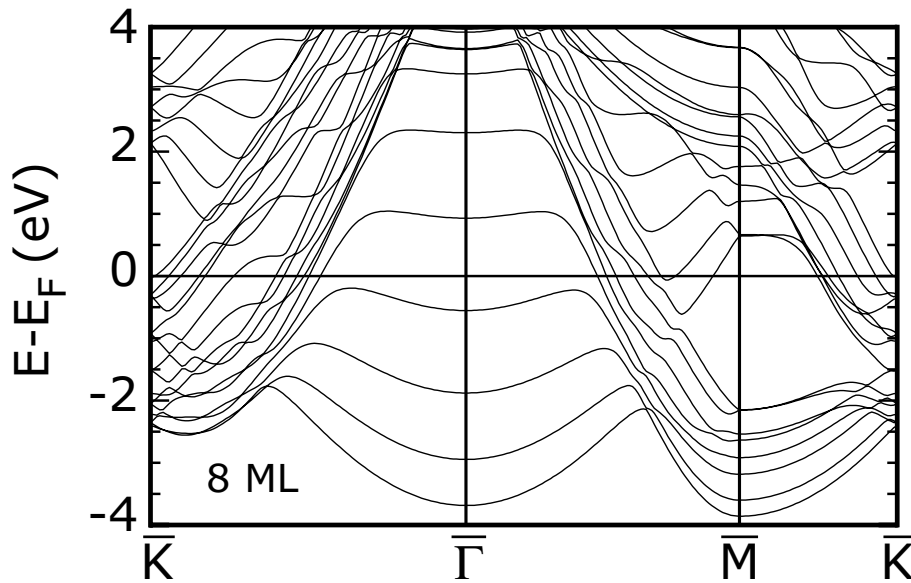


Figure 4.7: Projected band structure of a 8 ML Pb film along the high-symmetry directions. Data taken from Miyata *et al.* [95].

$V < 1$ V the QWSs give rise to box-shaped spectral features, while for $V > 1$ V the lineshapes are Lorentzian-like. We found that this energy dependence of the spectral lineshapes is universal for all investigated film thicknesses and we assign it to the peculiar band structure of the Pb QWSs.

Hence, for voltages below 0.9 eV we assume that the onset is well described by the arctan-shaped onset of a two-dimensional quasifree electron gas [90]. The steplike spectral features of the QWSs are in contrast to spectra measured on Pb/Si(111) where also the QWS below 1 V exhibit Lorentzian lineshapes [16, 78]. This difference in lineshape may be explained by the enhanced lossy interface scattering, induced by disorder at the Pb/Si interface as observed in Ref. [78], affecting the lineshape of the QWSs. Therefore, from observing the arctan-shaped onsets we infer that Pb films on Ag(111) exhibit a high-quality ordered interface.

As for QWSs with energies above 1 eV the observed spectral feature turns to a symmetric Lorentzian lineshape, the contribution of tunneling electrons with finite in-plane momenta decreases and should contribute less than 10 meV to the Lorentzian linewidth of the excitation at the $\bar{\Gamma}$ point [98, 99]. Hence, we

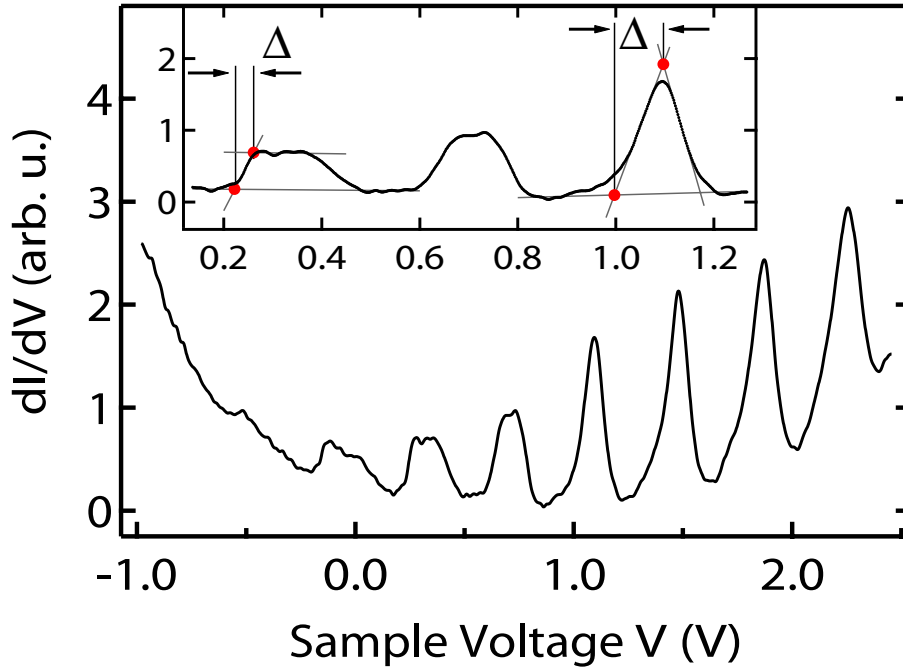


Figure 4.8: Exemplary constant-height dI/dV spectrum of 36 ML Pb. Inset shows a zoom in the same spectrum. The three gray lines on the left and on the right QWS indicate how the onset linewidths are determined for arctan-like QWS lineshapes (left) and a Lorentzian-like lineshape (right). Red dots highlight the intersection points, used to determine Δ .

assign Lorentzian lineshapes to QWSs with energies above 1.1 eV. For QWSs with energies ranging from 0.9 eV to 1.1 eV the distinction between arctan and Lorentzian lineshape is difficult and therefore we concentrate on QWS energies outside this energy range. In order to determine the lifetime broadening we analyze the QWSs onset widths following the surface state analysis of Li *et al.* described in Ref. [90]. To quantify the onset width, which we denote Δ , we adopt the geometrical definition illustrated in the inset in Fig. 4.8. For arctan-like features (left QWS) we extrapolate the slope at the midpoint of the rise to the continuation of the differential conductance above and below the onset. For Lorentzian-like features (right QWS) we extrapolate the slope at the steepest point of the rise to the continuation of the differential conductance below the onset and to the continuation of the steepest point of the trailing edge. The red dots highlight the intersection points, used to determine Δ .

We have also used constant-current dI/dV spectra to determine Δ . In order to minimize the distorting influence of the constant-current modulus on the observed lineshapes we normalize the constant-current dI/dV spectra to remove the influence of the changing tip-sample distance [38, 101].¹ We find that the normalization recovers the boxshaped QWS spectra for energies below 1 eV. For the unoccupied states we find that analyzing the two kinds of dI/dV spectra, *i. e.*, constant-height and normalized constant-current, yield linewidths which are in good agreement. This indicates the reliability of the normalization scheme also for linewidth determinations in the shown voltage range.

For arctan lineshapes, the lifetime broadening Γ_τ can be extracted from the geometrical onset width Δ as $\Gamma_\tau = (2/\pi)\Delta$ [77, 90]. For Lorentzian lineshapes it can be shown by means of simple lineshape analysis arguments that the geometrical onset width Δ as defined above relates to Γ_τ as $\Gamma_\tau = (2/\sqrt{3})\Delta$.

Figure 4.9 shows Γ_τ , obtained using the above mentioned lineshape analysis. We find that for energies below $E \approx -0.4$ eV, Γ_τ increases more rapidly as a function of $|E|$ than for positive voltages. We assign this to the lower band edge in Ag(111). Below the lower band edge at $E = -0.4$ eV the Pb QWSs turn into quantum well resonances due to the reduced confinement at the Pb/Ag interface. Thus, the elastic scattering rate of hole-like excitations in the quantum well rises, leading to the observed increase in Γ_τ [79, 102]. For energies within the inverted *sp*-band gap ($-0.4 \text{ eV} < E < 3.9 \text{ eV}$), we find that Γ_τ is independent of film thickness within the uncertainty margins. Hence, we assume the linewidth contribution due to the lossy interface scattering into the Ag(111) substrate to be rather small.

In the absence of defects within the Pb films, there are mainly three contributions to Γ_τ to be considered:

$$\Gamma_\tau = \Gamma_0 + \Gamma_{\text{e-p}}(E) + \Gamma_{\text{e-e}}(E). \quad (4.5)$$

¹ The dI/dV signal is divided by the transmission factor $T(V, \bar{z}) = \exp \left[-\bar{z} \sqrt{4m/\hbar^2 (\phi_s + \phi_t - eV)} \right]$ to obtain the normalized differential conductance dI/dV_N . We used $\phi_t = \phi_s = 4.5$ eV, and \bar{z} is calculated as $\bar{z}(V) = z(V) + 5 \text{ \AA}$ where $z(V)$ is the constant-current vertical tip displacement measured concomitantly with dI/dV .

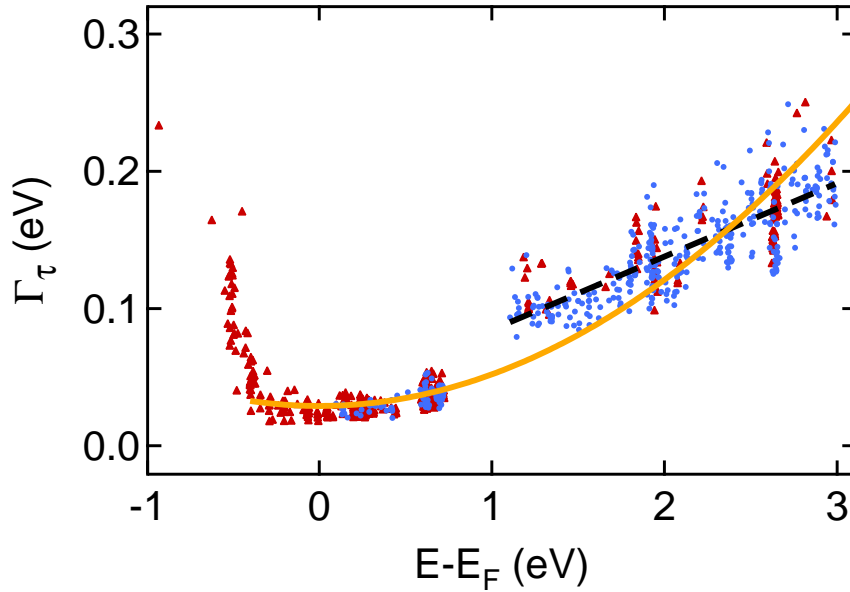


Figure 4.9: Lifetime broadening Γ_τ . Data from constant-current and constant-height data are indicated by dots and triangles, respectively. Solid orange line is a quadratic fit to the energy range from $E - E_F = -0.4$ eV to 3 eV. A dashed black line shows a linear fit for $E - E_F > 1$ eV.

$\Gamma_{e-e}(E)$ and $\Gamma_{e-p}(E)$ denote the electron-electron (e-e) and electron-phonon scattering rates, respectively. Γ_0 accounts for the lossy interface scattering. In Ref. [78], $\Gamma_{e-p}(E) \approx 20$ meV at E_F has been calculated for freestanding Pb at a temperature of 5 K. As $|\Gamma_{e-p}(E_F) - \Gamma_{e-p}(E)| < 10$ meV for $E \leq 2.5$ eV, we assume a constant contribution of Γ_{e-p} to the lifetime broadening over the energy range investigated here. From Fermi-liquid theory, as shown by Quinn-Ferrell, the e-e scattering is expected to exhibit a quadratic energy dependence for states close to E_F [103]. For Pb such a description yields, $\Gamma_{e-e}(E) = \alpha(E - E_F)^2$ with $\alpha = 0.027$ eV $^{-1}$. The solid orange line shows such a quadratic energy dependence fitted to our data in the energy range between -0.4 eV and 3 eV. The jump in Γ_τ that occurs at $E \approx 1$ eV is linked to the different lineshapes found for QWSs with energies below and above ≈ 1 eV. For the e-e scattering we find $\alpha = 0.023$ eV $^{-1}$ which compares very well with the Quinn-Ferrell value and with $\alpha = 0.026$ eV $^{-1}$ as measured by Hong and coworkers [78]. However, for energies above 1 eV a deviation of the quadratic energy dependence (shown by the dashed black line in

Fig.4.9) is observed. The fitted line has a slope of 53 meV eV^{-1} . A similar linear dependence has also been found theoretically for Pb islands on Cu(111) [79]. There it has been argued that the linear dependence is signaling deviations of the random phase approximation linewidth from simple quadratic dependence. The reported slope of 52 meV eV^{-1} is in good agreement with our measured data.

The fit also yields a constant offset of $\Gamma_0 + \Gamma_{e-p}(E_F) = 29 \text{ meV}$. Comparing this result with the above mentioned calculations for Γ_{e-p} of freestanding Pb, supports the assumption that the contribution of the lossy scattering to the lifetime broadening is small and of the order of $\Gamma_0 \approx 10 \text{ meV}$ at E_F . A similar analysis for the $\sqrt{3} \times \sqrt{3}$ and the 7×7 interface of Pb/Si yields $\Gamma_0 \approx 50 \text{ meV}$ and $\approx 140 \text{ meV}$ at E_F , respectively [78]. Hence, the Pb/Ag interface yields a better confinement than the Pb/Si interface and this possibly causes the observability of the box-shaped QWSs below $\approx 1 \text{ eV}$.

4.5 Summary

In summary, quantum well states in Pb(111) films up to 37 ML have been investigated. The thickness dependence of the QWS energies is found to be very well fitted with the phase accumulation model including energy dependent scattering phase shifts at the interface and the vacuum barriers. The dispersion along the Γ -L direction is shown to be well approximated by a constant group velocity of $v_g = 13.19 \text{ eV\AA}$. The Pb/Ag interface is found to be of high-quality, such that the lossy interface scattering contribution to the lifetime broadening is significantly reduced compared to Pb/Si interfaces. The electron-electron lifetime broadening is shown to follow to a good approximation a quadratic energy dependence $\Gamma_{e-e} = \alpha(E - E_F)^2$ with $\alpha = 0.023 \text{ eV}^{-1}$. However small deviations of the quadratic energy dependence are observed and may be caused by a deviation of the screening behavior of the Pb electrons compared to that of a homogeneous electron gas [79].

CHAPTER 5

Apparent Barrier Height on Noble Metal Surfaces

Abstract

The apparent height of the tunneling barrier in scanning tunneling microscopy measured on Au(111), Ag(111), and Cu(111) surfaces is found to vary significantly with the bias voltage. In particular, the apparent barrier height ϕ_a is asymmetric with respect to the bias polarity on all three surfaces, in contrast to simple interpretations of ϕ_a in terms of an average work function of tip and sample. Model calculations of the tunneling current, which take band structure effects into account, describe the experimental observations.

5.1 Introduction

A fundamental physical property of a metal surface is its work function ϕ , which is defined as the minimum work required to remove an electron from the metal at $T = 0$ K. Knowledge about ϕ at the atomic scale can improve the understanding of chemical surface processes like heterogeneous catalysis and adsorption [11, 12]. Scanning tunneling microscopy (STM) offers the possibility to study ϕ of conductive samples at the atomic scale [104, 105] using the exponential variation of the tunneling current I with the tip excursion z [39, 106]. From $I(z)$ data an apparent barrier height ϕ_a may be determined, which—within the WKB approximation of the tunneling current through a rectangular barrier—is related

to the sample work function ϕ_s by [6, 34]

$$\phi_a = \frac{1}{2}(\phi_s + \phi_t - |eV|), \quad (5.1)$$

where ϕ_t is the work function of the tip apex, V the applied tunneling bias voltage, and $-e$ the electron charge. Hence, the effect of the finite voltage on ϕ_a is assumed to be linear. A more realistic barrier shape, which takes into account a classical image potential, leads to minor modifications [107]. Atomistic Calculations for tunneling between an Au(100) sample and tip confirm this picture in the zero bias limit [106].

The number of publications using measurements of ϕ_a to characterize surfaces is considerable. Often ϕ_a is evaluated at elevated sample voltages with $|V| \gg 0.1$ V assuming that equation (5.1) is valid [16, 21, 22, 108–111]. On the other hand, surprisingly few reports on voltage-resolved ϕ_a measurements are available [22, 112–116]. For example, ϕ_a on the reconstructed Au(111) surface was reported to show a voltage polarity dependence, which was suggested to result from the surface dipole layer originating from the reconstruction [114]. In a subsequent study no voltage polarity dependence was found [115]. Calculations predicted a voltage polarity dependence of ϕ_a on Al(100) and excluded the possibility that the polarity induced difference may be due to the formation of an additional surface dipole layer [117]. Overall, more work appears to be required to clarify the origin of the voltage dependency of ϕ_a on metal surfaces and its interpretation.

Here, we report low-temperature STM results for voltage-resolved apparent barrier heights ϕ_a on the (111) surfaces of Au, Ag, and Cu. Probing the unoccupied states of defect-free surface areas we find similar behavior for all surfaces. ϕ_a remains rather constant for sample voltages up to $V \approx 3.5$ V. At higher voltages, ϕ_a decreases within some hundred millivolts by $\Delta\phi_a \approx 2$ eV and then undergoes oscillations due to Gundlach resonances [112]. When probing the occupied states ($V < 0$), ϕ_a decreases approximately linearly with the sample voltage as expected from Eq. (5.1). Near steps, ϕ_a no longer remains constant at $V > 0$ and becomes symmetric as a function of bias voltage. Using model calculations of the tunneling current we find that observed variations of ϕ_a may be attributed to the band structures of the investigated surfaces. The geometric asymmetry of the tip-sample junction plays a minor role.

5.2 Experiment

Measurements were performed with a home-built scanning tunneling microscope operated at 5 K in ultrahigh vacuum conditions. The tunneling voltage is applied to the sample. Au(111), Ag(111), and Cu(111) single crystal surfaces were prepared by repeated Ar⁺ bombardment and annealing cycles. W tips were first electrochemically etched and then further prepared in vacuo by repeated annealing. Au tips were cut at ambient conditions and used without further treatment. The current I versus tip excursion z was measured by opening the feedback loop at a current of 100 pA and driving the tip towards the surface by 2 Å at velocities ranging from 3 to 8 Å/s. dI/dz versus V spectroscopy was performed at constant current (closed feedback loop) with a sinusoidal voltage added to the z -piezo actuator voltage of the tip (resulting in a root-mean-square amplitude of 0.15 Å) and by measuring the current response with a lock-in amplifier. The frequency of the modulation voltage was chosen between 300 and 1000 Hz, and the velocity of the bias sweep dV/dt was low enough to maintain a constant current. ϕ_a is calculated from the measured data as

$$\phi_a = \frac{\hbar^2}{8m} \left(\frac{d \ln(I)}{dz} \right)^2, \quad (5.2)$$

where m denotes the electron mass and \hbar is the reduced Planck constant. Spectra of the differential conductance (dI/dV) were acquired at constant current using standard lock-in detection (root-mean-square modulation 2.5 mV at 10 kHz).

5.3 Modeling

The one-dimensional tunneling current is calculated in the limit $T = 0$ K as[33]

$$I(V) \propto \int_0^{eV} \rho_s(E) T(E, V, \tilde{z}) dE, \quad (5.3)$$

where $\rho_s(E)$ denotes the local density of states (LDOS) of the sample at the surface and \tilde{z} is the tip-sample distance. Since STM measures only relative tip displacements, \tilde{z} differs from the tip excursion z by a constant offset z_i .

Throughout this article the Fermi level of the sample E_F has been used as the reference level and is set to 0 eV. In using Eq. (5.3) we assume an electronically featureless tip. It should be mentioned that $\rho_s(E)$ denotes an effective local density of electronic states, which are involved in the tunneling process, and may deviate from the LDOS as obtained from band structure calculations owing to a certain selectivity of the tunneling probability in k -space [6, 118]. The transmission probability $T(E, V, \tilde{z})$ for an electron impinging on the tunneling barrier with energy E is given by [6, 34]

$$T(E, V, \tilde{z}) = \exp \left[-\frac{2}{\hbar} \int_0^{\tilde{z}} \sqrt{2m(U(s) - E)} ds \right], \quad (5.4)$$

where $U(s)$ is the barrier potential felt by the tunneling electron. The sample and tip surfaces are located at $s = 0$ and $s = \tilde{z}$ respectively. The barrier potential $U(s)$ is approximate by the electrostatic potential of a spherical metallic tip with radius R in front of a planar metal surface, $U_R(s)$. For our one-dimensional calculation we use the resulting potential barrier at the central axis of symmetry. Thus the barrier potential reads

$$U_R(s) = \phi_s + (eV + (\phi_t - \phi_s)) \cdot R \left(1 + \frac{R}{2\tilde{z}} \right) \cdot \left(\frac{1}{\tilde{z} + R - s} - \frac{1}{\tilde{z} + R + s} \right). \quad (5.5)$$

In the limit $R \rightarrow \infty$, i.e. an infinitely blunt tip, we obtain the widely used trapezoid approximation of the barrier potential:

$$U_\infty(s) = \phi_s + \frac{s}{\tilde{z}} (eV + (\phi_t - \phi_s)). \quad (5.6)$$

The choice of $U(s) = U_R(s)$ will be discussed in more detail in the Appendix. For simulating the feedback loop, \tilde{z} was adjusted at each voltage V to ensure constant current I , which in turn was numerically differentiated using $d\tilde{z} = 0.2 \text{ \AA}$ to obtain $d \ln(I)/d\tilde{z}$.

5.4 Results and Discussion

Figure 5.1 shows the main experimental finding for ϕ_a on defect-free (111) surfaces of Au, Ag, and Cu. On these surfaces, we find an asymmetry of ϕ_a with respect to zero bias. For $V < 0$, ϕ_a decreases approximately linearly while for $V > 0$, ϕ_a tends to be constant up to $V \approx 3.5$ V. Beyond this voltage, ϕ_a drops significantly within some 100 mV and oscillates for even larger V .¹ As shown by Scandella and Güntherodt [112] these oscillations are due to Gundlach resonances [119].

A possible reason for the observed asymmetry with respect to bias polarity is the asymmetric geometry of a sharp tip in front of a planar surface which affects the shape of the potential barrier. We discard this possibility because calculations (see Appendix) show that the resulting polarity dependence is opposite to the observed experimental asymmetry.

Spatially resolved measurements of ϕ_a (Fig. 5.2) show clear variations on and near monatomic surface steps. For voltages close to 0 V, ϕ_a is reduced by ≈ -0.4 eV on top of the step edge (Fig. 5.2(a)), as expected owing to a reduced barrier height, which results from the Smoluchowski effect [108, 120].² At the step, the asymmetry of the voltage dependency of ϕ_a , which is observed on terraces, vanishes. Moreover, in the vicinity of step edges, ϕ_a changes continuously (at intermediate voltages) as a function of lateral displacement (Fig. 5.2(b)). Before any further analysis of these data, it is worth noting that the reduction of ϕ_a at step edges and, in particular, its apparent lateral extension depend on the sample bias and should not be mistaken to directly reflect work function

1 Despite of these general tip-independent findings, we observed that the absolute values and the exact shape of $\phi_a(V)$ are tip dependent. (i) The absolute values of ϕ_a may vary by ≈ 1 eV. (ii) The curvature of ϕ_a for negative voltages varies. E. g., for W-tips on Ag(111) we also observed an increased curvature of ϕ_a at $V < 0$ similar to the case of an Au tip on Cu(111) shown in Fig. 5.1(c). (iii) For $0 < V \leq 3.5$ V, ϕ_a tends to be rather constant but slight increases were observed for some tips. (iv) For Ag(111) and Cu(111) the width of the transition from constant ϕ_a to the range of Gundlach-resonances varies with the tip status. In this regard Au(111) is exceptional as the transition at $V \approx 3.6$ V is rather tip-independent and narrow.

2 With different tips we observed varying values of $\Delta\phi_a$ at the step edge up to ≈ -0.8 eV.

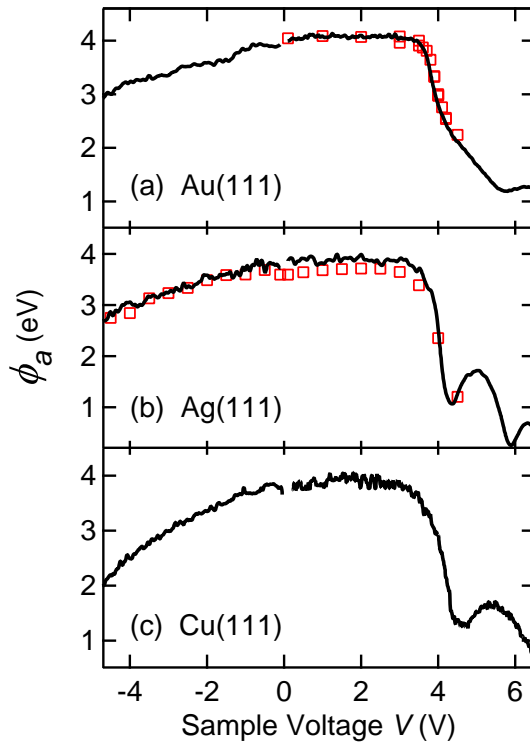


Figure 5.1: Voltage resolved apparent barrier height ϕ_a data acquired on (a) Au(111), (b) Ag(111), and (c) Cu(111) with W, W, and Au tips, respectively. Black lines denote dI/dz data acquired at constant current $I = 1$ nA, red squares show results obtained from $I(z)$ spectroscopy using Eq. (5.2). That we do find quantitatively similar results with both techniques points to the independence of ϕ_a on the tip-sample separation and also provides evidence for the correct choice of the modulation frequency during dI/dz spectroscopy.

differences.¹

We suggest that the peculiar band structures of the coinage metal (111) surfaces [87] are the origin of the observed polarity asymmetry of ϕ_a and its disappearance near steps. These band structures exhibit a projected band gap around $\bar{\Gamma}$ (wave vector parallel to the surface $k_{\parallel} = 0$) and a partially occupied surface state band within this gap (Figure 5.3). As a result, the local density of states

¹ It is worth noting that compared to Fig. 5.1(a), Fig. 5.2 shows an apparent barrier height ϕ_a which is larger by ≈ 1 eV. As mentioned before we assign this difference to the tip status.

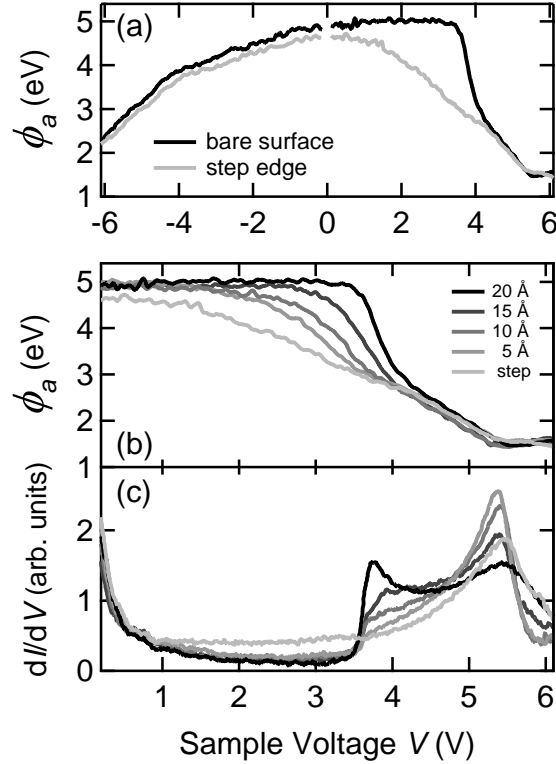


Figure 5.2: (a) Experimental results for ϕ_a on a terrace (black) and on top of a step edge (light-gray) on Au(111). (b) Detailed view of ϕ_a in the vicinity of a step edge for positive V . Light gray curves were acquired on top of the step edge; darker gray denotes increasing distances on the upper terrace from the step edge. Black lines were acquired 20 Å away from the step edge and are identical to spectra acquired on wide perfect terraces. On the lower terrace, similar results were obtained. (c) dI/dV recorded at constant $I = 5$ nA near a step edge. In (b, c) curves with the lightest gray were acquired on top of a step edge, darker gray corresponds to increasing distance on the upper terrace from the step edge as denoted by the legend in (b).

at the surface is comprised of components due to bulk states and the surface band. Their relative weights vary at step edges [121–125] and, as a consequence, ϕ_a exhibits lateral variations.

To substantiate this interpretation, additional information on the LDOS on terraces and near steps is required. We therefore recorded constant-current dI/dV spectra at these locations (Fig. 5.2(c)), which exhibit a similar lateral variation as the ϕ_a data. The spectra acquired on a bare Au(111) surface (black

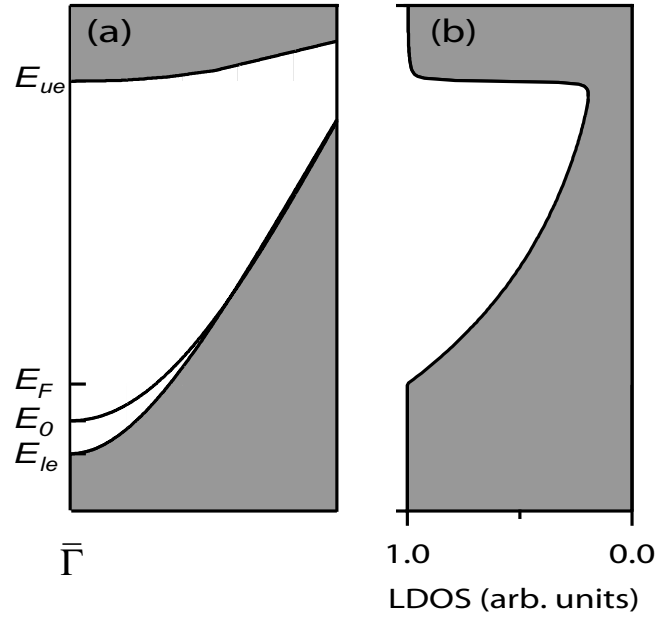


Figure 5.3: (a) Sketch of the electronic band structure at $\bar{\Gamma}$ of the (111) surfaces of Au, Ag, and Cu. The gray area denotes projected bulk bands. The black line inside the band gap (white area) shows the surface state band, with its minimum energy E_0 at $\bar{\Gamma}$. E_{le} (E_{ue}) denote the lower (upper) edge of the band gap. E_F is the Fermi energy. Table 5.1 lists the relevant energies for Au, Ag, and Cu. (b) Model LDOS $\rho_s(E)$ used for calculations.

Table 5.1: Energies of the surface state E_0 (Refs. [126, 127]) and the lower and upper projected band gap edges E_{le} and E_{ue} , respectively, at $\bar{\Gamma}$ (Ref. [87]).

| Surface | E_{le} (eV) | E_{ue} (eV) | E_0 (eV) |
|---------|---------------|---------------|------------|
| Au(111) | -1.0 | 3.6 | -0.487 |
| Ag(111) | -0.4 | 3.9 | -0.063 |
| Cu(111) | -0.89 | 4.25 | -0.435 |

line) display a steplike increase at $V \approx 3.6$ V which is generally assigned to the upper edge of the projected band gap at $\bar{\Gamma}$ [81]. Closer to the step edge (increasingly light colors in Fig. 5.2(c)) the steplike feature vanishes, the dI/dV signal below 3.6 V gradually increases, and the rapid increase above 3.6 V becomes less

pronounced. Using a normalization for constant current data [101, 128],¹ the effective tunneling density of unoccupied states is estimated from these spectra.

Figure 5.4 shows the resulting ρ_{exp} on a logarithmic scale. The color code is identical to the one used in Fig. 5.2, i.e., black on the bare surface, light gray on the step edge and intermediate colors inbetween. In spectra acquired on a

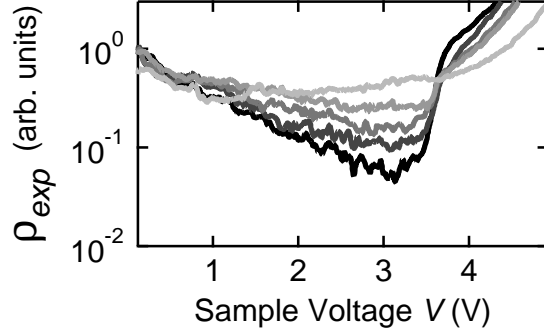


Figure 5.4: Experimental effective LDOS ρ_{exp} which is extracted from the differential conductance dI/dV shown in Fig. 5.2(c) (using the same color scheme) by normalization with $T(eV, V, \tilde{z}(V))$ as explained in the text. The black curve is acquired on the bare Au(111) surface, the lightest gray curve is taken on the step edge and intermediate colors inbetween.

terrace at varying distances from a step edge, the logarithm of ρ_{exp} decreases rather linearly with increasing V (up to $V \approx 3.2$ V). The magnitude of the slope of $\log(\rho_{exp})$ increases for increasing distance from the step edge.

The reduction of ρ_{exp} with increasing electron energy may be attributed to the projected band gap, which extends up to 3.6 eV above E_F for Au. As the tunneling probability depends on k_{\parallel} the gap is expected to diminish the contribution of bulk electronic states to the current. Similarly, the spectroscopic signal of the two-dimensional surface state decreases with increasing k_{\parallel} [101, 122, 126, 129]. Moreover, for increasing k_{\parallel} the surface band turns into a surface

¹ The differential conductance is divided by the transmission factor $T(eV, V, \tilde{z}(V))$ to obtain an experimental LDOS $\rho_{exp}(eV)$. From Fig. 5.2(b, at low positive V), we used $\phi_t = \phi_s = 5$ eV for spectra acquired off the step edge and $\phi_t = \phi_s = 4.6$ eV for the spectrum from the top of the step edge. To estimate the absolute tip-sample distance \tilde{z} , the constant-current vertical tip displacement $z(V)$ was measured concomitantly with dI/dV and \tilde{z} was calculated as $\tilde{z}(V) = z(V) + 5$ Å. Assuming a featureless LDOS of the tip, $\rho_{exp}(eV)$ should qualitatively resemble the sample LDOS $\rho_s(E)$.

resonance, which may affect its contribution to the current [130, 131].

On top of step edges, a rather constant ρ_{exp} is observed. This difference from the terrace result may have two possible reasons. As the step edge breaks the symmetry of the periodic lattice the band gap may be disturbed. Moreover, the presence of a one-dimensional state located at the step edge as found on Cu(111) [124] may modify ρ_{exp} .

For numerical calculations of ϕ_a the experimental ρ_{exp} (Fig. 5.4) was approximated by the model LDOS shown in Fig. 5.3(b). For energies between E_F and E_{ue} , $\rho_s(E)$ decreases exponentially as found in the experiments: $\rho_s(E) = \exp[-\alpha(E - E_F)]$, with α describing the exponential decrease of LDOS inside the band gap. α varies for different distances from the step. At E_{ue} , $\rho_s(E)$ increases in a $\arctan(E)$ -like manner (characteristic width 30 meV) to reach again a constant value $\rho_s(E) = 1$.

Figure 5.5(a) shows calculated constant-current ϕ_a data as obtained from Eqs. (5.3) and (5.4) using $\rho_s(E)$ as shown in (b). We find that the exponential decrease of $\rho_s(E)$ results in an increased ϕ_a in the band gap region. The stronger reduction of $\rho_s(E)$ for large α and the increased ϕ_a for $eV < E_{ue}$ is in good agreement with our experimental findings. At E_{ue} , ϕ_a decreases in a steplike manner as also found experimentally. Thus, the simple model for the LDOS is sufficient to reproduce the essential experimental effects.

According to the model calculations, ϕ_a is constant due to an exponentially-decaying effective local density of electronic states $\rho_s(E)$, which are involved in the tunneling process. $\rho_s(E)$ may be viewed as a weighting of $T(E, V, \tilde{z})$ in Eq. (5.3), which is used to calculate the tunneling current.

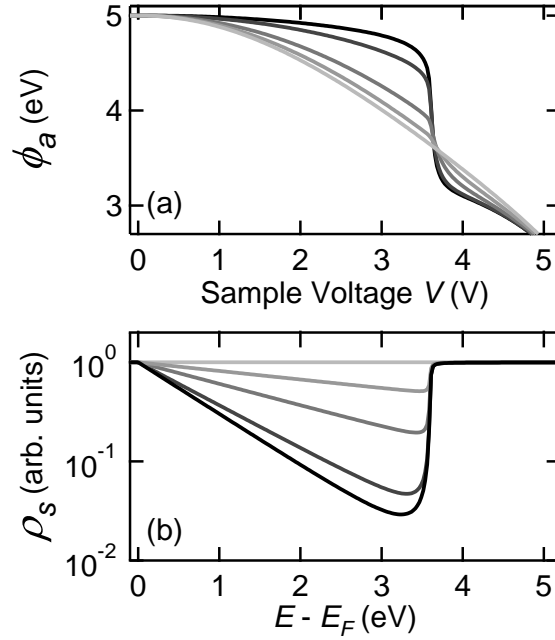


Figure 5.5: (a) Calculated constant-current ϕ_a data as obtained from Eqs. (5.3) and (5.4). The barrier potential U was approximated by U_∞ , i.e. $R = \infty$. The work functions were set to $\phi_s = \phi_t = 5$ eV as suggested by the low voltage value of ϕ_a in Fig. 5.2(b). (b) Model LDOS ρ_s used to calculate ϕ_a . The exponential decay constant was set to $\alpha = 0.0, 0.2, 0.5, 1.0$, and 1.2 eV $^{-1}$ for the curves shown in colors from light gray to black, respectively. The constant-current value for all spectra was determined at $V = 0.1$ V using $z_i = 5$ Å and $\alpha = 0$.

5.5 Conclusion

The band structure of the (111) faces of the coinage metals Au, Ag, and Cu has a significant impact on the voltage-resolved apparent barrier height ϕ_a measured by scanning tunneling microscopy. This leads to a surprising, asymmetric voltage dependence of ϕ_a with a constant- ϕ_a range for positive sample voltages below $V \approx 3.5$ V. These results have direct consequences for the interpretation of maps of the apparent barrier height. Such maps may exhibit interesting voltage dependencies, which, however, may reflect band structure variations rather than local changes of the decay of wave functions into the tunneling gap.

Acknowledgement Fruitful discussions with Thomas Frederiksen and Jörg Kröger and financial support via SFB 668, SFB 677, and the Innovationsfonds Schleswig-Holstein are gratefully acknowledged.

5.6 Annex: Influence of the Geometric Asymmetry of the Junction

The observed asymmetry of electron tunneling upon reversal of the bias polarity may in principle be caused by the asymmetric geometry of a sharp tip in front of a planar surface. Below we analyze the importance of such an effect. As to its impact on ϕ_a , we find that the geometric asymmetry cannot explain the experimental data.

First, we define the potential U in the barrier for limiting cases of the junction geometry. Two contributions to U are considered: $U = U_i + U_e$. Here U_i is the multiple image potential and U_e the potential resulting from the contact potential in case of a work function difference between tip and sample and the applied sample voltage. Figure 5.6(a) shows the multiple image potential for planar tip-sample electrodes (solid line) [132] and for a planar sample facing a hemispherical tip with radius $R = 5 \text{ \AA}$ on a planar metal surface (dashed-dotted line). The potential for the hemispherical tip in front of the planar metal surface was calculated along the high symmetry axis according to Ref. [133].

Figure 5.6(a, dotted line) shows an asymmetric reduction of U_i for the hemispherical tip, as expected. This reduction may be reasonably approximated by a straight line. In other words, the asymmetry of U_i induced by the hemispherical-tip is similar to an additional contact potential between two planar electrodes, which effectively lowers ϕ_t . Below, its effect may therefore be estimated by using different work function of tip and sample.

Figures 5.6(b) and (c) display the electrostatic potentials for different electrode geometries and bias polarities. Compared to the case of planar tip and sample electrodes (solid lines) the higher electric field causes a more rapid variation of U_e near the hemispherical tip. Hemispherical and spherical tip electrodes yield similar shapes of U_e , although the asymmetry is more pronounced for the spherical tip. A spherical tip may therefore be used to estimate an upper limit

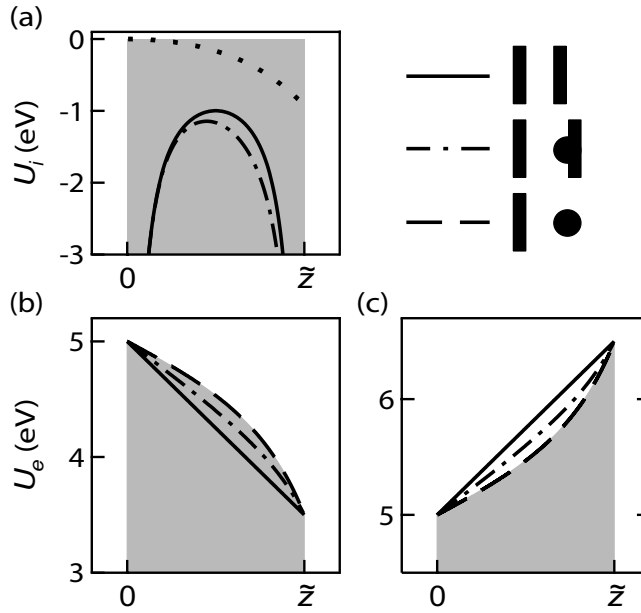


Figure 5.6: (a) Multiple image potential U_i for planar tip-sample electrodes (solid line) and a planar sample facing a tip made up of a hemisphere on a planar electrode (dashed-dotted line). The potential difference is shown by a dotted line. (b) Electrostatic potentials U_e for a planar metal electrode facing a second planar electrode (solid line), a hemisphere on a planar electrode (dashed-dotted line), or a sphere (dashed line). A negative voltage $V = -1.5$ V is applied to the left electrode. (c) Same as (b) but with $V = +1.5$ V. Further parameters: Electrode distance $\tilde{z} = 10$ Å, electrode work function $\phi = 5$ eV, hemisphere radius $R = 5$ Å.

of the impact of geometry.

Figure 5.7 summarizes the results of our numerical calculations of ϕ_a . For planar electrodes with identical work functions (Fig. 5.7(a), solid line) ϕ_a is symmetric about $V = 0$ V and decreases approximately linearly with V according to Eq. (5.1). The curvature of ϕ_a exhibits an inflection point at $V = \pm 5$ V, where $eV = \phi_s$ and the field emission regime is approached. For a spherical tip (dashed line), an asymmetry occurs. The asymmetry can be understood from Figs. 5.6(b) and (c). For all $V < 0$, the average tunneling barrier (i. e. the average value of the gray shaded area below the dashed line) is larger than the average of the trapezoidal barrier (i.e. the area below the solid line). Thus, ϕ_a decreases less as a function of voltage for a spherical tip. For $V > 0$ the effect is reversed. Electrons emitted from the Fermi level of a hemispherical tip towards

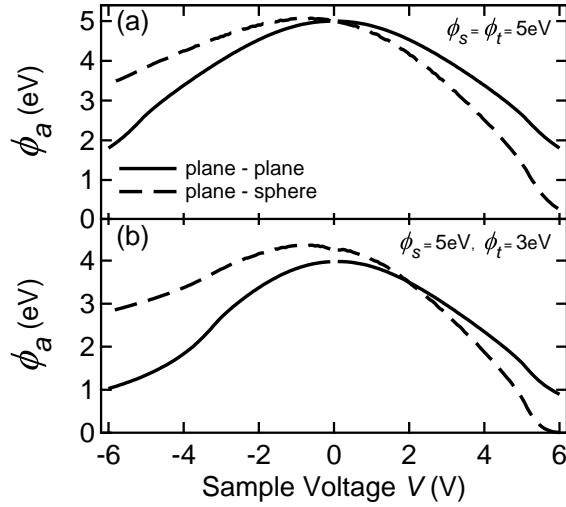


Figure 5.7: Constant-current ϕ_a data calculated from Eqs. (5.3) and (5.4) for planar electrodes (solid line) and a sphere with $R = 5 \text{ \AA}$ facing a plane (dashed line). (a) $\phi_s = \phi_t = 5 \text{ eV}$. (b) $\phi_s = 5 \text{ eV}$, $\phi_t = 3 \text{ eV}$. Further parameters: $\rho_s(E)$ set constant; $z_i = 5 \text{ \AA}$ and $V_i = \pm 0.1 \text{ V}$.

the sample, 'feel' an average barrier height that is smaller than for a planar electrode. Similar results are obtained when different electrode work functions are considered to mimic the effect of multiple image charges (Fig. 5.7(b)).

In summary, the geometric asymmetry of the STM junction may lead to a polarity dependence of ϕ_a , which is, however, opposite to the experimentally observed trends. If present in the experiment, it appears to be hidden by the band structure effects presented above.

CHAPTER 6

Contrast Inversion of the Apparent Barrier Height of Pb Thin Films

Abstract

Scanning tunneling microscopy measurements of the apparent height of the tunneling barrier are analyzed for Pb islands on Ag(111). The apparent barrier height (ABH) significantly varies with the bias voltage. This bias dependence leads to drastic changes and even inversion of contrast in spatial maps of the ABH. Using model calculations, these variations are interpreted in terms of the strongly modulated local density of states of thin Pb films, which is caused by quantum well states.

6.1 Introduction

The work function ϕ is an important property of surfaces, which influences catalytic reactivity and charge injection at interfaces. It controls the availability of charge carriers in front of a surface. Modifying ϕ has been achieved by deposition of metals and molecules [3, 4]. In particular, for Pb thin films on Si(111) the existence of a quantum-size-effect [2] induces a bilayer modulation of ϕ and of the chemical reactivity [15, 16, 19, 22, 134]. For investigating ϕ at the atomic scale, scanning tunneling microscopy (STM) has become a widely used technique. From the variation of the tunneling current I with the tip excursion z , an apparent barrier height ϕ_a may be extracted [5], which —within the WKB approximation

of the tunneling current between free-electron metals separated by a rectangular barrier—is related to the sample work function ϕ_s by [6]: $\phi_a = (\phi_s + \phi_t - |eV|)/2$. Here, ϕ_t is the local work function of the tip apex, V the applied tunneling bias voltage, and $-e$ the electron charge.

In this chapter, we report voltage resolved STM measurements of ϕ_a on Pb thin films supported on Ag(111). Strong modulations of the local density of states (LDOS), which are due to quantum well states (QWS's) in the Pb adlayers, result in a profoundly non-linear behavior of ϕ_a as a function of the bias voltage V . ϕ_a is found to be very sensitive to the shape of the LDOS. In spatial maps of ϕ_a , small voltage changes $\Delta V \approx 50$ mV can result in contrast reversal. Numerical calculations of the tunneling current using a one-dimensional WKB approximation and including the LDOS modulations induced by the QWS's, describe the experimental observations.

6.2 Experiment

Measurements were performed with a home-built scanning tunneling microscope operated at 5 K in ultrahigh vacuum conditions. The tunneling voltage is applied to the sample. Ag(111) single crystal surfaces were prepared by repeated Ar⁺ sputter/anneal cycles. Pb islands of several monolayer (ML) thickness were obtained by room-temperature deposition from a tungsten crucible with a deposition rate of 1ML/min. Pb grows on Ag(111) in the Stranski-Krastanov mode [44, 45] with an initial 1 ML thick wetting layer (WL). Film thicknesses are numbered in ML beyond the WL. Electrochemically etched W tips were prepared by annealing cycles and indenting into Pb islands, thereby covering the tip apex with Pb. The current I versus tip excursion z was measured by opening the feedback loop at 100 pA and driving the tip towards the surface by 2 Å. Constant-current dI/dz versus V spectroscopy was performed with a closed feedback loop. A small sinusoidal modulation of the tip-sample separation (amplitude 0.15 Å_{rms}) was used and the current response was measured with a lock-in amplifier. ϕ_a was calculated from the measured data as

$$\phi_a = \frac{\hbar^2}{8m} \left(\frac{d \ln(I)}{dz} \right)^2, \quad (6.1)$$

where \hbar is the reduced Planck constant and m the electron mass. Spectra of the differential conductance (dI/dV) were acquired by using standard lock-in detection (voltage modulation amplitude 2.5 mV_{rms}, frequency 10 kHz).

6.3 Modeling

Numerically, the tunneling current as a function of sample voltage V and tip-sample distance \tilde{z} was calculated as[33]

$$I(V) \propto \int_{E_F}^{E_F+eV} \rho_s(E) T(E, V, \tilde{z}) dE, \quad (6.2)$$

where ρ_s denotes the LDOS of the sample at the surface and E_F is the Fermi level of the sample. Since STM measures only relative tip displacements, \tilde{z} differs from the tip excursion z by a constant initial offset z_i . It should be mentioned that $\rho_s(E)$ denotes an effective local density of electronic states, which are involved in the tunneling process, and may deviate from the LDOS as obtained from band structure calculations owing to a certain selectivity in k -space. The transmission probability $T(E, V, \tilde{z})$ for an electron impinging on the tunneling barrier with energy E is given by

$$T(E, V, \tilde{z}) = \exp \left[-\tilde{z} \sqrt{\frac{4m}{\hbar^2} (\phi_s + \phi_t + eV - 2E)} \right]. \quad (6.3)$$

For simulating the feedback loop, \tilde{z} was adjusted for each voltage V to ensure constant current I , which in turn was numerically differentiated using $d\tilde{z} = 0.2 \text{ \AA}$ to obtain $d \ln(I)/d\tilde{z}$. In using (6.2) we assume an electronically featureless tip, which is supported by the experimentally observed clearly dominating impact of the sample LDOS.

6.4 Results and Discussion

Figures 6.1(a,b) show experimental data of (a) voltage resolved ϕ_a and (b) constant-current dI/dV measured on the WL (red) and on a Pb island (see

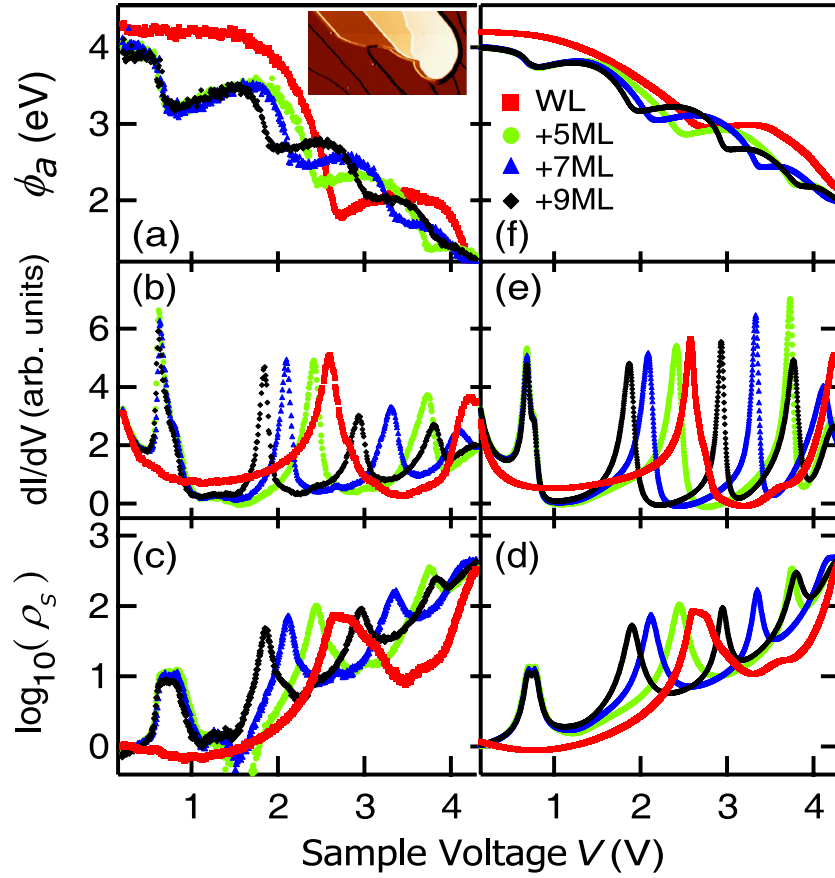


Figure 6.1: Experimental (left) and numerical results (right) for the voltage resolved apparent barrier height ϕ_a : (a) and (f), and for constant-current dI/dV : (b) and (e), respectively. Experimental data has been acquired on the wetting layer (WL) and on the island shown in the inset to (a) (image size $330 \times 175 \text{ nm}^2$). See legend in (f) for color code. (c) experimentally derived LDOS ρ_s as explained in the text. (d) model LDOS used for the numerical calculation. The model LDOS has been constructed from a set of lorentzians approximating the experimental LDOS shown in (c). The constant current setpoint was determined at: $z_i = 5 \text{ \AA}$, $V = 0.1 \text{ V}$, WL: $\phi_s = \phi_t = 4.2 \text{ eV}$, Pb island: $\phi_s = \phi_t = 4.0 \text{ eV}$.

inset to Fig. 6.1(a)) consisting of 5, 7, and 9 ML of Pb beyond the WL (green, blue, and black data points, respectively). The same color scheme is used throughout Fig. 6.1). We find a nonlinear behavior of ϕ_a which is apparently linked to variations of the dI/dV signal. ϕ_a tends to decrease for increasing dI/dV , while ϕ_a stays constant or even increases for decreasing dI/dV . Before analyzing the

data any further, it is worth noting that relative differences of ϕ_a on the different island heights and on the WL are voltage dependent and should not be mistaken to directly reflect work function differences. For example, at $V \approx 2$ V, ϕ_a is largest for the WL and smallest for the 9 ML film (Fig. 6.1(a)). At $V \approx 2.7$ V, this sequence is reversed. We suggest that the peculiar LDOS of the quantum well system Pb/Ag(111) is at the origin of the observed voltage dependence of ϕ_a . To substantiate this interpretation we normalize the constant-current dI/dV data to estimate the density of unoccupied states from these spectra [38, 101].¹ Figs. 6.1(c,d) show the experimentally derived LDOS ρ_s and a model LDOS chosen such as to mimic the experimental data. Using this model LDOS, dI/dV and ϕ_a were calculated (Figures 6.1(e,f)). As in the experiment, an increasing ρ_s results in an increasing dI/dV and decreasing ϕ_a . In other words, the simple model of the tunneling current is able to reproduce the essential experimental findings. Hence, the nonlinear behavior of ϕ_a may be attributed to the weighting of $T(E, V, \tilde{z})$ by $\rho_s(E)$ in Eq. 6.2. In addition to this effect, a wavevector-dependence of the electron decay length has been suggested to play a role [134]. As the experimental LDOS ρ_s in our model already includes tunneling matrix element effects it is difficult to separate these two contributions in the present study.

Below we analyze the impact of the voltage dependence of ϕ_a on spatially resolved maps of ϕ_a . Figure 6.2(a) shows ϕ_a data from a Pb island with thicknesses varying from 16 to 26 ML. Different voltages were used as indicated at the images. At $V = 5$ mV, ϕ_a is almost unaffected by finite voltage effects. Contrasts in this map, therefore, reflect variations of ϕ_a due to the different film thicknesses. Clear even-odd oscillations are observed as a function of the number of layers in the film as expected. The dI/dV spectra in Fig. 6.2(b) reveal the energies of the QWS of a few characteristic terraces labeled 1–6 in Fig. 6.2(a). Comparison of the values of ϕ_a and the position of the highest-occupied QWS shows that

¹ The differential conductance is divided by the transmission factor $T(eV, V, \tilde{z}(V))$ to obtain $\rho_s(eV)$. From Fig. 6.1(a, at low V), we used $\phi_t = \phi_s = 4.2$ eV for the spectrum acquired on the WL and $\phi_t = \phi_s = 4.0$ eV for spectra on the Pb island. \tilde{z} is calculated as $\tilde{z}(V) = z(V) + 5$ Å where $z(V)$ is the constant-current vertical tip displacement measured concomitantly with dI/dV . Assuming a featureless LDOS of the tip, $\rho_s(E)$ should qualitatively resemble the sample LDOS.

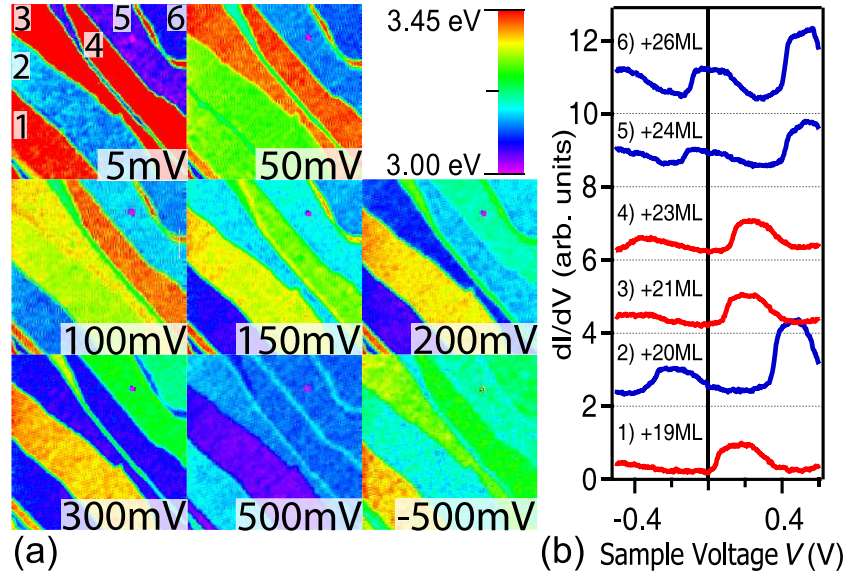


Figure 6.2: (a) Maps of the apparent barrier height ϕ_a acquired by means of $I(z)$ measurements on a Pb island (thickness WL+16 to +26 ML) at different voltages as indicated at the images (for magnitude of ϕ_a see colorscale). (b) Constant-height dI/dV spectra acquired at the terraces indicated by numbers in the ϕ_a map at 5 mV. Spectra are offset by even integers for clarity.

ϕ_a assumes low values when this state is close to the Fermi level. These observations appear to qualitatively agree with previous results reported by Qi *et al.* for Pb/Si(111) from measurements at $V = -2$ V [16]. A striking difference, however, are the drastic changes of the ϕ_a maps with the applied bias voltage. For instance, the terraces labeled 2, 5, and 6 exhibit lower ϕ_a than terraces 1, 3, and 4 at $V = 5$ mV. At $V = 300$ mV, this sequence is inverted.

From the dI/dV spectra shown in Fig. 6.2(b), the voltage dependent change of ϕ_a at the different layer thicknesses can be understood along the same line as the spectroscopic results in Fig. 6.1. For positive voltages, we find an increasing dI/dV signal to result in a decreasing ϕ_a and vice versa. For elevated negative voltages the effect is different as will be discussed below.

At $V < 0$ V the tunneling current is dominated by electrons from close to E_F . Given a peak in the occupied ρ_s close to E_F , electrons from this peak region will predominantly contribute to the current. The value of dI/dz will, therefore, reflect the apparent barrier characteristic of these electrons. ϕ_a will be small if

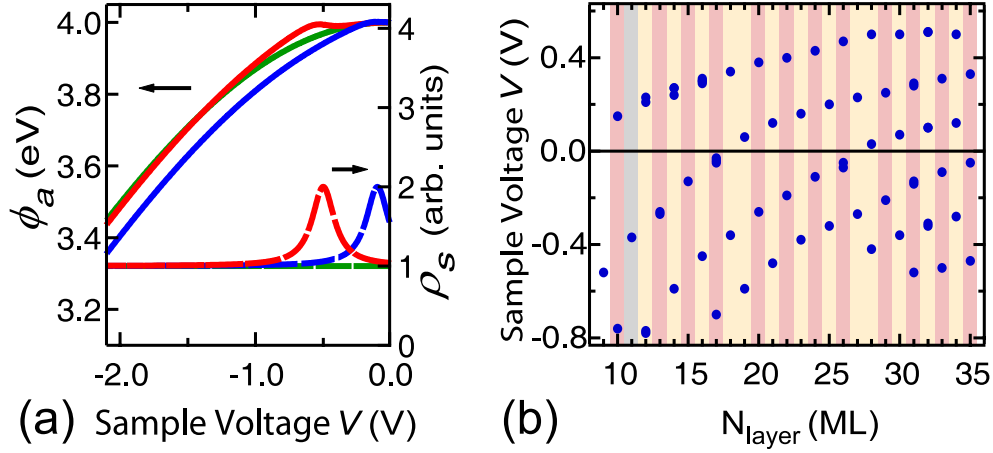


Figure 6.3: (a) Impact of gaussian peaks in the LDOS ρ_s (dashed lines) on ϕ_a (solid lines) calculated for $V < 0$ and $\phi_s = \phi_t = 4$ eV. The result for constant ρ_s is shown in green for comparison. Peak positions: -0.1 V and -0.5 V, full width at half maximum = 0.2 V. Setpoint parameters: $z_i = 5$ Å, $V = 0.1$ V, and $\rho_s(E) = 1$. (b) Layer-resolved QWS energies (blue dots) extracted from experimental dI/dV spectra. Background colors reflect low voltage ϕ_a results: Yellow corresponds to $\phi_a(N) > \phi_a(N-1)$ and red to $\phi_a(N) < \phi_a(N-1)$. As for $\phi_a(11)$ no discernible difference to $\phi_a(10)$ is found, gray background was used.

this LDOS peak is close to E_F and will increase as the peak moves away from E_F .

Numerical results (Fig. 6.3(a)) confirm the qualitative picture. ϕ_a was calculated for negative voltages assuming a LDOS which is constant except for a Gaussian peak close to (blue) or farther away (red) from E_F . The result for constant ρ_s (green) is shown for comparison. The height of the peak was chosen to be comparable to the observed peaks in Fig. 6.2(b). We find that a pronounced peak close to E_F reduces ϕ_a (blue, solid line) compared to a peak farther away from E_F (red, solid line). As an important consequence, ϕ_a measured at elevated negative voltages may oscillate as a function of layer thickness because the energy of the highest occupied QWS oscillates. No oscillation of the work function ϕ is required.¹ An oscillation of ϕ has previously been inferred in Ref. [16] from mea-

¹ We note that a LDOS peak close to E_F results in an increased topographic height, too, as first pointed out by Altfeder *et al.* [135].

measurements of ϕ_a at $V = -2$ V. The above results suggest that this interpretation is not fully conclusive.

Finally, Figure 6.3(b) shows layer-resolved QWS energies (blue dots) of Pb thin films on Ag(111) determined from series of dI/dV spectra (not shown). We use background colors to indicate the apparent barrier heights (red/yellow indicating low/high ϕ_a) measured at low bias, $|V| \leq 10$ mV. Under this condition, changes of ϕ_a are expected to reflect changes of the work function. For the investigated thicknesses $N = 11 \dots 35$ layers of Pb on Ag(111), we re-establish the finding of Qi *et al.* [16]. A highest occupied QWS close to E_F results in a low ϕ_a (red background). As reported in Ref. [16] a beating pattern at $N = 18$ ML and $N = 27$ ML is also observed.

6.5 Conclusion

In summary, the dependence of the apparent barrier height ϕ_a on the bias voltage can be profoundly nonlinear. The contrast of ϕ_a maps taken on multilayer Pb islands can be reversed for different tunneling bias voltage V . Model calculations show that this result is not limited to Pb/Ag(111). In general, ϕ_a measurements on systems exhibiting strong variations of the local density of states are prone to nonlinearity effects of the finite bias. At small bias voltages, the experimental data confirms the even-odd oscillation of ϕ_a with the number of Pb layers.

Acknowledgement Financial support by the Deutsche Forschungsgemeinschaft (SFB 668, SFB 677) and by the Innovationsfonds Schleswig-Holstein is gratefully acknowledged.

CHAPTER 7

Conductance of Atom-Sized Pb Contacts

Abstract

The contact formation of a metallic tip approaching Pb thin films supported on Ag(111) substrates is investigated with a cryogenic scanning tunneling microscope. While contacts to thicker Pb films are formed rather abruptly, the transition between tunneling and contact is gradual for the first Pb monolayer on Ag(111). This behavior may be understood in terms of different vertical bonding-strengths due to a charge-transfer induced surface dipole. Owing to the gradual evolution of tip-surface contacts on the first Pb(111) ML imaging can be performed at contact. Furthermore, we show that for atomic-sized Pb contacts, the interpretation of peaks in conventional conductance histograms in terms of single-atom point-contact conductances yields an overestimation of contact conductances.

7.1 Introduction

The electron transport properties and mechanical characteristics of atomic-sized metallic contacts are of fundamental interest in view of future nanoscale device technologies. Proximity probes like the scanning tunneling microscope (STM), metal break junctions, and related techniques, together with computational methods for simulating tip-sample interactions with atomic detail, have made it possible to address this issue [7]. Tip-surface point contacts are known

to exhibit a jump of the conductance [8, 106, 136, 137]. When stretched to the point of breaking, their conductance decreases in discrete steps. The shape of this staircase is material dependent and is related to electronic and mechanical properties of the contact region [138]. The conduction in such systems is usually discussed in terms of the Landauer formula [139, 140]. Using a suitable set of quantum states, so-called eigenchannels, the low-temperature linear conductance of a point contact can then be written as $G = G_0 \sum_i T_i$, where $T_i \in [0,1]$ are transmission probabilities of the eigenchannels and $G_0 = 2e^2/h = 77.5 \mu\text{S}$ is the quantum of conductance. Here, h is the Planck constant and $-e$ the electron charge. Much current research aims at measuring, understanding and controlling these transmission probabilities and their variation with geometric structure, electrode material, electrode magnetization, mechanical strain etc. Taking advantage of the imaging capability of the STM recent experiments on individual adsorbed atom (adatom) [8, 141–143] and on single molecule [9, 144, 145] contacts showed that these contacts can reproducibly be made without structural changes of tip or sample.

Here we report a study into the conductance G of a Pb tunnel tip contacting Pb(111) thin films supported on Ag(111) substrates.¹ The contacts are found to exhibit a reproducible variation from tunneling to the contact regime with purely elastic deformations of tip and sample. So far, such behavior has not been observed on close packed fcc metal surfaces at low V , where contacts are known to quite reproducibly result in material transfer from tip to sample [8]. The transition between tunneling and contact is found to be more gradual for the first Pb(111) monolayer (ML), while contact to thicker films is more abrupt. This behavior may be understood in terms of different vertical bonding-strengths due to a charge-transfer induced surface dipole, which increases the stiffness of the Pb-Ag bond compared to a Pb-Pb bond. For the first Pb(111) ML it is shown that owing to the gradual character of the tip-surface contacts contact imaging can be performed.

¹ We used Pb-covered W-tips as described in the *Experiment* section. Throughout this article we refer to these tips simply as Pb tips.

7.2 Experiment

Measurements were performed with a home-built scanning tunneling microscope operated at 5 K in ultrahigh vacuum conditions. The tunneling voltage V is applied to the sample. Ag(111) single crystal surfaces were prepared by repeated Ar⁺ sputter/anneal cycles. Pb films were obtained by room-temperature deposition from a tungsten crucible with a deposition rate of 1 ML/min. Electrochemically etched W tips were prepared by annealing cycles and indenting into Pb islands, thereby covering the tip apex with Pb. Throughout the article we refer to these tips simply as Pb tips. The current I versus tip excursion z was measured by opening the feedback loop and driving the tip toward the surface by $\approx 2 \text{ \AA}$ at velocities ranging from 0.5 to 2 $\text{\AA}/\text{s}$. The experimental setup of Limot *et al.* was employed to avoid a significant voltage drop at the current preamplifier [94].

7.3 Results and Discussion

Pb grows on Ag(111) in the Stranski-Krastanov mode [44, 45] with an initial 1 ML thick wetting layer (WL) which exhibits a hexagonal moiré-type modulation with a $(\sqrt{19} \times \sqrt{19}) \text{ R } 23.4^\circ$ supercell [56]. The in-plane lattice constant of the Pb WL corresponds within 99% to the (111) in-plane lattice constant of bulk Pb, 3.5 \AA . At higher coverage, flat-top islands of distinct heights are formed. The in-plane lattice constant on the Pb islands corresponds to that of bulk Pb. We number the film thicknesses including the WL in MLs.

Figure 7.1 shows an atomically resolved image of the moiré pattern observed on a 6 ML Pb island. The color scale corresponds to a height range of 0.23 \AA . On the Pb islands, the moiré pattern can be observed for film thicknesses as large as ≈ 35 ML [146]. Altfeder *et al.* reported that the moiré pattern in multilayers is caused by lateral adiabatic changes of the electrons scattering-phase shift located at the adlayer/substrate interface rather than geometric modulation of the films [70].

For typical tunneling conductances G in the range of $\approx 10^{-5} - 10^{-2} G_0$ ($V = 100 \text{ mV}$) the apparent height of the moiré superstructure is $\approx 0.1 \text{ \AA}$ on the

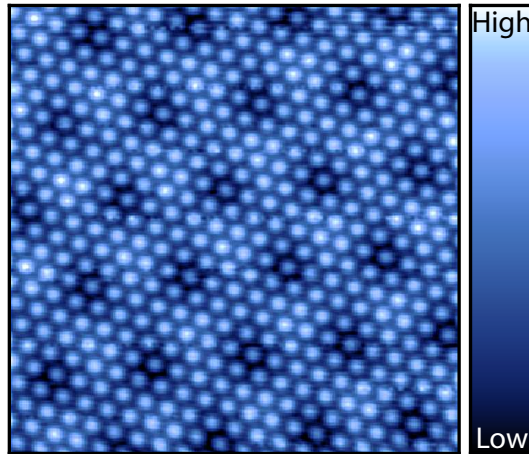


Figure 7.1: Atomically resolved topograph ($6.8 \times 6.8 \text{ nm}^2$) of a 6 ML Pb island, clearly exhibiting a moiré-type superstructure. The color scale corresponds to a height range of 0.23 \AA ($V = 100 \text{ mV}$, $I = 710 \text{ nA}$, $G = 0.09 G_0$).

WL and somewhat smaller on Pb islands. The increased apparent height of the moiré pattern as shown in Fig. 7.1 for a conductance of $G = 0.09 G_0$ indicates deviations of G as a function of tip excursion z from purely exponential behavior at conductances larger than $10^{-2} G_0$ and will be discussed below.

For contact measurements on pristine noble metal (111) surfaces using low voltages, $G(z)$ traces exhibit a strictly exponential behavior in the tunneling regime up to the point where a sharp jump to contact (JTC), random in nature, occurs [106]. Usually, the tip-apex atom is transferred to the surface during this process. In the contact range, $G(z)$ saturates and stays rather constant. In contrast, the conductance over single Ag (Cu) adatoms on Ag(111) (Cu(111)) exhibits a smooth and reproducible elastic transition from tunneling to contact regime [8].

For the Pb tip-surface contacts studied here, more than 200 contacts can be made with well formed Pb tips without material being transferred between tip and sample.¹ While contacts acquired in a sequence at the same location are highly reproducible, contacts on different positions of the moiré pattern result

¹ Unless stated explicitly, all presented contact traces were not accompanied by material-transfer between tip and sample, which was checked by repeated topographical imaging of the surface.

in different shapes of the contact traces. Ranging from very smooth behavior, where no sign of a JTC is observed, to JTC characterized contacts as also found on noble metal (111) surfaces [8, 136, 147]. In addition to the variations with lateral position, there are distinct differences of the contact traces acquired on the WL compared with contacts made on thicker Pb films.

7.3.1 Thickness Dependence of Pb Contacts

Figures 7.2(a),(b) show normalized probability distributions of the variability of G vs the tunneling gap variation Δz acquired on (a) 6 ML Pb and (b) the WL. A total of 80 conductance traces acquired alternately on the two film thicknesses is shown. After each individual contact trace, the tip has been laterally moved onto the other film thickness where the next contact trace was acquired. The traces were taken throughout the moiré supercell, without noticeable irreversible change of the tip configuration. It is found that the transition region exhibits a more pronounced step-like behavior with a larger variety of the conductance traces on the 6 ML Pb film (Fig. 7.2(a)) as compared with the WL (Fig. 7.2(b)). Similar results were found for the comparison of contact traces on the WL and 3ML Pb. Here we focus on thin Pb films with thicknesses ≤ 6 ML and voltages $V \leq 200$ mV, such as to rule out any impact of quantum well states on the measured conductances [73, 148]. For the WL the transition from tunneling to contact is very smooth and also more homogeneous throughout the moiré supercell as can be inferred from the reduced variation of contact traces in Fig. 7.2(b). To further illustrate the difference between the contact spectra acquired on the different film thicknesses, $G(z)$ histograms of the contact traces are shown in Figure 7.2(c). The dark blue line denotes the $G(z)$ histogram of the WL. The smooth $G(z)$ traces result in a histogram with a very flat characteristic, where no clear discrimination between tunneling and contact regime is obvious. In contrast, the $G(z)$ histogram of the 6 ML Pb film (light blue area) exhibits a clear step-like onset at the transition to the contact regime. The analysis of Pb conductance histograms on film thicknesses beyond 1 ML will be discussed below.

We assign the differences of the conductance traces to the different atomic species in the second layer and suggest that the peculiar vertical bonding strength

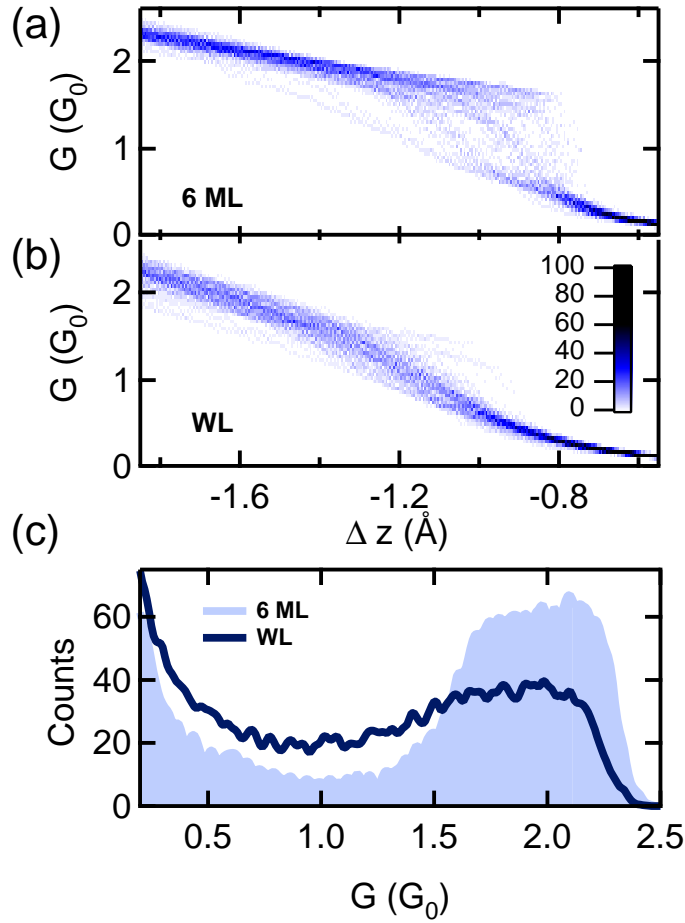


Figure 7.2: $G(z)$ traces of atomic-sized contacts on (a) 6 ML Pb and (b) the WL. To quantify the scatter of the traces, probability distributions were calculated at each value of Δz and used to color the data points (color scale as inset to b). Set point: $I = 250$ nA $V = 0.1$ V. 80 conductance traces were acquired alternately on the two terraces, throughout the moiré supercell. (c) Histogram of the conductance traces $G(z)$ from (a) (light blue) and (b) (dark blue).

of the Pb(111) surface layer atoms is the origin of the observed differences of contact traces. While the Pb surface atoms of the WL are vertically bonded to Ag substrate atoms, the surface layer atoms of films with $ML > 1$ are vertically bonded to Pb atoms. By means of electrochemical underpotential deposition experiments it has been shown that the Pb-Ag bonding energy is 0.3 eV larger than that of a corresponding Pb-Pb bond [44]. This increase in binding energy

has been shown to be related to charge transfer effects between the WL and the Ag(111) substrate [149]. Assuming that the vertical bonding strength of such a Pb-Pb bond must be between the limiting values of the bonding strength of a single Pb₂ dimer and that of a nearest neighbor bond in bulk Pb, which corresponds to 0.84 eV and 0.34 eV respectively,[150, 151] it may be inferred that the Pb-Ag bonding strength is larger by $\approx 35 - 90\%$. Therefore, it is expected that the stiffness of the vertical bond of the WL to the Ag(111) surface atoms is enhanced.

A possibly related result has been observed for single Ag (Cu) adatoms on Ag(111) (Cu(111)), where the origin of the observed smooth contact traces is a redistribution of surface charge due to the Smoluchowski effect that creates a surface dipole which enhances the bonding of the adatom [8]. Hence, the atomic positions are only slightly relaxed during the transition from the tunneling regime to point contact, which is in sharp contrast to the situation on the flat noble metal (111) surfaces, where the tip apex was routinely fractured and a sudden JTC was observed. The reason being the larger stiffness of the adatom bond to the surface. It is found that the surface dipole roughly doubles the elastic constants as compared to the value found on flat surfaces [152].

7.3.2 Imaging at Contact

Taking advantage of the very smooth characteristics of the contact traces on the WL, it is possible to perform contact imaging. Figure 7.3 displays the evolution of constant current STM topographs spanning the range from (a) $0.16 G_0$ to (f) $1.26 G_0$. At conductances of $\approx 0.25 G_0$ the corrugation of the Pb atoms is reversed. Comparing Fig. 7.3 (a) and (b) ($0.43 G_0$) the Pb atoms appear as protrusions in (a), while they appear as depressions in (b). Further increase of the current results in a triangular-shape-like appearance of the WL hollow positions and increased apparent heights. A similar effect of corrugation reversal has been observed for manipulated-atom images [153, 154]. Those images were obtained by rastering a Co adatom over a Cu(111) surface, using the tip-induced local potential to trap the Co atom under the rastering probe tip. It was concluded that, due to adhesion forces the Co atom did not precisely follow the tip, but hopped to the fcc or hcp binding sites nearest the moving tip. Since there is

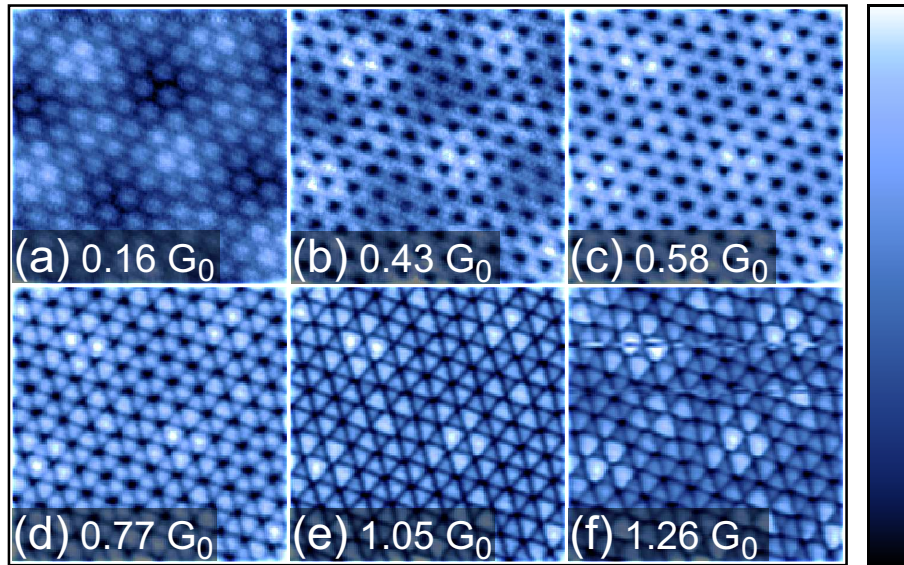


Figure 7.3: WL contact images with Pb tip ($V = 100$ mV): (a) $0.16 G_0$, (b) $0.43 G_0$, (c) $0.58 G_0$, (d) $0.77 G_0$, (e) $1.05 G_0$, (f) $1.26 G_0$. Color scale corresponds to 0.17 \AA for (a), (b), and 0.28 \AA for (c)-(f).

no adatom involved in the acquisition of the contact images presented here, we assign the observed corrugation to the lateral elasticity of the apex atom of the tip, which, while rastering the surface, prefers to reside on hollow position of the Pb lattice. Hence, when scanning on top of a Pb atom, the apex atom is laterally attracted and deflected towards the nearest hollow position. This causes the STM electronics to approach the tip toward the surface in order to maintain a constant current. Therefore the on top position appears as depressions. On this grounds the increased resolution with increased conductance may be understood in terms of enhanced attractive (repulsive) forces of the hollow (on top) position with increased proximity of tip-apex atom and sample, such that the deflection of the apex atom as a function of lateral position becomes more inhomogeneous. As an additional feature, the moiré pattern is observed in contact images, too. The apparent height of the hollow positions is modulated according to the $(\sqrt{19} \times \sqrt{19}) R 23.4^\circ$ supercell. However, from the present data it appears difficult to distinguish whether this contrast reflects just real height differences due to the corrugation of the WL, or is an indicator of preferred binding sites as it was suggested for Co on Cu(111) [153]. Note, in contrast to Co on Cu(111) we do

not observe a three-fold symmetry, which can be understood in terms of the moiré supercell where the Pb atoms are not in registry with the Ag(111) lattice.

7.3.3 Analysis of Pb Conductance Histograms

For a quantitative comparison of atomic-sized contacts made of different materials, the conductance traces are often represented by a single value, the contact conductance G_c . G_c may be analyzed using conductance histograms of large numbers of $G(z)$ traces [7]. For noble metals the conductance histogram exhibits a clear peak at G_c owing to the flat-top steplike behavior of $G(z)$ in contact. However, for materials where the conductance exhibits a finite slope in the contact regime, the determination of G_c using conductance histograms is more difficult. Figure 7.4 shows data of a representative series of 223 conductance traces bridging the transition between tunneling and contact regime. These data were acquired consecutively on a 3 ML Pb film with the same tip. Contact traces acquired on 6 ML Pb, using the same voltage, exhibit similar behavior (see Fig. 7.2(a)). Contacts were made at different sites of the moiré pattern. The area shaded light-blue in Fig. 7.4(a) indicates the variability of the conductance measurements and encloses all 223 $G(z)$ contact traces. Here the conductance vs tunneling gap variation is displayed on a logarithmic scale. Four representative contact traces are highlighted, showing the variety of the elastic Pb contacts. The random character of the contact traces may be understood in the light of DFT structure simulations, where it was shown that the jump to contact on Au(111) strongly depends on whether the tip is positioned on top of a surface atom or over a hollow [155]. In the following the different regimes of the contact traces are discussed.

The exponential variation of the tunneling current is usually characterized by the apparent barrier height ϕ_a :

$$I \propto \exp(-1.025\sqrt{\phi_a} \tilde{z}) \quad (7.1)$$

where ϕ_a is in eV and \tilde{z} the tip-sample distance in Å. For the Pb-Pb tunneling junctions studied here, we find for $G < 10^{-2} G_0$ a constant ϕ_a in the range of 3.5 - 5 eV, characteristic for metal-metal tunneling junctions. Here ϕ_a depends on the

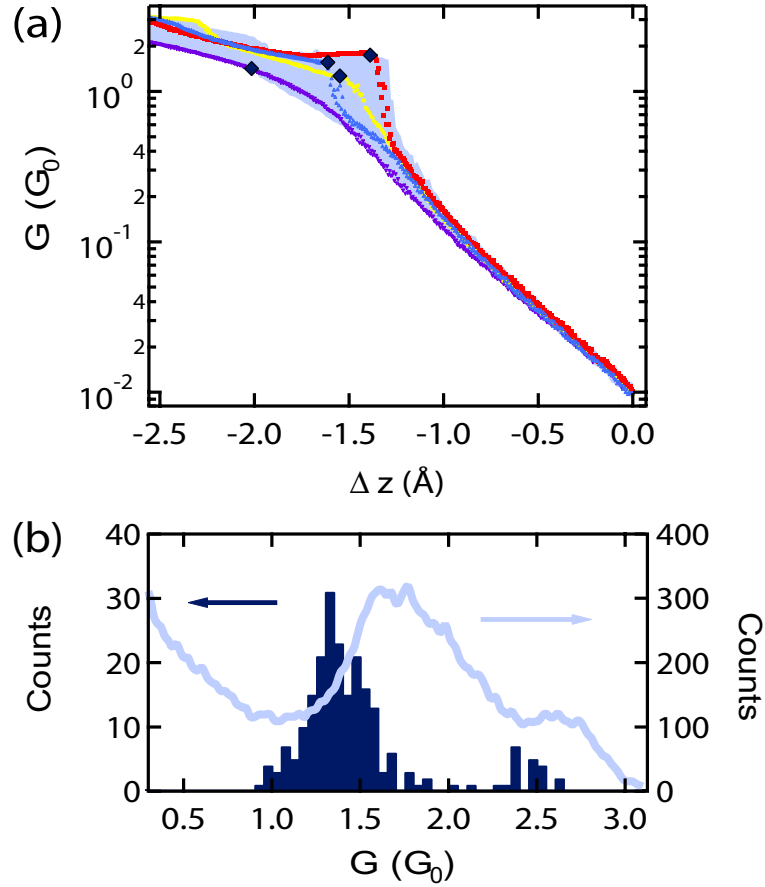


Figure 7.4: (a) The light-blue shaded area denotes the variability of 223 consecutively acquired contact traces on a 3 ML Pb island without material transfer ($V = 200$ mV). 4 representative contact curves are highlighted. Diamonds denote the deduced contact conductance G_c of the different traces. (b) Histograms of the contact conductance G_c (dark-blue) and of the conductance $G(z)$ (light-blue) of the data presented in (a).

tip, film thickness, and applied bias [17]. ϕ_a starts to increase $\approx 0.5 - 1$ Å before the contact is reached up to $\approx 7 - 8$ eV. Concomitantly, the variability of the $G(z)$ traces in the tunneling regime recorded throughout the moiré supercell increases, i.e. for increasing conductance the light blue shaded area in Fig. 7.4(a) gets wider. This marks the beginning of the transition region in $G(z)$ measurements and explains the enhanced corrugation of the moiré pattern as shown in Figure 7.1.

In the transition region $G(z)$ exhibits a rich structure (see, e.g., the dark blue trace in Fig. 7.4(a)) which makes it difficult to characterize this range by an

assignment of a single-valued slope. However, as a general result, we find that at conductances of $\approx 0.1 G_0$ the slope of the conductance traces increases and the transition region is entered. The transition region is then followed by the contact regime which exhibits an approximately constant slope (on the logarithmic scale) which is significantly smaller than the slope in the tunneling regime.

In addition to using conductance histograms for evaluating G_c , other schemes have been employed. For single-atom contacts Limot *et al.* [8] defined G_c by the intersection between the experimental curve and the linear extrapolation of $\ln(G(z))$ vs z at large tip-sample separations. For the present Pb data, the point of intersection lies in the transition range for some of the $G(z)$ traces. Néel *et al.* [9, 143, 156] used the conductance right after the JTC, which was defined as the point of intersection of linear fits to the transition and contact ranges of $\ln(G(z))$ vs z . Due to the rich structure of the transition range in the present study, we modified this latter approach and performed a local fit to the transition range close to the contact regime, where the slope approaches a constant value. The resulting G_c are highlighted by diamonds in Fig. 7.4(a) for some typical contacts. Figure 7.4(b) shows histograms of G_c (dark-blue) derived from the 223 contacts, and of $G(z)$ (light-blue) from the same data set. A Gaussian fit to the two distributions in the range from $1.0 - 2.1 G_0$ yields maxima at $1.35 G_0$ for the G_c distribution and $1.65 G_0$ for the $G(z)$ histogram. The shift by $0.3 G_0$ may be understood in terms of mechanical strain, inducing a finite slope of the $G(z)$ traces in the contact regime and shifting the peak structure towards larger conductances [138].

More precisely, on a logarithmic scale the contact traces highlighted in Figure 7.4(a) exhibit a rather constant slope in the contact region, due to elastic deformations and mechanical strain in the junction [138]. In the transition region the slope is larger. Hence, if all conductance traces were to result in the same slope in the contact regime, the $G(z)$ histogram would be expected to exhibit a step-like onset at G_c . Due to the scatter of G_c in different measurements, this onset is smeared. A maximum of the histogram is reached where nearly all conductance traces have entered the contact range with its reduced slope. This behavior can be seen in Figure 7.4(b) where the peak in $G(z)$ occurs at the trailing edge of the G_c distribution. Summarizing this issue, from $G(z)$ histograms G_c is overestimated by $\approx 20\%$ in the present study owing to a non-zero slope of

$G(z)$ in the contact regime.

Our result $G_c = 1.35 G_0$ is in good agreement with conductance histograms of recent electrochemical fabricated atomic-sized Pb contacts, where no mechanical strain forces are present and which exhibit a prominent peak at $G_c = 1.4 G_0$ [157].¹ Earlier conventional break junction experiments led to conductance histograms with a peak at $G \approx 1.7 G_0$ which again agrees with our result from Pb films with thicknesses exceeding 1 ML [7, 158].

7.3.4 Role of the Tip

Finally, we comment on the influence of the Pb tips on the contact measurements. Figure 7.5 shows conductance traces measured on the WL with two nanoscopically different Pb tips. The dark blue data points denote $G(z)$ for 30 contacts acquired throughout the moiré supercell on the WL of Pb/Ag(111). During the acquisition of the conductance trace highlighted in red, an irreversible tip switch occurred. Material was transferred from the tip to the surface, thereby changing the nanoscopic structure of the tip apex. After the material transfer, the shape of the conductance traces changed (light blue). The new nanoscopic structure of the tip favors a smooth transition from the tunneling to the contact regime throughout the moiré supercell.

It is clear that the tip shape has a significant influence on the contact traces and that a certain tip geometry seem to persist until material transfer occurs. Pb tips which preferentially show a very smooth transition from tunneling to contact regime on the WL appear to be more stable than other tip configurations. For tips which preferably show a JTC on the WL, the difference of the contact traces on the WL and Pb islands are not as pronounced. Although the stability and the shape of the contact formation is significantly affected by the atomic structure of the tip apex, we did not find an accompanying tip-dependence of the resolution of tunneling images or the shape of tunneling spectra.

¹ The range of the tip excursion was kept fixed during the measurements. Hence the significance of the histograms is reduced for conductances exceeding $G = 2.1 G_0$, which is the lowest measured conductance at $\Delta z = -2.6 \text{ \AA}$ (see light-blue area in Fig. 7.4(a)). However, the relevant finding of the mismatch of G_c deduced from simple conductance histograms as obtained by mechanical break junction or STM experiments and the explicit assignment of G_c as the endpoint of the transition from tunneling to contact is unaffected.

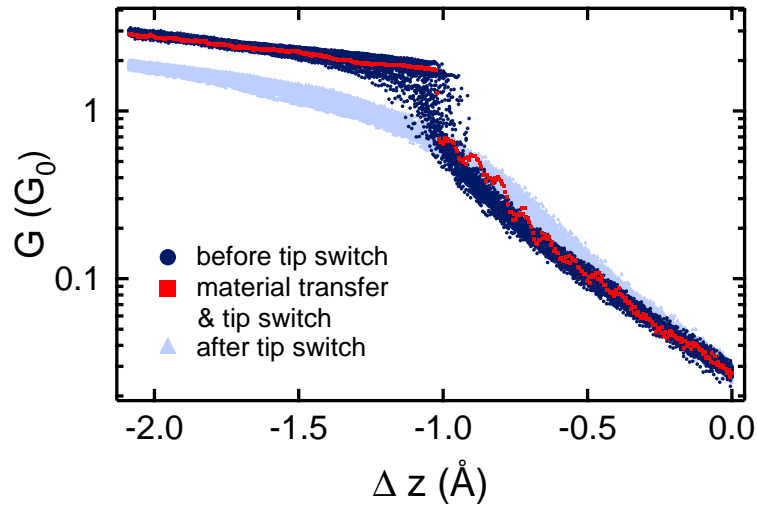


Figure 7.5: Impact of tip structure on contact traces acquired on the WL. Dark blue dots and light blue triangles represent data from contact traces before and after an irreversible tip switch, respectively. The red squares denote the contact trace, during which the tip irreversibly changed.

7.4 Conclusion

Pb(111) films deposited on Ag(111) substrates may be contacted with a STM tip without irreversible structural changes of tip or sample. Contact to the first monolayer of Pb exhibits a more gradual transition between tunneling and contact, while contact to thicker Pb films is more abrupt. This behavior is explained in terms of different vertical bonding-strengths due to a charge-transfer induced surface dipole. For the first Pb(111) ML it is shown that due to the gradual character of the tip-surface contacts using Pb tips, contact imaging can be performed. For film thicknesses exceeding 1 ML, contact conductances of $1.4 G_0$ are observed. Furthermore, we have demonstrated that the peak position in conventional conductance histograms deviates from this value.

Acknowledgement Fruitful discussions with P. Ferriani and S. Heinze and financial support by the Schleswig-Holstein-Fonds are gratefully acknowledged.

Summary

Quantum well states in Pb(111) films up to 37 monolayer have been investigated. The thickness dependence of the QWS energies is found to be very well fitted with the phase accumulation model including energy dependent scattering phase shifts at the interface and the vacuum barriers. The dispersion along the Γ -L direction is shown to be well approximated by a constant group velocity of $v_g = 13.19 \text{ eV\AA}$. The Pb/Ag interface is found to be of high-quality, such that the lossy interface scattering contribution to the lifetime broadening is significantly reduced compared to Pb/Si interfaces. The electron-electron lifetime broadening is shown to follow to a good approximation a quadratic energy dependence $\Gamma_{e-e} = \alpha(E - E_F)^2$ with $\alpha = 0.023 \text{ eV}^{-1}$. However small deviations of the quadratic energy dependence are observed and may be caused by a deviation of the screening behavior of the Pb electrons compared to that of a homogeneous electron gas [79].

The QWSs in the Pb(111) thin films give rise to a profoundly nonlinear dependence of the apparent barrier height ϕ_a on the bias voltage. The contrast of ϕ_a maps taken on multilayer Pb islands can be reversed for different tunneling bias voltage V . Similarly, the band structure on the (111) faces of the coinage metals Au, Ag, and Cu is found to have a significant impact on the voltage-resolved ϕ_a . An asymmetric voltage dependence of ϕ_a with a constant- ϕ_a range for positive sample voltages below $V \approx 3.5 \text{ V}$ is observed. Model calculations explain these experimental findings. In general, systems exhibiting significant variations of the local density of states are prone to nonlinearity effects of ϕ_a measurements at finite bias. These results have direct consequences for the interpretation of maps of the apparent barrier height. Such maps may exhibit interesting voltage dependencies, which, however, may reflect band structure variations rather than

local changes of the decay of wave functions into the tunneling gap. At bias voltages, which are small compared to the energy scale at which variations of the local density of states occur, accurate information on work function differences can be achieved. For the Pb thin films studied here, the even-odd oscillation of ϕ_a with the number of Pb layers as proposed by Schulte has been confirmed [2]. A highest occupied QWS close to E_F results in a low ϕ_a . Additionally, it was shown that the geometric asymmetry of the STM junction may also lead to a voltage polarity dependence of ϕ_a , which is, however, opposite to the experimentally observed trends. If present in the experiment, it appears to be hidden by the band structure effects.

In the course of atom-sized conductance measurements on Pb(111) films deposited on Ag(111) substrates it was found that Pb films may be contacted with a STM tip without irreversible structural changes of tip or sample. Contacts on monolayer films are found to differ from contacts made on thicker Pb films. Contacts to the first monolayer of Pb exhibit a more gradual transition between tunneling and contact, while contacts to thicker Pb films are more abrupt. This behavior is explained in terms of different vertical bonding-strengths due to a charge-transfer induced surface dipole. For the first Pb(111) ML it is shown that due to the gradual character of the tip-surface contacts, contact imaging can be performed. For the single-atom contact on Pb(111) films beyond the first monolayer conductances of $1.4 G_0$ are observed. Furthermore, it is demonstrated that analyses based on hitherto widely used conventional conductance histograms may overestimate the single-atom contact conductance by as much as 20 %.

APPENDIX A

Pb/Ag(111) Quantum Well State Energies

Here, the measured quantum well state energies as a function of film thickness as shown in Fig. 4.4 are given. The energies are determined as the peak position in the dI/dV spectra acquired with currents $I < 5$ nA. The energies can vary within ± 30 meV depending on the position on the moiré supercell. First, the results using constant current spectroscopy are given:

| ML | E_1 | E_2 | E_3 | E_4 | E_5 | E_6 | E_7 | E_8 | E_9 | E_{10} | E_{11} |
|----|-------|-------|-------|-------|-------|-------|-------|-------|-------|----------|----------|
| 1 | 2,63 | 4,23 | | | | | | | | | |
| 2 | | | | | | | | | | | |
| 3 | 1,96 | 3,96 | 4,60 | | | | | | | | |
| 4 | | | | | | | | | | | |
| 5 | | | | | | | | | | | |
| 6 | 0,63 | 2,42 | 3,73 | 4,37 | | | | | | | |
| 7 | 1,46 | 2,93 | | | | | | | | | |
| 8 | 0,63 | 2,10 | 3,31 | 4,08 | | | | | | | |
| 9 | 1,43 | 2,68 | 3,67 | 4,26 | | | | | | | |
| 10 | 0,63 | 1,85 | 2,93 | 3,80 | 4,29 | | | | | | |
| 11 | | | | | | | | | | | |
| 12 | 0,66 | 1,71 | 2,67 | 3,51 | 4,09 | | | | | | |
| 13 | 0,23 | 1,24 | 2,17 | 3,03 | 3,75 | 4,22 | | | | | |
| 14 | 0,67 | 1,60 | 2,46 | 3,24 | 3,88 | 4,32 | | | | | |
| 15 | 0,27 | 1,16 | 1,97 | 2,76 | 3,46 | 3,99 | 4,33 | | | | |
| 16 | 0,67 | 1,50 | 2,26 | 2,99 | 3,63 | 4,11 | | | | | |
| 17 | 0,31 | 1,12 | 1,84 | 2,56 | 3,22 | 3,80 | 4,23 | | | | |
| 18 | 0,72 | 1,45 | 2,15 | 2,84 | 3,45 | 3,93 | 4,27 | | | | |
| 19 | 0,35 | 1,08 | 1,74 | 2,40 | 3,01 | 3,57 | 4,03 | 4,32 | | | |
| 20 | 0,73 | 1,40 | 2,01 | 2,67 | 3,24 | 3,73 | 4,10 | | | | |

| ML | E_1 | E_2 | E_3 | E_4 | E_5 | E_6 | E_7 | E_8 | E_9 | E_{10} | E_{11} |
|-----------|-------|-------|-------|-------|-------|-------|-------|-------|-------|----------|----------|
| 26 | -0,36 | 0,16 | 0,69 | | | | | | | | |
| 27 | -0,07 | 0,44 | -0,05 | 0,47 | | | | | | | |
| 28 | -0,27 | 0,23 | | | | | | | | | |
| 29 | -0,42 | 0,03 | 0,50 | | | | | | | | |
| 30 | -0,21 | 0,25 | | | | | | | | | |
| 31 | -0,36 | 0,07 | 0,50 | | | | | | | | |
| 32 | -0,52 | -0,13 | 0,28 | 0,71 | -0,14 | 0,29 | | | | | |
| 33 | -0,31 | 0,10 | 0,51 | 0,93 | -0,32 | 0,10 | 0,51 | | | | |
| 34 | -0,50 | -0,09 | 0,31 | 0,72 | | | | | | | |
| 35 | -0,28 | 0,12 | 0,50 | 0,90 | | | | | | | |
| 36 | -0,47 | -0,05 | 0,33 | 0,71 | | | | | | | |

APPENDIX B

Scanning Tunneling Microscopy on High-Temperature Superconductors

Abstract

Scanning tunneling microscopy (STM) measurements on the high-temperature superconductor (HTS) $\text{Bi}_2\text{Sr}_2\text{CaCu}_2\text{O}_{8+\delta}$ (Bi-2212) are presented. The STM investigations on Bi-2212 as a model system for superconductivity in the HTSs were performed as part of the DFG-funded project "Nanospektroskopie und theoretische Felddescription von Feld- und Korrelationseffekten". Due to the brittle behavior of Bi-2212 in combination with its layered structure, these measurements were frequently obscured by peculiarities, which are outlined below and explained in terms of disordered superconductor-insulator-superconductor Josephson junctions induced by micro-cracks of the single crystal.

B.1 Introduction

Since the discovery of the HTSs by Bednorz and Müller in 1986 [159], a large number of experimental investigations have been performed to reveal the electronic structures and the underlying pairing mechanism in these materials. Discovered in 1988 [160], Bi-2212 is a cuprate superconductor with a two-dimensional layered perovskite structure where superconductivity originates from CuO_2 double-layers. The idealized structure of the unit cell of $\text{Bi}_2\text{Sr}_2\text{CaCu}_2\text{O}_8$ (Fig. B.1) has a tetragonal shape with dimensions $a = b = 5.4 \text{ \AA}$ and $c = 30.9 \text{ \AA}$ which consists

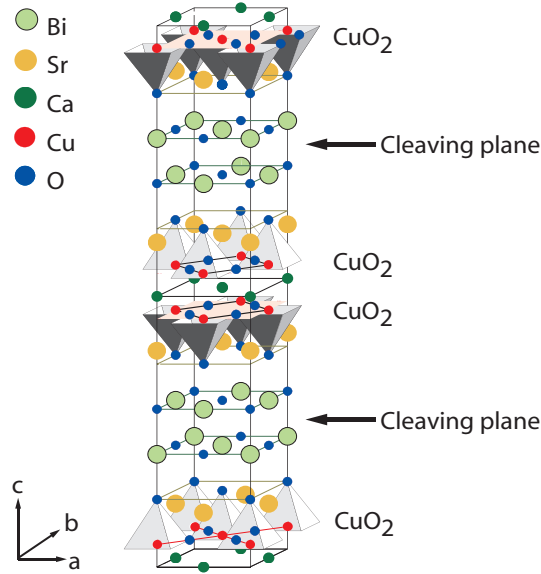


Figure B.1: Tetragonal unit cell of $\text{Bi}_2\text{Sr}_2\text{CaCu}_2\text{O}_8$ with dimensions $a = b = 5.4 \text{ \AA}$, $c = 30.9 \text{ \AA}$. Cleaving predominantly exposes the BiO layer to the surface (adopted from Ref. [161]).

of $4 \times [\text{Bi}_2\text{Sr}_2\text{CaCu}_2\text{O}_8]$ and has 15 planes. The structure may be considered as built up from two types of slabs: an insulating rocksalt derived slab containing two BiO layers and a perovskite derived $\text{SrO-CuO}_2\text{-Ca-CuO}_2\text{-SrO}$ slab. This structure has a strong two-dimensional character with a cleavage plane between the two BiO layers.

In order to be a superconductor, $\text{Bi}_2\text{Sr}_2\text{CaCu}_2\text{O}_8$ needs to be hole doped. This is usually achieved by adding interstitial oxygen atoms to the copper oxide layers, leading to the stoichiometric formula $\text{Bi}_2\text{Sr}_2\text{CaCu}_2\text{O}_{8+\delta}$. The critical temperature T_c of Bi-2212 is sensitive to the exact doping level. The maximum critical temperature of $T_c^{\text{max}} = 92 \text{ K}$ is achieved with a doping level of $p = 0.16$ which corresponds to an excess of about 0.16 holes per Cu atom [162]. For other doping levels, T_c can be estimated using the generic formula $p = 0.16 \pm \sqrt{(1 - T_c/T_c^{\text{max}})/82.6}$ [163]. However, it has to be noted that T_c also depends on the sintering process of the samples [162].

Concerning the electron transport properties perpendicular to the superconducting CuO_2 layers (along the c -axis), it has been shown that the specific layered

structure of Bi-2212 causes this material to behave like a stack of superconductor-insulator-superconductor Josephson junctions (SISJJs) [164]. The $I(V)$ characteristics of these SISJJs could be well explained by modeling the layered crystal as made up of junctions, where 3 Å thick superconducting layers, i.e. the CuO_2 double layers, are separated by 12 Å thick insulating layers [165].

Here, the results of c-axis oriented scanning tunneling spectroscopy (STS) measurements on BiO terminated surfaces of Bi-2212 are presented. For tunneling resistances R_0 below $\approx 10 \text{ M}\Omega$ the $dI/dV(V)$ spectra are regularly obscured by sharply pronounced dips. The dips are symmetric around zero bias and shift to lower values of V with decreasing R_0 . The shift is nearly proportional to R_0 and is reversible for small changes of R_0 . The widths of the dips are found to be rather independent of R_0 . By means of temperature resolved measurements, the dips are shown to be correlated with the superconducting state of Bi-2212. Following Refs. [166, 167], the dips are discussed in terms of micro-cracks of the single crystal, which lead to disordered SISJJs. For a current I which locally exceeds the critical current density of such a SISJJ, the junction switches to the resistive (normal-conducting) state. The latter is accompanied by a certain voltage drop at the junction [164], giving rise to the observed dips in the differential conductance. The shift of the dips as a function of tunneling resistance R_0 may be understood in terms of mechanical stress, induced by the tunneling tip, affecting the coupling of the SISJJs and hence their critical current value.

B.2 Experiment

Samples with dimensions of $\approx 5 \times 2 \times 0.2 \text{ mm}^3$ were cleaved from bulk single crystals and glued to a sample holder with conducting two-component silver glue. All presented data were obtained on samples which were provided by Dr. Geetha Balakrishnan from the University of Warwick: Optimally doped Bi-2212 with $T_c = 87 \text{ K}$. Additionally, the appearance of the dips in dI/dV was verified on over-doped ($p > 0.16$) Bi-2212 samples with $T_c = 81 \text{ K}$ provided by Helmuth Berger from the École Polytechnique Fédérale de Lausanne.

W and Au tips were used for this study. W tips were first electrochemically etched and then further prepared in vacuo by repeated annealing. Au tips were

cut at ambient conditions and used without further treatment. Spectra of the differential conductance dI/dV were acquired at constant height using standard lock-in detection (root-mean-square modulation 2.5 mV at 10 kHz).

For the variable temperature measurements, the inner cryostat of the STM chamber was filled with liquid nitrogen. The temperature was varied by controlled pumping on the inner cryostat.

B.3 Results and Discussion

Figure B.2(a) shows an STM topograph of the BiO terminated Bi-2212 surface. The bright dots indicate the positions of the Bi atoms. Independent of the tunneling voltage V , the O atoms are not visible in STM. The surface exhibits an incommensurate superstructure with rows of depressed atoms running along the b -axis (see arrows in Fig. B.2(b)), thereby extending the unit cell along the a -axis. (b) shows a zoom onto the superstructure of the lower left area in (a).

While the origin of the reconstruction is still under debate [162], it has been

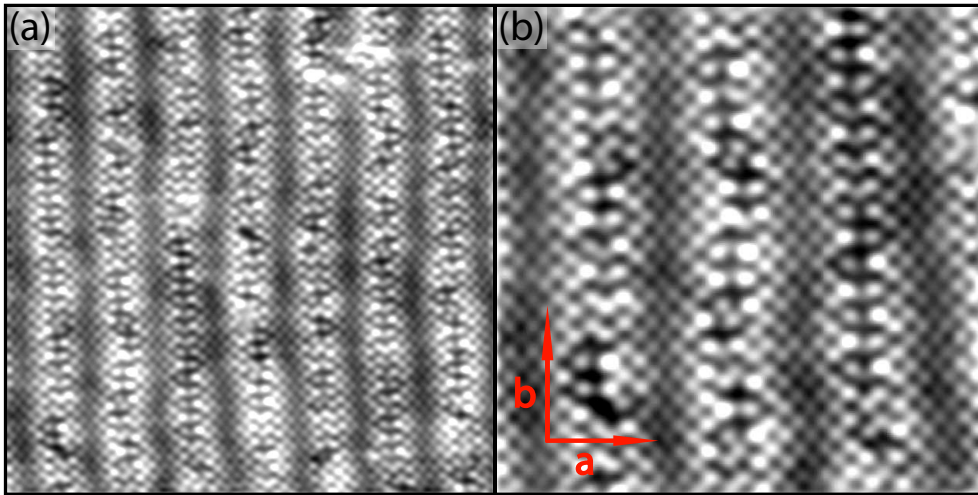


Figure B.2: STM topographs of the BiO surface of Bi-2212: (a) $20 \times 20 \text{ nm}^2$ and (b) $10 \times 10 \text{ nm}^2$ acquired at 5 K with $V = 875 \text{ mV}$, $I = 0.1 \text{ nA}$. The red arrows in (b) highlight the direction of the a - and b -axis of the unit cell. The bright dots indicate the positions of the Bi atoms [168]. Increasing brightness corresponds to increasing height. The superstructure exhibits a corrugation of $\approx 1 \text{ \AA}$.

shown that the supermodulation is not restricted to the surface. A buckling of the whole Bi-2212 crystal according to the observed supermodulation as seen by STM has been evidenced by theory and experiment [169, 170].

Concerning STS measurements on the cleaved BiO terminated surfaces, it is commonly believed that the measured DOS originates from the CuO_2 double layer. The CuO_2 layer lies 4.5 \AA beneath the surface BiO layer, with the tip being $\approx 5 \text{ \AA}$ above that plane [162]. The detailed impact of the BiO layer is still an open question. However, it is obvious from the STM topographs, which show the lattice of Bi atoms on the surface, that the role of the BiO layer cannot be completely neglected.

Figure B.3 shows a dI/dV spectrum acquired on the surface, which is shown in Figure B.2. The prominent low-energy features of the Bi-2212 spectra are two

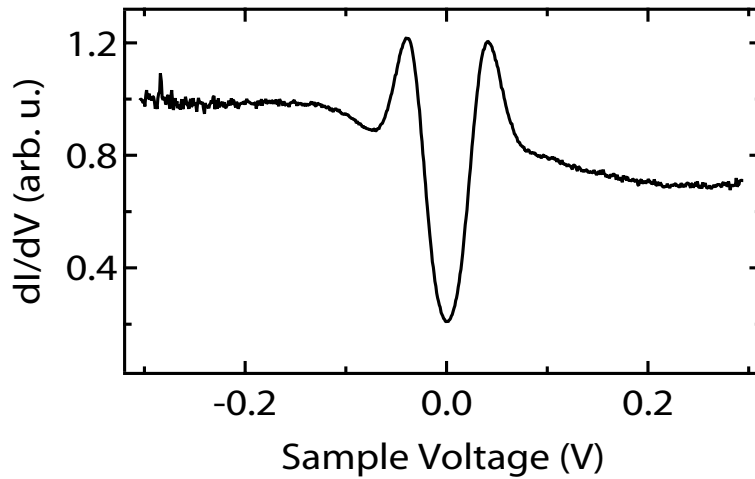


Figure B.3: Spectrum of the superconducting gap of Bi-2212; setpoint: $V = 300 \text{ mV}$, $I = 1 \text{ nA}$, $R_0 = 300 \text{ M}\Omega$.

large peaks in the differential conductance defining a clear gap centered on the Fermi energy E_F and a differential conductance increasing linearly (V-shaped) with energy close to E_F . For convenience, the superconducting gap is often defined as half the energy separating the two peaks (Δ_p). In HTSs, the reduced gap defined as $2\Delta_p/k_B T_c$ significantly exceeds 3.5 or 4.3, the values expected for weak coupling s -wave or d -wave conventional (Bardeen-Cooper-Schrieffer (BCS)) superconductors, respectively. The spectrum shown in Figure B.3 exhibits a Δ_p of 37 meV corresponding to $2\Delta_p/k_B T_c = 9.9$, which is in good agreement with

previous reports [162].

It has to be noted that in contrast to conventional superconductors, the spectroscopic gap-feature around the Fermi level is not homogeneous as a function of lateral position on the BiO terminated surface [162]. The spectrum shown here, exhibits the smallest Δ_p observed during this study.

B.3.1 Spectroscopy at Low Tunneling Resistances

Figure B.4 shows a representative spectrum of the observed anomalies at low tunneling resistances R_0 . The spectrum exhibits dips of the differential conductance (blue), which are also recognizable as kinks in the current signal I (red). The dips appear symmetric around zero sample voltage V . On well-defined surfaces where imaging yields topographs as shown in Figure B.2, the dips usually occur at elevated tunneling currents which correspond to tunneling resistances $R_0 \leq 10 \text{ M}\Omega$. On ill-defined surfaces where STM imaging only yields featureless, noisy topographs, the dips are frequently observed also for tunneling resistances $R_0 > 10 \text{ M}\Omega$.

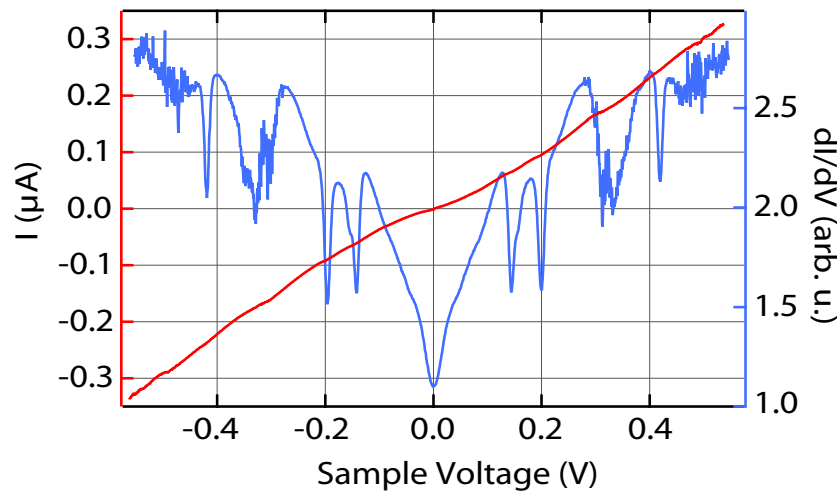


Figure B.4: Exemplary spectrum of the differential conductance dips measured on Bi-2212; setpoint: $V = 400 \text{ mV}$, $I = 200 \text{ nA}$, $R_0 = 1.8 \text{ M}\Omega$.

These dips have been observed earlier [166, 167] and were explained in terms of SISJJs [171], which were induced by the presence of the STM tip. For a current I which locally exceeds the critical current density of such a SISJJ, the junction

switches to the resistive state. Hence, a certain voltage drop at the junction occurs [164], giving rise to the observed dips in the differential conductance. As a possible origin of the SISJJs the occurrence of micro-cracks in the tunneling region due to mechanical stress, induced by the presence of the tip has been proposed. The absence of these dips in spectra taken at very high resistances, i.e. large tip-sample separations (see Fig. B.3), and consequently at very low tip-sample pressures were taken as evidence for the proposed mechanism. For a discussion of the behavior of the dips a model for a disordered system of Josephson junctions was used [167]. Using this model Volodin *et al.* derived an R_0 -dependence of the dips position as $V_{\text{dip}} \propto R_0^{1+\alpha}$. They found $\alpha \approx 0.3$. In the following the experimental R_0 -dependence of V_{dip} as found here is investigated.

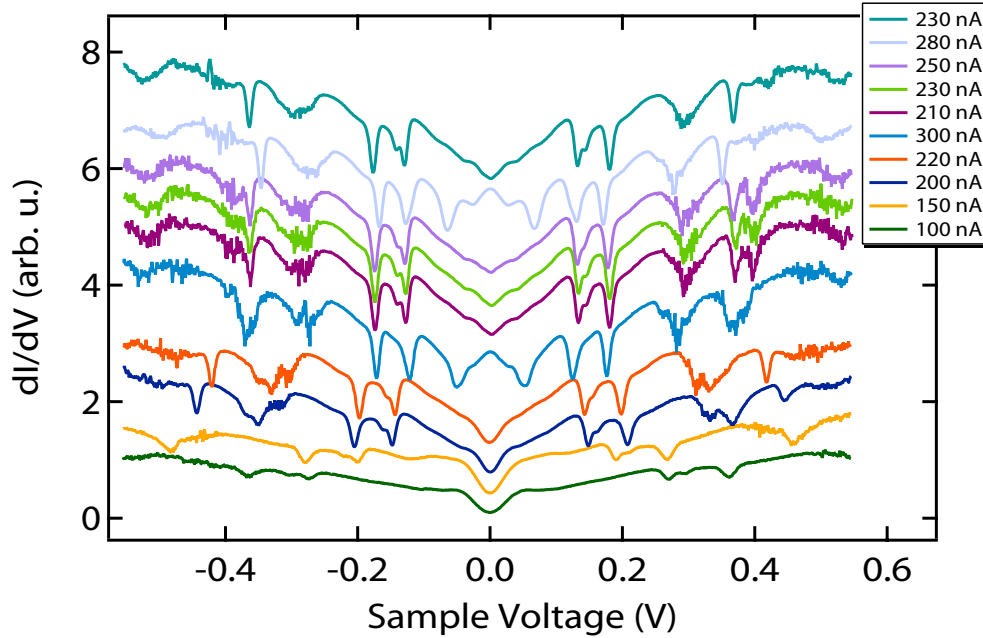


Figure B.5: Impact of tunneling resistance on the dip-structure; setpoint $V = 400$ mV, I as indicated in the legend. The spectra are vertically offset for clarity.

Figure B.5 shows an exemplary series of consecutively acquired spectra, which exhibit the dI/dV -dips. The spectra were acquired in-a-row from bottom to top. For increasing setpoint current from 100 nA to ≈ 200 nA the dips shift towards lower voltages. Upon further current increase to 300 nA, the gap feature around the Fermi level turns to a peak structure, a so-called zero-bias differential conductance peak (ZBDPC), which may be understood in terms of an

impurity induced bound state caused by the presence of the tip. Such impurity induced bound states can be seen as fingerprints of the d -wave character of superconductivity in the HTSs [162]. Retracting the tip, i.e. decreasing the setpoint current to 210 nA, causes the peak to vanish, yielding a spectrum which resembles the 220 nA spectrum which was acquired just before. Hence for small current changes, the spectra appear to be reversible.

To characterize the shift of the dips with varying tunneling resistance R_0 , the voltage of the lowest dip position as function of R_0 for a series of spectra (containing the spectra shown in Fig. B.5) are analyzed. The results are shown as red crosses in Figure B.6. It is found that for tunneling resistances in the range of $1.5 \text{ M}\Omega \leq R_0 \leq 5 \text{ M}\Omega$, the dip position depends rather linearly on R_0 ($\alpha = 0$). Beyond a certain R_0 (here $1.5 \text{ M}\Omega$), which differs for different tunneling junction geometries, the shift of the dip position saturates. To guide the eye, a line (blue) has been added to highlight the rather linear dependence of the dip position on R_0 . Note, that the main features of the observed structures are reproducible for

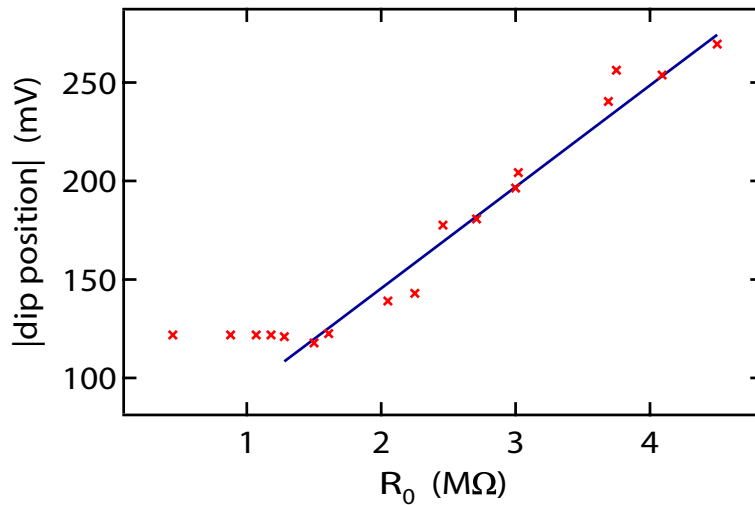


Figure B.6: Lowest dip-position in dependence of tunneling resistance R_0 .

approaches on different positions on the sample surface. To summarize, the dips shift to lower values of V with decreasing R_0 . The shift is nearly proportional to R_0 and is reversible for small changes of R_0 . The width of the conductivity dip is found to be rather independent of R_0 . Beyond a certain R_0 , which differs for different tunneling junction geometries, the shift of the dip position saturates.

B.3.2 Temperature Resolved Measurements

To clarify whether the occurrence of the dips is correlated with the superconducting state of Bi-2212 or with Coulomb-blockade effects, temperature resolved measurements were performed. If the dips vanish at temperatures close to T_c (≈ 87 K) Coulomb-blockade effects may be excluded.

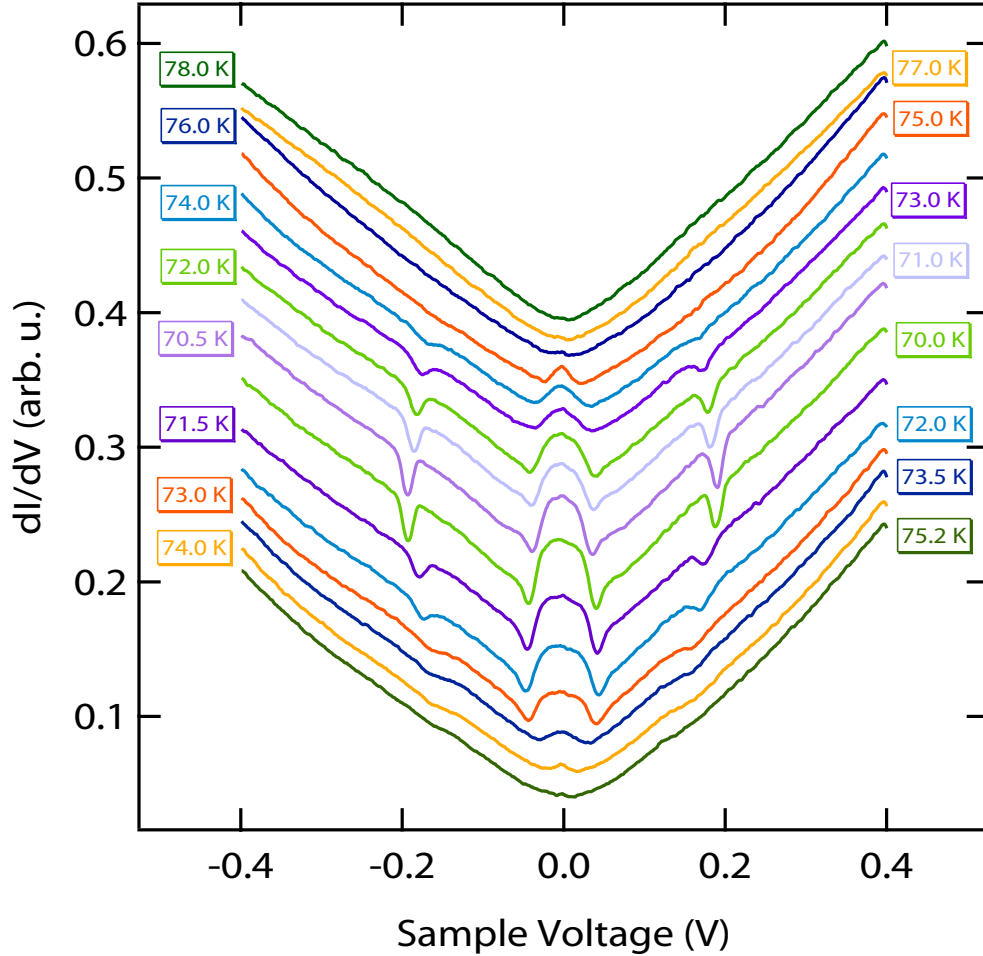


Figure B.7: Temperature resolved dI/dV spectra of the differential conductance dips; setpoint $V = 350$ mV, $I = 10$ μ A, $R_0 = 35$ k Ω . The spectra have been offset for clarity and were acquired consecutively from bottom to top at the temperatures which are indicated at the corresponding dI/dV curves.

Figure B.7 shows the result of such measurements. The spectra were taken during a cooling/heating cycle of the sample while the lateral tip position was kept constant. Acquired consecutively from bottom to top, the spectra have

been offset for clarity. The temperature is indicated at the corresponding dI/dV curve.

It is found, that the dips vanish at temperatures above ≈ 75 K. Although $T_c \approx 87$ K $>$ 75 K, it appears that the dips are indeed correlated with the superconducting state of Bi-2212 and are not induced by Coulomb-blockade effects. Below ≈ 75 K the dip position shift with temperature as also found by Walsh *et al.* using squeezable-electron-tunneling junctions [166]. During the temperature resolved measurements the tunneling resistance was reduced to 35 k Ω in order to improve the stability of the tip-sample junction and reduce drift effects. The observed ZBDPC as found here, can be understood as a direct consequence of the close proximity of tip and sample and has been discussed above.

B.4 Summary

The results of c-axis oriented STS measurements on BiO terminated surfaces of Bi-2212 have been presented. On well-defined Bi-2212 surfaces using tunneling resistances R_0 below ≈ 10 M Ω the $dI/dV(V)$ characteristics are regularly obscured by sharply pronounced dips induced by the close proximity of the tunneling tip. The dips are symmetric around zero bias and shift to lower values of V with decreasing R_0 . The shift is nearly proportional to R_0 and is reversible for small changes of R_0 . The width of the dips are found to be rather independent of R_0 . By means of temperature resolved measurements, the dips are shown to be correlated with the superconducting state of Bi-2212. Following Refs. [166, 167], the dips are discussed in terms of micro-cracks of the single crystal. These micro-cracks result in disordered superconductor-insulator-superconductor Josephson junctions (SISJJs). For a current I which locally exceeds the critical current density of such a SISJJ, the junction switches to the resistive state, which is accompanied by a certain voltage drop at the junction [164]. The shift of the dips as a function of tunneling resistance R_0 is explained in terms of mechanical stress, induced by the tunneling tip, affecting the coupling of the SISJJs and hence their critical current value.

Acknowledgment Fruitful discussions with J. Kröger and R. Kleiner are acknowledged. I thank G. Balakrishnan and H. Berger for providing the Bi-2212 samples.

Bibliography

- [1] R. C. Jaklevic and J. Lambe, *Phys. Rev. B* **12**, 4146 (1975).
- [2] F. Schulte, *Surf. Sci.* **55**, 427 (1976).
- [3] L. D. Schmidt and R. Gomer, *J. Chem. Phys.* **45**, 1605 (1966).
- [4] J. Gland and G. Somorjai, *Surf. Sci.* **41**, 387 (1974).
- [5] G. Binnig, H. Rohrer, C. Gerber, and E. Weibel, *Phys. Rev. Lett.* **49**, 57 (1982).
- [6] J. G. Simmons, *J. Appl. Phys.* **34**, 2581 (1963).
- [7] N. Agraït, A. L. Yeyati, and J. M. van Ruitenbeek, *Phys. Rep.* **377**, 81 (2003).
- [8] L. Limot, J. Kröger, R. Berndt, A. Garcia-Lekue, and W. A. Hofer, *Phys. Rev. Lett.* **94**, 126102 (2005).
- [9] Y. F. Wang et al., *Phys. Rev. Lett.* **104**, 176802 (2010).
- [10] M. Brandbyge et al., *Phys. Rev. B* **52**, 8499 (1995).
- [11] J. E. Inglesfield, *Rep. Prog. Phys.* **45**, 223 (1982).
- [12] H. Nienhaus, *Surf. Sci. Rep.* **45**, 1 (2002).
- [13] Y. Guo et al., *Science* **306**, 1915 (2004).
- [14] M. Jałochowski and M. Hoffman and E. Bauer, *Phys. Rev. Lett.* **76**, 4227 (1996).
- [15] C. M. Wei and M. Y. Chou, *Phys. Rev. B* **66**, 233408 (2002).
- [16] Y. Qi et al., *Appl. Phys. Lett.* **90**, 013109 (2007).
- [17] M. Becker and R. Berndt, *Appl. Phys. Lett.* **96**, 033112 (2010).

- [18] Y. Zhang et al., Phys. Rev. Lett. **95**, 096802 (2005).
- [19] X. Ma et al., Proc. Nat. Acad. Sci. U.S.A. **104**, 9204 (2007).
- [20] P. Jiang et al., J. Am. Chem. Soc. **130**, 7790 (2008).
- [21] J. F. Jia, K. Inoue, Y. Hasegawa, W. S. Yang, and T. Sakurai, J. Vac. Sci. Technol. B **15**, 1861 (1997).
- [22] M. Hupalo and M. C. Tringides, Phys. Rev. B **65**, 115406 (2002).
- [23] J. U. Kliewer, *Dynamics and Manipulation of Surface States*, PhD thesis, RWTH Aachen, Germany, 2000.
- [24] C. J. Chen, *Introduction to Scanning Tunneling Microscopy*, Oxford University Press Inc, 1993.
- [25] J. Stroscio and W. Kaiser, *Scanning Tunneling Microscopy*, Academic Press Inc, 1994.
- [26] R. Wiesendanger, *Scanning Probe Microscopy and Spectroscopy: Methods and Applications*, Cambridge University Press, 1994.
- [27] H. Güntherodt and R. Wiesendanger, *Scanning Tunneling Microscopy I: General Principles and Applications to Clean and Adsorbate-covered Surfaces v. 1*, Springer, Berlin, 1994.
- [28] A. Foster and W. Hofer, *Scanning Probe Microscopy: Atomic Scale Engineering by Forces and Currents*, Springer, Berlin, 2006.
- [29] M. Bowker and P. R. Davies, *Scanning Tunneling Microscopy in Surface Science*, Wiley-VCH, 2009.
- [30] R. Gaisch et al., Ultramicroscopy **42-44**, 1621 (1992).
- [31] H. Jensen, Zusammenbau eines Rastertunnelmikroskops und erste Messungen an einkristallinen Metalloberflächen, Master's thesis, Christian-Albrechts-Universität zu Kiel, 2003.
- [32] M. V. Fistul, Phys. Rev. B **75**, 014502 (2007).
- [33] A. Selloni, P. Carnevali, E. Tosatti, and C. D. Chen, Phys. Rev. B **31**, 2602 (1985).
- [34] J. G. Simmons, J. Appl. Phys. **34**, 1793 (1963).
- [35] J. Tersoff and D. R. Hamann, Phys. Rev. Lett. **50**, 1998 (1983).

- [36] J. Tersoff and D. R. Hamann, Phys. Rev. B **31**, 805 (1985).
- [37] B. Koslowski, C. Dietrich, A. Tschetschetkin, and P. Ziemann, Phys. Rev. B **75**, 035421 (2007).
- [38] M. Ziegler, N. Néel, A. Sperl, J. Kröger, and R. Berndt, Phys. Rev. B **80**, 125402 (2009).
- [39] N. D. Lang, Phys. Rev. B **37**, 10395 (1988).
- [40] M. L. Meade, *Lock-In Amplifiers: Principles and Applications*, Institution of Engineering and Technology, 1983.
- [41] Stanford Research Systems, *MODEL SR830 DSP Lock-In Amplifier*, www.thinkSRS.com.
- [42] J. Kröger et al., Prog. Surf. Sci. **80**, 26 (2005).
- [43] K. J. Rawlings, M. J. Gibson, and P. J. Dobson, J. Phys. D: Appl. Phys. **11**, 2059 (1978).
- [44] K. Takayanagi, D. Kolb, K. Kambe, and G. Lehmpfuhl, Surf. Sci. **100**, 407 (1980).
- [45] A. Rolland, J. Bernardini, and M. Barthes-Labrousse, Surf. Sci. **143**, 579 (1984).
- [46] B. J. Hinch, C. Koziol, J. P. Toennies, and G. Zhang, Europhys. Lett. **10**, 341 (1989).
- [47] B. Hinch, C. Koziol, J. Toennies, and G. Zhang, Vacuum **42**, 309 (1991).
- [48] W. J. Lorenz et al., Electrochim. Acta **37**, 2173 (1992).
- [49] U. Müller et al., Phys. Rev. B **46**, 12899 (1992).
- [50] C. Nagl, O. Haller, E. Platzgummer, M. Schmid, and P. Varga, Surf. Sci. **321**, 237 (1994).
- [51] C. Nagl, M. Schmid, and P. Varga, Surf. Sci. **369**, 159 (1996).
- [52] J. Dalmas et al., Surf. Sci. **600**, 1227 (2006).
- [53] J. H. Dil, J. W. Kim, S. Gokhale, M. Tallarida, and K. Horn, Phys. Rev. B **70**, 045405 (2004).
- [54] S. Li et al., Phys. Rev. B **74**, 075410 (2006).

- [55] S. Müller et al., *J. Phys. Condens. Matter* **13**, 1793 (2001).
- [56] C. R. Ast et al., *Phys. Rev. B* **73**, 245428 (2006).
- [57] J. Dalmas et al., *J. Phys. Chem. Solids* **67**, 601.
- [58] J. Dalmas et al., *Phys. Rev. B* **72**, 155424 (2005).
- [59] G. Wittich, *Scanning Tunneling Microscopy and Spectroscopy at Low Temperatures: Development of a 1 K-Instrument and Local Characterization of Heterogenous Metal Systems*, PhD thesis, Universität Konstanz, Germany, 2005.
- [60] J. Dalmas et al., *Surf. Sci.* **600**, 1227 (2006).
- [61] D. Pacilé et al., *Phys. Rev. B* **73**, 245429 (2006).
- [62] L. P. Nielsen et al., *Phys. Rev. Lett.* **71**, 754 (1993).
- [63] L. P. Nielsen et al., *Phys. Rev. Lett.* **74**, 1159 (1995).
- [64] L. Limot, E. Pehlke, J. Kröger, and R. Berndt, *Phys. Rev. Lett.* **94**, 036805 (2005).
- [65] J. Repp et al., *Phys. Rev. Lett.* **85**, 2981 (2000).
- [66] C. Nagl, O. Haller, E. Platzgummer, M. Schmid, and P. Varga, *Surf. Sci.* **321**, 237 (1994).
- [67] M. Schmid, W. Hebenstreit, P. Varga, and S. Crampin, *Phys. Rev. Lett.* **76**, 2298 (1996).
- [68] O. Kurnosikov, O. A. O. Adam, H. J. M. Swagten, W. J. M. de Jonge, and B. Koopmans, *Phys. Rev. B* **77**, 125429 (2008).
- [69] O. Kurnosikov, J. H. Nietsch, M. Sicot, H. J. M. Swagten, and B. Koopmans, *Phys. Rev. Lett.* **102**, 066101 (2009).
- [70] I. B. Altfeder, V. Narayanamurti, and D. M. Chen, *Phys. Rev. Lett.* **88**, 206801 (2002).
- [71] R. Otero, A. L. V. de Parga, and R. Miranda, *Phys. Rev. B* **66**, 115401 (2002).
- [72] R. Otero, A. L. V. de Parga, and R. Miranda, *Surf. Sci.* **447**, 143 (2000).
- [73] R. C. Jaklevic, J. Lambe, M. Mikkor, and W. C. Vassell, *Phys. Rev. Lett.* **26**, 88 (1971).

- [74] S. Qin, J. Kim, Q. Niu, and C. Shih, *Science* **324**, 1314 (2009).
- [75] F. Calleja, M. C. G. Passeggi, J. J. Hinarejos, A. L. V. de Parga, and R. Miranda, *Phys. Rev. Lett.* **97**, 186104 (2006).
- [76] A. Crottini et al., *Phys. Rev. Lett.* **79**, 1527 (1997).
- [77] P. M. Echenique et al., *Surf. Sci. Rep.* **52**, 219 (2004).
- [78] I. Hong et al., *Phys. Rev. B* **80**, 081409 (2009).
- [79] A. Zugarramurdi, N. Zabala, V. M. Silkin, A. G. Borisov, and E. V. Chulkov, *Phys. Rev. B* **80**, 115425 (2009).
- [80] N. V. Smith, N. B. Brookes, Y. Chang, and P. D. Johnson, *Phys. Rev. B* **49**, 332 (1994).
- [81] D. P. Woodruff, W. A. Royer, and N. V. Smith, *Phys. Rev. B* **34**, 764 (1986).
- [82] P. M. Echenique and J. B. Pendry, *J. Phys. C* **11**, 2065 (1978).
- [83] N. V. Smith, *Phys. Rev. B* **32**, 3549 (1985).
- [84] D. Luh, T. Miller, J. J. Paggel, M. Y. Chou, and T. Chiang, *Science* **292**, 1131 (2001).
- [85] E. McRae and M. Kane, *Surf. Sci.* **108**, 435 (1981).
- [86] P. Echenique and J. Pendry, *Prog. Surf. Sci.* **32**, 111 (1989).
- [87] E. V. Chulkov, V. M. Silkin, and P. M. Echenique, *Surf. Sci.* **437**, 330 (1999).
- [88] M. C. Yang et al., *Phys. Rev. Lett.* **102**, 196102 (2009).
- [89] M. H. Upton, T. Miller, and T. Chiang, *Phys. Rev. B* **71**, 033403 (2005).
- [90] J. Li, W. Schneider, R. Berndt, and B. Delley, *Phys. Rev. Lett.* **80**, 2893 (1998).
- [91] W. B. Su et al., *Phys. Rev. Lett.* **86**, 5116 (2001).
- [92] J. R. Anderson and A. V. Gold, *Phys. Rev.* **139**, A1459 (1965).
- [93] M. Jałochowski, H. Knoppe, G. Lilienkamp, and E. Bauer, *Phys. Rev. B* **46**, 4693 (1992).

-
- [94] L. Limot, T. Maroutian, P. Johansson, and R. Berndt, *Phys. Rev. Lett.* **91**, 196801 (2003).
- [95] N. Miyata et al., *Phys. Rev. B* **78**, 245405 (2008).
- [96] J. H. Dil, J. W. Kim, T. Kampen, K. Horn, and A. R. H. F. Ettema, *Phys. Rev. B* **73**, 161308 (2006).
- [97] F. Yndurain and M. P. Jigato, *Phys. Rev. Lett.* **100**, 205501 (2008).
- [98] A. Bauer, A. Mühlig, D. Wegner, and G. Kaindl, *Phys. Rev. B* **65**, 075421 (2002).
- [99] D. Wegner, A. Bauer, and G. Kaindl, *Phys. Rev. Lett.* **94**, 126804 (2005).
- [100] D. Wegner et al., *Phys. Rev. B* **73**, 115403 (2006).
- [101] J. Li, W. Schneider, and R. Berndt, *Phys. Rev. B* **56**, 7656 (1997).
- [102] T. Miller, A. Samsavar, G. E. Franklin, and T. C. Chiang, *Phys. Rev. Lett.* **61**, 1404 (1988).
- [103] J. J. Quinn and R. A. Ferrell, *Phys. Rev.* **112**, 812 (1958).
- [104] G. Binnig, H. Rohrer, C. Gerber, and E. Weibel, *Appl. Phys. Lett.* **40**, 178 (1982).
- [105] G. Binnig and H. Rohrer, *Surf. Sci.* **126**, 236 (1983).
- [106] L. Olesen et al., *Phys. Rev. Lett.* **76**, 1485 (1996).
- [107] G. Binnig, N. Garcia, H. Rohrer, J. M. Soler, and F. Flores, *Phys. Rev. B* **30**, 4816 (1984).
- [108] J. F. Jia, K. Inoue, Y. Hasegawa, W. S. Yang, and T. Sakurai, *Phys. Rev. B* **58**, 1193 (1998).
- [109] D. Ostermann, G. Walther, and K. D. Schierbaum, *Phys. Rev. B* **71**, 235416 (2005).
- [110] R. Pascal, C. Zarnitz, M. Bode, and R. Wiesendanger, *Phys. Rev. B* **56**, 3636 (1997).
- [111] M. Saida, K. Horikawa, T. Sato, S. Yamamoto, and M. Sasaki, *Surf. Sci.* **600**, L139 (2006).
- [112] L. Scandella and H. Güntherodt, *Ultramicroscopy* **42-44**, 546 (1992).

- [113] L. Olesen, E. Laegsgaard, I. Stensgaard, and F. Besenbacher, *Appl. Phys. A* **66**, S157 (1998).
- [114] W. Mizutani, T. Ishida, N. Choi, T. Uchihashi, and H. Tokumoto, *Appl. Phys. A* **72**, S181 (2001).
- [115] Y. Yamada, A. Sinsarp, M. Sasaki, and S. Yamamoto, *Jpn. J. Appl. Phys.* **42**, 4898 (2003).
- [116] T. Furuhashi, Y. Oshima, and H. Hirayama, *Appl. Surf. Sci.* **253**, 651 (2006).
- [117] H. Totsuka, Y. Gohda, S. Furuya, and S. Watanabe, *Phys. Rev. B* **70**, 155405 (2004).
- [118] J. A. Stroscio, R. M. Feenstra, and A. P. Fein, *Phys. Rev. Lett.* **57**, 2579 (1986).
- [119] K. Gundlach, *Solid-State Electron.* **9**, 949 (1966).
- [120] R. Smoluchowski, *Phys. Rev.* **60**, 661 (1941).
- [121] L. C. Davis, M. P. Everson, R. C. Jaklevic, and W. Shen, *Phys. Rev. B* **43**, 3821 (1991).
- [122] M. F. Crommie, C. P. Lutz, and D. M. Eigler, *Nature* **363**, 524 (1993).
- [123] P. Avouris and I. Lyo, *Science* **264**, 942 (1994).
- [124] L. Bartels et al., *Phys. Rev. B* **67**, 205416 (2003).
- [125] G. Hoffmann, T. Maroutian, and R. Berndt, *Phys. Rev. Lett.* **93**, 076102 (2004).
- [126] J. Kliewer et al., *Science* **288**, 1399 (2000).
- [127] F. Reinert, G. Nicolay, S. Hüfner, U. Probst, and E. Bucher, *J. Electron. Spectrosc. Relat. Phenom.* **114-116**, 615 (2001).
- [128] M. Ziegler, N. Néel, A. Sperl, J. Kröger, and R. Berndt, *Phys. Rev. B* **80**, 125402 (2009).
- [129] J. Li, W. D. Schneider, S. Crampin, and R. Berndt, *Surf. Sci.* **422**, 95 (1999).
- [130] M. G. Vergniory, J. M. Pitarke, and S. Crampin, *Phys. Rev. B* **72**, 193401 (2005).

- [131] M. Becker, S. Crampin, and R. Berndt, *Appl. Phys. A* **88**, 555 (2007).
- [132] N. M. Miskovsky, P. H. Cutler, T. E. Feuchtwang, and A. A. Lucas, *Appl. Phys. A* **27**, 139 (1982).
- [133] J. Bono, R. Good, and Jr., *Surf. Sci.* **151**, 543 (1985).
- [134] X. Liu et al., *Appl. Phys. Lett.* **93**, 093105 (2008).
- [135] I. B. Altfeder, K. A. Matveev, and D. M. Chen, *Phys. Rev. Lett.* **78**, 2815 (1997).
- [136] J. K. Gimzewski and R. Möller, *Phys. Rev. B* **36**, 1284 (1987).
- [137] U. Dürig, O. Züger, and D. W. Pohl, *Phys. Rev. Lett.* **65**, 349 (1990).
- [138] J. C. Cuevas et al., *Phys. Rev. Lett.* **81**, 2990 (1998).
- [139] R. Landauer, *IBM J. Res. Dev.* **1**, 223 (1957).
- [140] M. Büttiker, Y. Imry, R. Landauer, and S. Pinhas, *Phys. Rev. B* **31**, 6207 (1985).
- [141] A. Yazdani, D. M. Eigler, and N. D. Lang, *Science* **272**, 1921 (1996).
- [142] N. Néel et al., *Phys. Rev. Lett.* **98**, 016801 (2007).
- [143] N. Néel, J. Kröger, and R. Berndt, *Phys. Rev. Lett.* **102**, 086805 (2009).
- [144] N. Néel et al., *Phys. Rev. Lett.* **98**, 065502 (2007).
- [145] G. Schull, T. Frederiksen, M. Brandbyge, and R. Berndt, *Phys. Rev. Lett.* **103**, 206803 (2009).
- [146] I. B. Altfeder, D. M. Chen, and K. A. Matveev, *Phys. Rev. Lett.* **80**, 4895 (1998).
- [147] J. Kröger, H. Jensen, and Berndt, *New J. Phys.* **9**, 153 (2007).
- [148] M. Becker and R. Berndt, *Phys. Rev. B* **81**, 205438 (2010).
- [149] D. Kolb, M. Przasnyski, and H. Gerischer, *J. Electroanal. Chem.* **54**, 25 (1974).
- [150] D. D. Stranz, *J. Chem. Phys.* **74**, 2116 (1981).
- [151] C. Kittel, *Introduction to Solid State Physics*, Wiley, 7 edition, 1995.

- [152] W. Hofer, A. Garcia-Lekue, and H. Brune, *Chem. Phys. Lett.* **397**, 354 (2004).
- [153] J. A. Stroscio and R. J. Celotta, *Science* **306**, 242 (2004).
- [154] A. Sperl, J. Kröger, and R. Berndt, *Phys. Rev. B* **81**, 035406 (2010).
- [155] W. A. Hofer, A. J. Fisher, R. A. Wolkow, and P. Grütter, *Phys. Rev. Lett.* **87**, 236104 (2001).
- [156] R. Berndt, J. Kröger, N. Néel, and G. Schull, *Phys. Chem. Chem. Phys.* **12**, 1022 (2010).
- [157] F.-Q. Xie et al., *Phys. Rev. B* **82**, 075417 (2010).
- [158] A. I. Yanson, *Atomic chains and electronic shells: quantum mechanisms for the formation of nanowires*, PhD thesis, Universiteit Leiden, The Netherlands, 2001.
- [159] J. Bednorz and K. Müller, *Z. Phys. B: Condens. Matter* **64**, 189 (1986).
- [160] H. Maeda, Y. Tanaka, M. Fukutomi, and T. Asano, *Jpn. J. Appl. Phys.* **27**, L209 (1988).
- [161] S. Johnston, F. Vernay, and T. P. Devereaux, *Europhys. Lett.* **86**, 37007 (2009).
- [162] Ø. Fischer, M. Kugler, I. Maggio-Aprile, C. Berthod, and C. Renner, *Rev. Mod. Phys.* **79**, 353 (2007).
- [163] M. R. Presland, J. L. Tallon, R. G. Buckley, R. S. Liu, and N. E. Flower, *Physica C* **176**, 95 (1991).
- [164] R. Kleiner, F. Steinmeyer, G. Kunkel, and P. Müller, *Phys. Rev. Lett.* **68**, 2394 (1992).
- [165] R. Kleiner and P. Müller, *Phys. Rev. B* **49**, 1327 (1994).
- [166] T. Walsh, J. Moreland, R. H. Ono, and T. S. Kalkur, *Phys. Rev. B* **43**, 11492 (1991).
- [167] A. P. Volodin, J. Aarts, I. V. Falkovsky, and M. V. Fistul', *Physica C* **201**, 426 (1992).
- [168] M. D. Kirk et al., *Science* **242**, 1673 (1988).
- [169] R. E. Gladyshevskii and R. Flükiger, *Acta Crystallogr., Sect. B* **52**, 38 (1996).

- [170] Y. He, S. Graser, P. J. Hirschfeld, and H.-P. Cheng, Phys. Rev. B **77**, 220507 (2008).
- [171] K. K. Likharev, Rev. Mod. Phys. **51**, 101 (1979).

List of the Author's Publications

Complete List of the Author's Peer-Reviewed Journal Publications

1. M. Becker, S. Crampin, R. Berndt
Theoretical analysis of STM-derived lifetimes of excitations in the Shockley surface-state band of Ag(111),
Phys. Rev. B **73**, 081402 (2006)
2. J. Kröger, M. Becker, H. Jensen, Th. von Hofe, N. Néel, L. Limot, R. Berndt, S. Crampin, E. Pehlke, C. Corriol, V.M. Silkin, D. Sánchez-Portal, A. Arnau, E.V. Chulkov, P.M. Echenique
Dynamics of surface-localised electronic excitations studied with the scanning tunnelling microscope,
Prog. Surf. Sci. **82**, 29 (2007)
3. M. Becker, S. Crampin, R. Berndt
Lifetimes of electrons in the Shockley surface state band of Ag(111),
Appl. Phys. A **88**, 555 (2007)
4. G. Schull, N. Néel, M. Becker, J. Kröger, R. Berndt
Spatially resolved conductance of oriented C₆₀,
New J. Phys. **10**, 065012 (2008)
5. G. Schull, M. Becker, R. Berndt
Imaging confined electrons with plasmonic light,
Phys. Rev. Lett. **101**, 136801 (2008)

6. N. Hauptmann, M. Becker, J. Kröger, R. Berndt
Surface reconstruction and energy gap of superconducting $V_3Si(001)$,
Phys. Rev. B **79**, 144522 (2009)
7. M. Becker, R. Berndt
Influence of band structure on the apparent barrier height in scanning tunneling microscopy,
Phys. Rev. B **81**, 035426 (2010)
8. M. Becker, R. Berndt
Contrast inversion of the apparent barrier height of Pb thin films in scanning tunneling microscopy,
Appl. Phys. Lett. **96**, 033112 (2010)
9. M. Becker, R. Berndt
Scattering and lifetime broadening of quantum well states in Pb films on Ag(111),
Phys. Rev. B **81**, 205438 (2010)
10. M. Becker, R. Berndt
Conductance of atom-sized Pb contacts,
New J. Phys. **12**, 113010 (2010)

Selbständigkeitserklärung

Diese Dissertationsschrift wurde von mir in Form und Inhalt unter Anleitung von Prof. Dr. Richard Berndt und nur unter Zuhilfenahme der angegebenen Hilfsmittel angefertigt. Diese Arbeit hat weder in gleicher, noch in ähnlicher Form an anderer Stelle im Rahmen eines Prüfungsverfahrens vorgelegen.

Kiel,
(Ort)

(Datum)

(Unterschrift)

Wissenschaftlicher Lebenslauf

Persönliche Daten

Name: Michael Becker
geb. am 30.10.1975 in Kiel
deutsche Staatsangehörigkeit

Studium

10/2000 - 05/2006 Studium der Physik an der Christian-Albrechts-Universität zu Kiel

Diplomarbeit: 04/2005 - 04/2006,
Lifetimes of Stark-shifted Shockley Surface States at Ag(111) and Cu(111)
Betreuer: Prof. Dr. Richard Berndt, Universität zu Kiel
Dr. Simon Crampin, University of Bath, UK

Auslandsaufenthalte:
08/2002 - 06/2003: ERASMUS-Student an der
Universität in Bergen, Norwegen
04/2005 & 10/2005: Gastwissenschaftler an der
Universität in Bath, UK

seit 06/2006 Promotionsstudium am Institut für Experimentelle
und Angewandte Physik der Christian-Albrechts-
Universität zu Kiel

Auslandsaufenthalt: 09/2007 - 12/2007:
Gastwissenschaftler am NIMS in Tsukuba, Japan.
Betreuer: Dr. Takashi Uchihashi

Danksagung

An dieser Stelle möchte ich mich bei allen Personen bedanken, die mich in meiner wissenschaftlichen Tätigkeit unterstützt und zum Gelingen dieser Doktorarbeit beigetragen haben.

Besonders danke ich Prof. Dr. Richard Berndt für die Möglichkeit, diese Arbeit in seiner Arbeitsgruppe anfertigen zu können, für viele wertvolle Ratschläge und das unkomplizierte Arbeitsklima. Prof. Dr. Jörg Kröger danke ich für viele hilfreiche Diskussionen und die stete Aushilfe mit UHV Komponenten. Dr. Takashi Uchihashi danke ich für die Gastfreundschaft während meines Aufenthalts am NIMS und die unzähligen Diskussionen über Wissenschaft und Japan. Dr. Thomas Jürgens danke ich für die Einführung in die Vakuumtechnik und Messtechnik und für viele Tipps und Tricks rund um die Rastertunnelmikroskopie. Herrn Frank Brach und allen Mitarbeitern der Werkstatt für die gute Zusammenarbeit und tatkräftige Unterstützung beim Instandhalten der UHV-Anlage. Jörg Neubauer möchte ich für die schnelle Hilfe bei Elektronikproblemen danken. Frau Monika Seeger danke ich für die stets freundliche Unterstützung beim Ausfüllen von Formularen jeglicher Art und die nette Atmosphäre in ihrem Büro.

Bedanken möchte ich mich auch bei den restlichen Mitgliedern und Ehemaligen der Arbeitsgruppe für die gute Arbeitsatmosphäre, viele Tipps und Unterstützung: Simon Altenburg, Sven Marten Czerwonka, Dr. Xin Ge, Björn Gojdka, Dr. Thiruv. Gopakumar, Dr. Markus Gruyters, Christian Hamann, Nadine Hauptmann, Dr. Thomas von Hofe, Dr. I-Po Hong, Henning Jensen, Sujoy Karan, Marco Knutzen, Dr. Laurent Limot, Dr. Carlos Manzano, Dr. Francesca Matino, Lars Mühlenberend, Svenja Mühlenberend, Dr. Nicolas Néel, Uschi Nebendahl, Dr. Jürgen Rathlev, Maria Reinhardt, Nico Ruppelt, Dr. Patrick Schmidt, Natalia Schneider, Dr. Guillaume Schull, Alexander Sperl, Dr. Yongfeng Wang, Dr. Alexander Weismann, René Woltmann, Dr. Hao Zheng, Dr. Martin Ziegler.

Besonderen Dank gilt meiner Familie für die fortwährende Unterstützung. Meiner Freundin Barbara möchte ich für die Unterstützung und Aufmunterung sowie die in den letzten Monaten aufgebrachte Geduld danken.

Der DFG und der JSPS danke ich für die erhaltene finanzielle Förderung.